A surrogate model approach to study the effect of rainfall through cracks on the macro-stability of canal dikes

Jorijn Holstvoogd

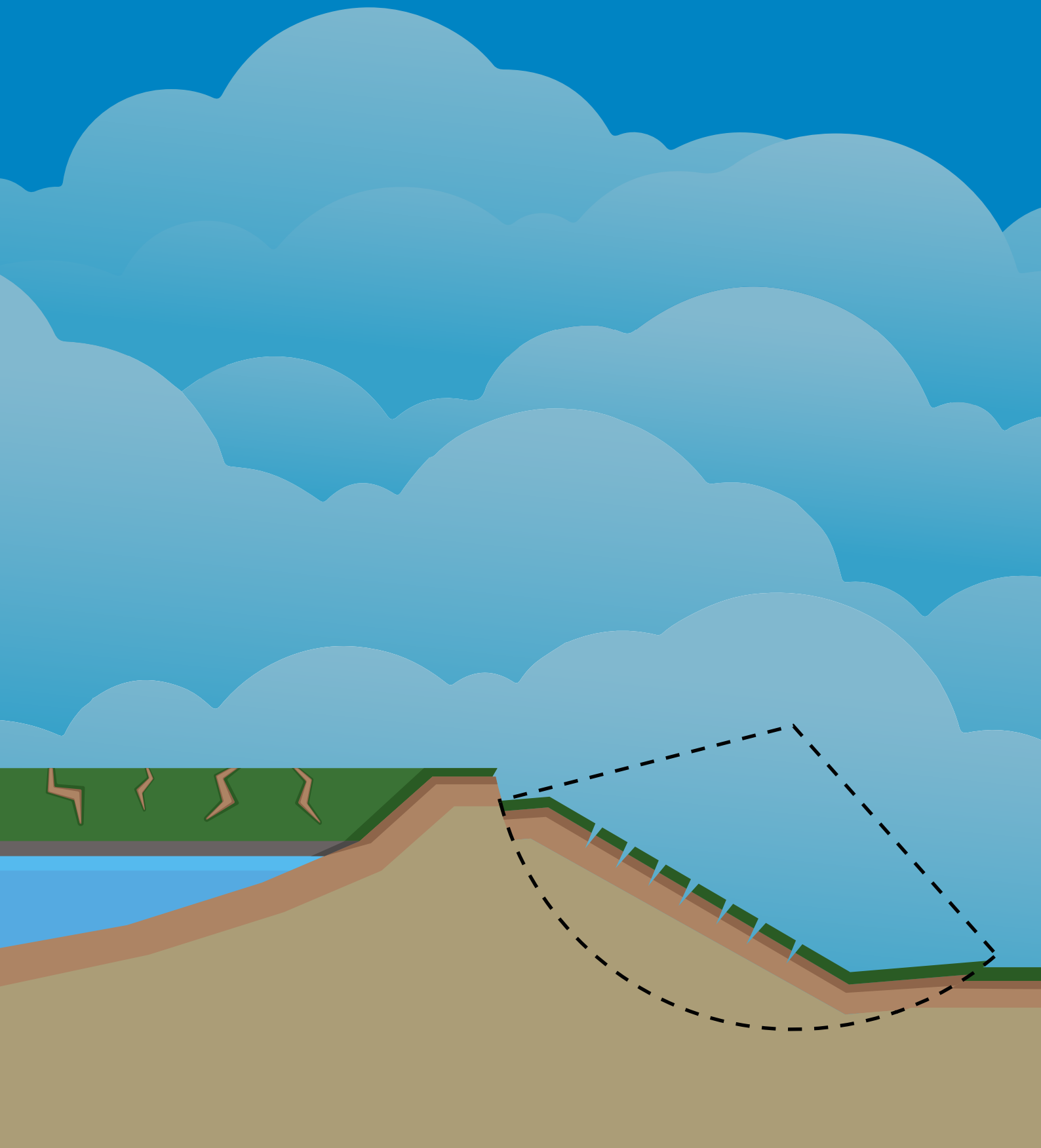

A surrogate model approach to study the effect of rainfall through cracks on the macro-stability of canal dikes

By

J.R. Holstvoogd

In partial fulfilment of the requirements for the degree of

Master of Science
in Civil Engineering

at the Delft University of Technology,
to be defended publicly on Monday the 7th of November, 2022 at 10:00 AM.

Thesis Committee:
Dr. T.A. Bogaard (chair) (TU Delft)
Dr. J.P. Aguilar-López (TU Delft)
Dr. S.J.H. Rikkert (TU Delft)

Preface

This MSc thesis is my final work for obtaining a master's degree in Water Management. I followed the specialization of Hydrology, through which I developed my interest in machine learning techniques for hydrological applications. It is with this passion that I present this research.

Firstly, I would like to thank my daily supervisor: Juan Pablo. It has been a pleasure working with you and learning from your expertise. Thank you for your guidance, inspiring discussions, and motivating words when I needed them the most. Thanks for helping me consult additional expertise and for never making me feel like I was doing the research alone! Additionally, I would like to thank the rest of my committee, Thom Bogaard, and Stephan Rikkert. Thank you for your critical constructive feedback and the enthusiasm you have shown during our meetings. Also, I would like to thank Anika Vroom and my dad for proofreading and providing solid feedback. Lastly, I want to thank my friends, especially Karlijn, Julia, Juliette, Kevin, Helena, and my family, for getting me out of my study cave and for all the support during my thesis.

Jorijn Holstvoogd Delft, November 2022

Abstract

Under the current climate change projections, droughts and extreme rainfall events are becoming more common and intense. During sustained droughts, soil cracks can develop in the topsoil of a dike. These soil cracks can enhance the infiltration and drainage of the dike, affecting the dike stability. This study's main objective is to better understand the potential influence of cracks on the hydrology and dike stability of canal dikes.

A finite element model (FEM) was built to study the hydrological response and stability of a canal dike due to rainfall infiltration through a uniformly distributed cracked top layer. This model included the fast hydrological response of the fractures and their exchange with the soil. A surrogate model (a simplified data-driven machine learning model) was built using training data generated by the FEM to reduce the computational burden and allow for a sensitivity and stochastic reliability assessment.

An evaluation of important model features, such as the connectivity among cracks and soil swelling, revealed that the cracks have a very localized influence on the infiltration and drainage of water through the dike. Water drainage in the toe of the dike is restricted by soil swelling resulting in a larger decline in dike stability. The sensitivity analysis found that the cracks facilitate more infiltration than drainage before the crack parameters, such as the crack aperture and the amount of cracking, reached a threshold. Above this threshold, drainage provided by the cracks is greater than the infiltration. The failure probability was calculated for a variety of different rainfall patterns. A pattern where the rainfall intensity incrementally increases over time results in the highest failure probability.

The main conclusion from this study is that soil cracks influence the stability of the dike by enhancing infiltration and drainage under rainfall. Under low-intensity rainfall, the cracks in the toe facilitate more water to drain out of the dike than rainfall to infiltrate, stabilizing the dike. However, in the absence of cracks in the toe, the cracks provide more infiltration than drainage resulting in a lower dike stability. Under high-intensity rainfall, cracks in the crest and the inner slope of a dike advance the wetting front resulting in a larger decline in dike stability than a dike without soil cracks. Rainfall infiltration and drainage in a cracked dike depend on both rainfall characteristics, such as the average rainfall intensity, duration, and pattern, and the crack features, such as the crack width, amount of cracking, and the connectivity of the cracks. Since this study was not validated with observations, it is recommended that further studies aim to validate the observed influence of the cracks by conducting field experiments.

Acronyms

CDF	Cumulative Density Function
CPT	Cone Penetration Test
DPM	Dual-Permeability Model
FEM	Finite-Element Model
FNN	Forward Neural Network
FOS	Factor of Safety
IDF	Intensity Duration Frequency
LHS	Latin Hypercube Sampling
LSTM	Long Short Term Memory
OAT	One-At-the-Time
PCA	Principle Component Analysis
PDF	Probability Density Function
REV	Representative Elementary Volume
RNN	Recurrent Neural Network
SHANSEP	Stress History And Normalized Soil Engineering Property
SPM	Single-Permeability Model
SWRC	Soil Water Retention Curve

Contents

List of Figures

List of Tables

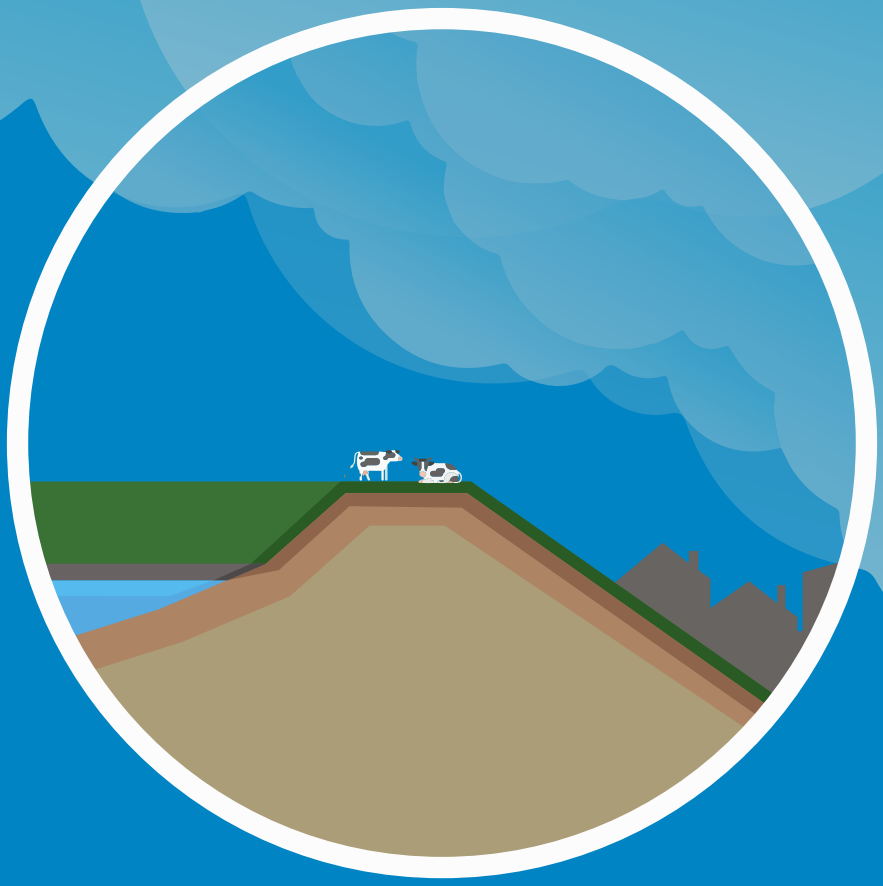

1. Introduction

1 Introduction

The risk of flooding from rivers or the sea is prevalent in low-lying deltas like the Netherlands. Floods can have disastrous outcomes, often involving casualties and significant economic impacts. This was the case during the "Watersnoodramp" in February of 1953 when a severe storm flooded a large region of the delta in the Netherlands, resulting in the loss of 1800 lives and large economic damages (Goemans & Visser, 1987). Flood defenses such as river dikes are constructed to protect these flood-prone areas and are divided into primary and regional flood defenses. While the primary flood defenses protect against floods from the sea, main rivers, and lakes, the regional flood defenses provide protection from regional rivers, canals, and smaller lakes. These systems are managed via a risk-based approach, where flood risk is defined as the product of the probability of occurrence of a flood event and the severity of the subsequent consequences of the event. Since the Netherlands contains several densely populated regions, a flood's economic and social consequences can be enormous. In the risk-based assessment of dikes, the likelihood of the occurrence of a flood event is directly correlated to the condition of the dike ring. Therefore, maintaining these flood defenses is crucial from a risk-based perspective.

Figure 1: Flood defenses of the Netherlands

The Netherlands contains almost 18.000 kilometers of flood defenses that need to be assessed every few years. Hence, cost-effective methods for risk-based assessments are required to maintain the safety of the flood defenses. In these assessments, the probability of failure is divided among possible failure modes. Therefore, it is essential to understand the likelihood of occurrence of each type of failure mode. One of these failure modes is the macro-instability of the inner slope of a dike. Rijkswaterstaat (2016) defines macro-instability as the sliding of a soil plane which results in a loss of its water-retaining function. The loss of stability is mainly influenced by the buildup of water which reduces the effective stresses required to stabilize the dike. Therefore, macro-instability can be triggered by hydrological events.

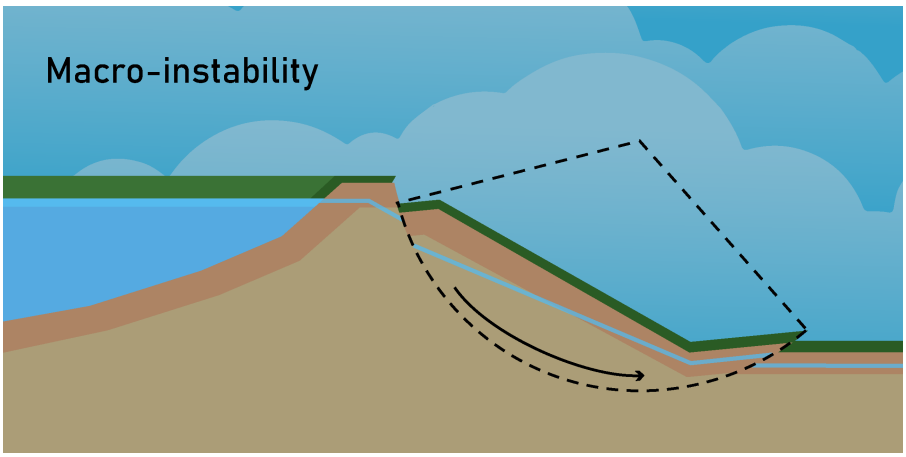

Figure 2: Macro-instability of the inner slope of a dike

1.1 Problem statement

In recent years, the effects of climate change are becoming increasingly visible. Prolonged droughts and extreme storms are becoming more common (IPCC, 2022). Sustained droughts have caused dikes to form cracks due to soil shrinkage. These cracks, in combination with rainfall, are believed to affect their stability.

Most dikes in the Netherlands consist of cohesive soil or have cohesive topsoil, which is prone to forming drought-induced cracks. These cracks, or fractures, are expected to influence the infiltration and water retention within the soil and accommodate for preferential flow (J. H. Li et al., 2011; Novák et al., 2002). Preferential flow refers to the rapid flow of water through available soil defects and occurs at shorter time spans as opposed to flow through the soil matrix (Beven & Germann, 2013). The buildup of increased water pressures within the dike due to preferential flow can reduce the effective stresses required to stabilize the slope and result in a larger slope instability (Shao et al., 2015; Kukemilks et al., 2018). However, a connected network of these cracks may facilitate drainage and decrease the pore pressures within the dike.

Contrary to the primary flood defenses, fluctuations in the phreatic surface within the regional flood defenses are governed by rainfall as they observe a controlled water level (Ten Bokkel Huinink, 2016; Lendering, 2016). Therefore, the presence of soil cracks in these dikes may induce fluctuations in the phreatic surface and affect their stability. Thus, an improved understanding of the spatio-temporal effect of rainfall-induced preferential flow through these cracks on the macro-stability of a dike may aid in optimizing dike asset management.

1.2 Objective

This research aims to analyze the influence of preferential flow through cracked topsoil on the macro-stability of canal dikes. A dual-permeability model (DPM) will be implemented to investigate the influence of preferential flow. The main research question to be answered in this study is defined as follows:

"How does rainfall-induced preferential flow in soil cracks influence the macro-stability of canal dikes?"

To dissect and simplify this research question, it is split up into several sub-questions which are defined as follows:

1. *"How to model rainfall infiltration through cracks on the slope stability of a canal dike?"*
2. *"How to build a surrogate model of rainfall infiltration through cracks and its effect on the slope stability?"*
3. *"What is the effect of varying the crack and rainfall parameters on the slope stability?"*

The first sub-question focuses on building a finite-element model (FEM), which aims to model rainfall infiltration through soil cracks and its effect on the macro-stability. Elements of the model are first researched and subsequently built into the FEM in COMSOL. Four study parameters are chosen to capture the influence of the cracks and rainfall. These parameters are the observed maximum crack width, the volumetric ratio of the cracks, average rainfall intensity, and the associated return period of the storm. The synergy of the influence of these parameters is studied and evaluated. A surrogate model is built using machine learning techniques for the second sub-question.

This model is built on the results of the FEM and is assessed by comparing it with the FEM. Finally, the third sub-question encompasses the effect of varying the study parameters using the surrogate model to determine the influence of cracks on the slope stability of a canal dike.

1.3 Thesis structure

The influence of preferential flow through soil cracks was studied by building an FEM and a surrogate model of the FEM. Since every step depends on the previous, this thesis is structured according to the flowchart in Figure 3.

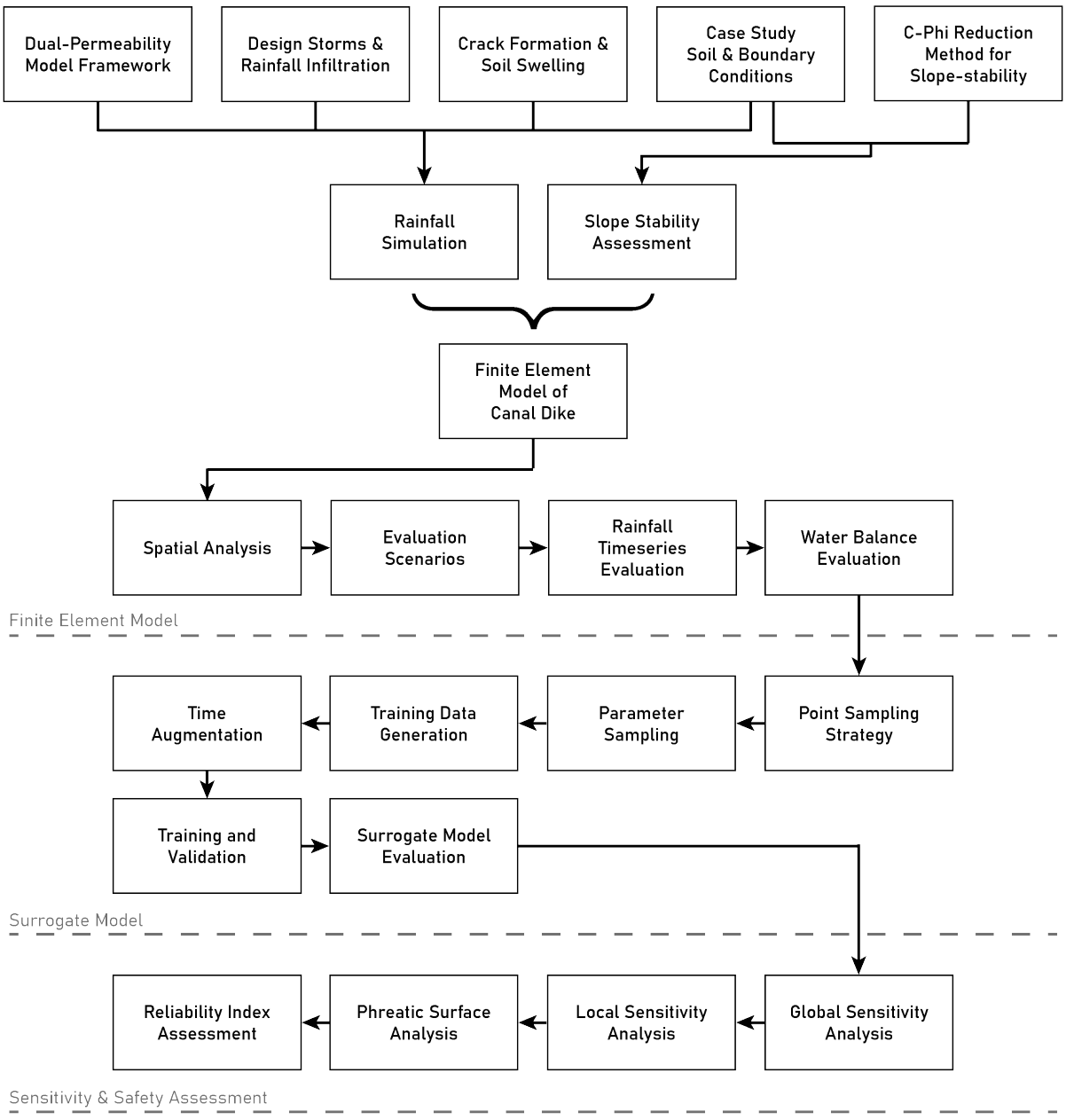

Figure 3: Flowchart displaying the methodology used in the thesis. The methodology can be subdivided into the finite element model, surrogate model, and sensitivity and safety assessment.

The first part of this thesis concerns the development of the finite element model, which coupled a rainfall model with a slope stability assessment. This was done by studying the crack formation, the DPM framework, soil swelling, rainfall infiltration, design storms, and the C-Phi reduction method for the assessment of the slope stability. Subsequently, the gathered physical relations were translated into the FEM using the finite element software of COMSOL. Four study parameters were selected to study the synergy between the cracks and rainfall. A sandy clay canal dike with hypothetical surface cracks was modelled using monitoring data provided by HHNK (2015).

Preferential flow through this fractured topsoil was represented by adopting a DPM framework that solves the head-based formula of Richards' equation with an additional exchange term between domains. A spatial analysis was performed on two reference scenarios of low and high rainfall intensity. Subsequently, these reference scenarios were compared against evaluation scenarios which simplified the proposed model to study the influence of the model features. Additionally, a three-day rainfall timeseries was used to compare and evaluate the DPM with a single permeability model (SPM). This analysis evaluated the connectivity among the cracks. Finally, the water balance for the reference scenarios was evaluated.

The surrogate model buildup is discussed in the second part of this thesis. Points within the dike were sampled using a principle component analysis (PCA) of the high-intensity rainfall reference scenario. Then, parameter distributions were made for the four study parameters. Subsequently, a Latin hypercube sampling (LHS) technique was used to sample the input parameter sets in a "space-filling" manner. The FEM simulation was run for several LHS parameter sets to generate the training data sets. Each run produced a timeseries of the pore pressure distribution and factor of safety. These timeseries were augmented to create a larger training data set. The surrogate model adopted a machine learning architecture which was trained and evaluated.

The last part of this thesis concerns analyzing patterns extracted from the surrogate model. A global and local sensitivity analysis of the study parameters was conducted on seven representable rainfall patterns. Next, the pore pressure distributions from the output of the surrogate model were spatially interpolated to determine the location of the phreatic surface. Finally, a reliability assessment compared the reliability index per return period for each rainfall pattern to the minimum reliability index set by Dutch legislation.

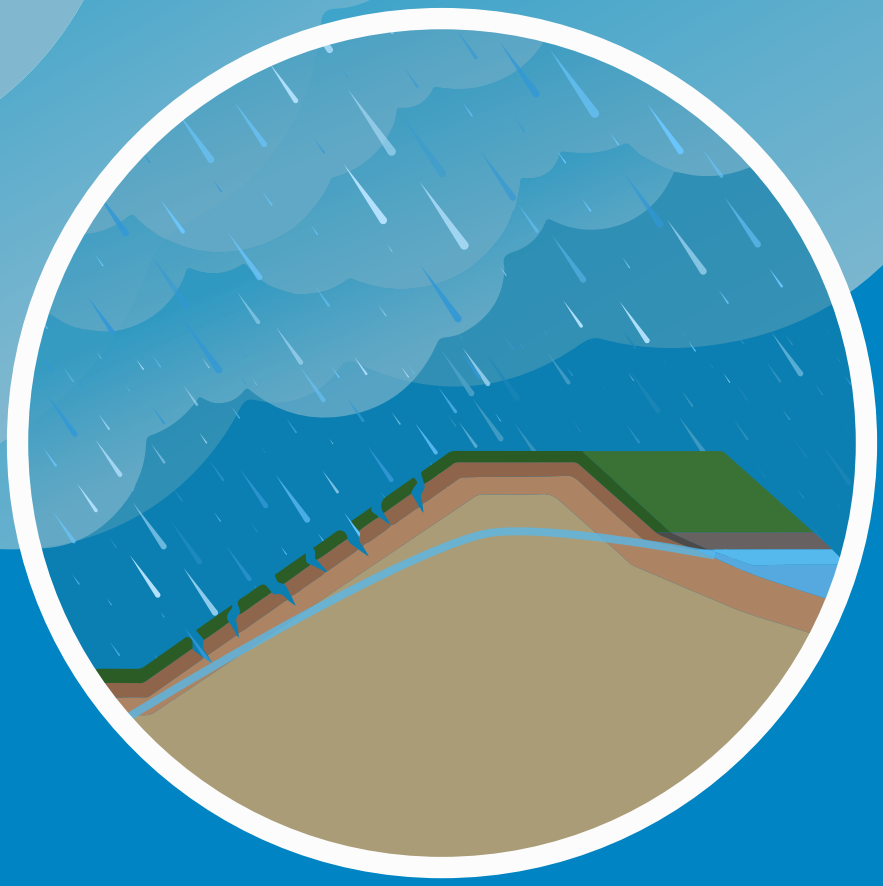

2. Finite Element Model

2 Finite element model

A COMSOL finite element model was constructed to quantify the influence of the soil cracks. This FEM utilized Richards' equation in a continuous DPM to study the pore pressure changes due to rainfall infiltration on cracked soil. Additionally, the slope assessment in the FEM quantified changes in the macro-stability of the dike. An FEM in its raw form is an approximation method that subdivides a complex problem of space into finite smaller elements. A FEM is often applied to model partial differential equations over a domain with imposed boundary conditions. Furthermore, it provides the modeller flexibility in accuracy and visualizations (Fong, 2019).

This chapter explains the framework and development of the finite element model in section 2.1. Subsequently, the model results for two reference scenarios are analyzed in section 2.2. Finally, in section 2.3, an evaluation of essential model features such as the connectivity of the cracks, the DPM framework, and soil swelling is made.

2.1 Methodology

2.1.1 Theory

2.1.1.1 Formation of cracks

Prolonged droughts decrease the phreatic level in a dike through seepage, enlarging the unsaturated zone in the top of the dike. Soil shrinkage of a clay soil can be summarized in two phases: first vertical deformation (subsidence) occurs, followed by vertical and horizontal deformation (Chotkan et al., 2022). In the first phase, the decrease in volume is equivalent to the reduction in water content, but the soil remains fully saturated. Cracks form in the second phase, where the matrix dimensions reduce from D_0 to D, and the matrix volume decreases from V_0 to V (Figure 4). In the latter phase, dry conditions induce an increase in matrix suction which draws soil particles closer together, effectively decreasing the volume and increasing the density (van den Akker et al., 2014). Irreversible shrinkage occurs when soil swelling during rainfall does not close the cracks formed after drying (van den Akker et al., 2014).

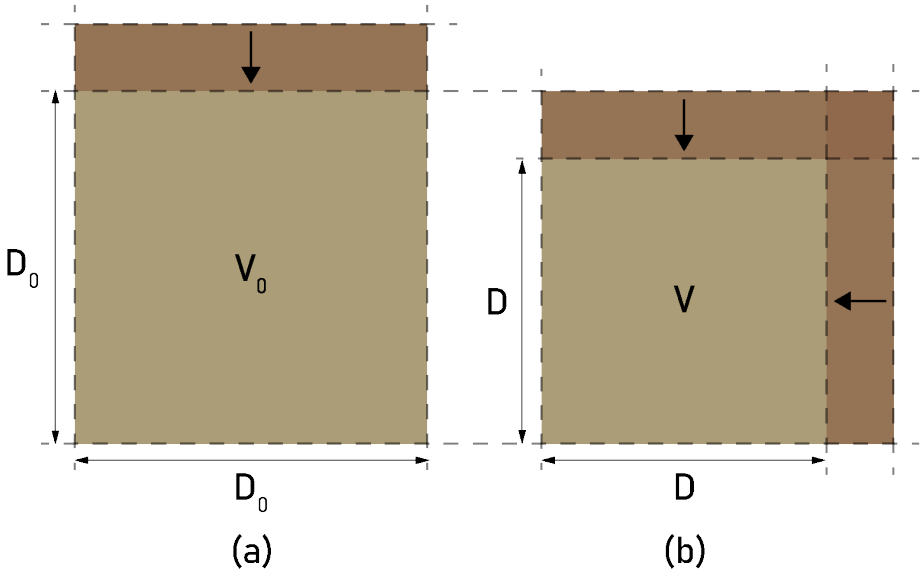

Figure 4: (a) Indicates the first phase of soil shrinkage which is dominated by subsidence. (b) Shows the horizontal and vertical deformation in the second phase of soil shrinkage (Chotkan et al., 2022).

The FEM built in this study does not include the formation of the cracks, as it was assumed cracks only form on the surface of the dike, where seepage occurs.

2.1.1.2 Preferential flow and DPMs

One of the main obstacles of physical modelling is the complexity of the real system. Preferential flow is a collective term used to describe rapid, uneven water flow through porous media, often exhibiting widely different velocities than the rest of the medium (Beven & Germann, 2013). Preferential flow describes a variety of heterogeneities in

porous media, such as flow along roots or fractures and cracks. The major drawback of modelling a system with preferential flow is that the preferential flow path properties are often "camouflaged" by averaging permeability properties in space (Hendrickx & Flury, 2001). Hence, it limits our ability to predict flow through porous media (Gerke & Van Genuchten, 1993a). DPMs are often used to overcome this drawback. In these models, two interacting domains: the matrix and the fracture domain, represent the complete porous medium. By representing preferential flow as a separate overlapping domain, it is treated as a homogeneous medium with vastly different flow properties. This approach also significantly reduces the computational burden as conventionally macropore flow through fractures is approximated by a Navier-Stokes type of numerical solution since it behaves more like a fluid pressurized conduit (Gerke & Van Genuchten, 1993a; Aguilar-López et al., 2020).

A DPM was adopted in which both overlapping domains are solved simultaneously as porous media continuum models using the 2D Richards' equation in head-based form. The DPM framework applied in this study was first introduced by Gerke & Van Genuchten (1993a). The volumetric ratios of the fracture and matrix domain in a DPM framework are derived from the representative elementary volume (REV) (Equation 1). The subscript of the matrix domain is denoted by an (m) and the fracture domain by an (f).

$$w_m + w_f = 1 \tag{1}$$

(w_m) $[-]$ and (w_f) $[-]$ are the volumetric ratios of the matrix and fracture domains, respectively. The volumetric ratio of the fracture domain is determined from the top projection at the surface. (w_f) is approximated as the superficial fracture porosity (n_c) $[m^3/m^3]$ by the following relation (Aguilar-López et al., 2020). Hence, this porosity is defined as the ratio between the fracture void area with respect to the total soil area. (J. Li & Zhang, 2010).

$$w_f = \frac{b}{b+a} \tag{2}$$

(b) $[m]$ is the fracture aperture length, or crack width, and (a) $[m]$ is the width of the average matrix block size. This relation only applies to fractured clay topsoil and is not representative of the remaining soil. The volumetric ratios of the remaining soil are set to 0.5, making the two domains identical for the remaining soil. Hence, the DPM framework simulates preferential flow in only the top layer.

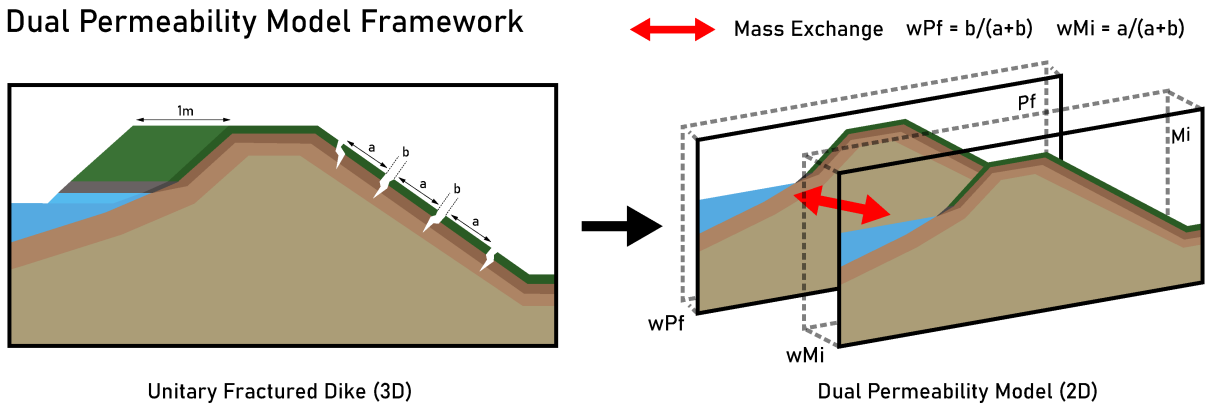

Figure 5: Dual permeability model framework showing the division of the volumetric fractions of the topsoil and the mass exchange between domains (Aguilar-López et al., 2020).

By approximating the volumetric ratios in this manner (see Figure 5), the total water content of the superimposed systems remains equal to that of a single permeability system. In the same manner, the total porosity (ε) $[m^3/m^3]$, the total moisture content (θ) $[-]$, the total volumetric flux (q) $[m/s]$ and the saturated hydraulic conductivity (K) $[m/s]$ can be decomposed based on their respective volume fractions.

$$\varepsilon = w_m \varepsilon_m + w_f \varepsilon_f \tag{3}$$

$$\theta = w_m \theta_m + w_f \theta_f \tag{4}$$

$$q = w_m q_m + w_f q_f \tag{5}$$

$$K = w_m K_m + w_f K_f \tag{6}$$

After partitioning the volumes of the two domains, the head-based 2D Richards' equation formulation for each domain can be defined (Celia et al., 1990).

$$C_f(h)\frac{\partial h_f}{\partial t} = \nabla[K_f(h)\nabla(h_f + z)] - \frac{\Gamma_w}{w_f} \tag{7}$$

$$C_m(h)\frac{\partial h_m}{\partial t} = \nabla[K_m(h)\nabla(h_m + z)] - \frac{\Gamma_w}{w_m} \tag{8}$$

$$\Gamma_w = \alpha_w^* K_a(h_f - h_m) \tag{9}$$

$$\alpha_w^* = \frac{\beta\gamma_w}{(a/2)^2} \tag{10}$$

(C) $[1/m]$ denotes the specific water capacity of each respective domain. The exchange term (Γ_w) $[1/s]$ governs the head-driven exchange between the two domains. (K_a) $[m/s]$ is the interface hydraulic conductivity and (α_w^*) $[m/s]$ is the first order exchange coefficient. Several factors define this coefficient. (β) $[-]$ is a factor that depends on the shape of the aggregates and is equivalent to 3, (γ_w) $[-]$ is a scaling coefficient equal to 0.4 (Gerke et al., 2007) and a scaling factor which is approximated as half the width of (a) $[m]$. Since the layers that are not cracked cannot be approximated by Equation 2, the (a) of these domains is defined as $0.1mm$ to represent a rapid transfer between domains.

The hydraulic properties of each domain are approximated with the Mualem-van-Genuchten soil water retention curve (SWRC) (Van Genuchten, 1980).

$$S_e(h) = [1 + (|\alpha h|)^n]^{-m} = \frac{\theta - \theta_r}{\theta_s - \theta_r} \tag{11}$$

$$K(S_e) = K_s S_e^{0.5}[1 - (1 - S_e^{1/m})^m]^2 \tag{12}$$

The (S_e) $[-]$ denotes the effective saturation, (h) $[m]$ is the pressure head, (α) $[1/m]$ is the scaling fitting parameter, (m) and (n) $[-]$ are fitting parameters related to the pore distribution (if l=0.5, $m = 1 - 1/n$ for Mualem-van-Genuchten), (θ) $[-]$ is the water content, (θ_r) $[-]$ is the residual volumetric water content, and (θ_s) $[-]$ is the saturated volumetric water content. Finally, $(K(S_e))$ $[m/s]$ is the approximated hydraulic conductivity as a function of the effective saturation.

Several studies have aimed to reduce the complexity of solving two coupled Richards' equation systems by constructing composite SWRC (Chertkov & Ravina, 2001). While this simplifies the formulation, the dynamic exchange between the two domains must be addressed. Aguilar-López et al. (2020) improved the DPM conceptualization by estimating representable SWRC Van Genuchten parameters of the fracture domain for a complete hollow cavity and realizing a more suitable exchange function to capture the dynamic exchange between the domains. They tested the performance of several exchange functions and found that the $K_{a_{min}}$ formulation showed the best performance when comparing it to an explicit model of the same setup (Aguilar-López et al., 2020). This formulation was originally introduced by Gerke et al. (2013) in which the lowest hydraulic conductivity value from each respective SWRC was evaluated with the largest pressure head value from both subsystems. Hence, the less permeable subsystem controls the head-driven flow at each time instance.

$$K_{a_{min}} = min\{K_m(h_f), K_f(h_f)\}, h_f \geq h_m \tag{13}$$

$$K_{a_{min}} = min\{K_m(h_m), K_f(h_m)\}, h_f < h_m \tag{14}$$

Solving Richards' equation in the fracture domain has several computational downsides. Due to this domain's high hydraulic conductivity and SWRC parameters, the domain dries very quickly. Infiltration into very dry soils, estimated by Richards' equation, results in very sharp wetting fronts. These wetting fronts lead to large spatial gradients of soil hydraulic properties. Thus, this introduces significant non-linearities, which are difficult to solve by Richards' equation (Miller et al., 2013). This increased the simulation time and often resulted in model crashes. To overcome this, a separate head-based SWRC was formulated and applied in which pressure heads above the field capacity of clay soil (-3.3m) (Assouline & Or, 2014) are fully saturated. This resulted in the fractures remaining saturated throughout the simulation. Aguilar-López et al. (2020) has indicated that a DPM of a fractured clay system on a small scale (0.19m by 0.19m) can reach saturation within 3.81s and the explicit model of the same system within 4.02s. Since storms that last hours were modelled, this error is negligible compared to the simulation time. While the SWRC parameters of the fracture domain are not used in the SWRC of the fracture domain, they are used in the exchange function governed by Equations 13 and 14.

Table 1: Hydraulic properties of the soil layers. [a,b,c,d,e] *(Aguilar-López et al., 2020; Mills, n.d.; Carsel & Parrish, 1988; Fan & Miguez-Macho, 2011; HHNK, 2015)*

Parameter	Cracked Sandy Clay	Sandy Clay	Peat
$\theta_{s,m}$ [-]	0.38[c]	0.38[c]	0.91[b]
$\theta_{s,f}$ [-]	0.99[a]	0.38[c]	0.91[b]
$\theta_{r,m}$ [-]	0.1[c]	0.1[c]	0.01[b]
$\theta_{r,f}$ [-]	0.01[a]	0.1[c]	0.01[b]
n_m [-]	1.23[c]	1.23[c]	1.3[b]
n_f [-]	4[a]	1.23[c]	1.3[b]
α_m [1/m]	1.65[e]	1.65[e]	1.41[b]
α_f [1/m]	1.41[a]	1.65[e]	1.41[b]
K_s, m [m/s]	7.5E-6[d]	1.5E-5[e]	4.5E-7[b]
K_s, f [m/s]	Variable	1.5E-5[e]	4.5E-7[b]
w_m [-]	Variable	0.5	0.5
w_f [-]	Variable	0.5	0.5
a [mm]	Variable	0.1	0.1

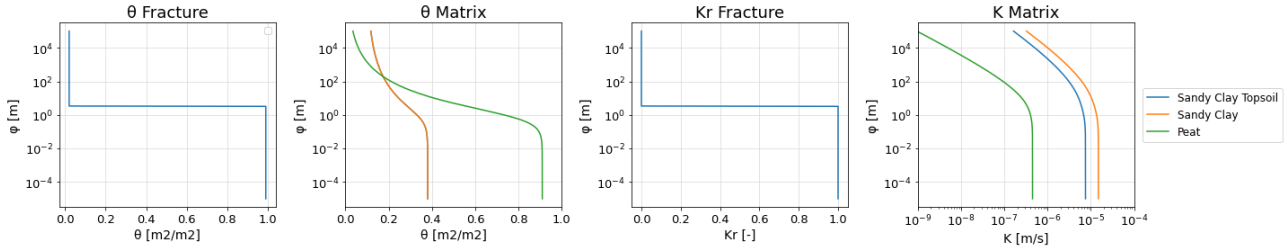

Figure 6: SWRC of the soils and fracture.

In Figure 6, the matric potential (Γ) is a function of the water content (θ), the relative hydraulic conductivity (K_r), and saturated hydraulic conductivity (K).

Flow through the fractures is approximated as laminar flow between parallel plates resulting in Hagen-Poiseuille flow. Snow (1965) proposed that the fracture's inner flux is related to the cube of the aperture of the fracture. This flux is then related to flux in Darcy's law to yield an approximation of the hydraulic conductivity inside a fracture. This equation assumes an absence of tortuosity in the fractures.

$$K_3 = \frac{b^2 g}{12\nu} \tag{15}$$

where (b) [m] is the aperture length of the fracture, (g) [m/s^2] is the gravitational acceleration constant, and (ν) [m^2/s] stands for the kinematic viscosity of water.

2.1.1.3 Soil Swelling

Many soils rich in clay content swell when wetted and subsequently shrink after drying. This phenomenon severely affects the saturated hydraulic conductivity of these soils. Many models neglect this dynamic behavior of clay-rich soil and rely on the simplification that most water flows through the cracks as they are the medium of least resistance (Novák et al., 2002). Furthermore, most DPMs consider the volumetric ratios of each respective domain to stay constant in time and space. These models restrict the dynamic behavior of the swelling in clay-rich soils by disconnecting the hydraulic properties from the domain.

Early studies by Messing & Jarvis (1990) and Jabro (1996) conducted field measurements of the saturated hydraulic conductivity of clayey soils. They found that the saturated hydraulic conductivity in these soils is a function of the water content. Furthermore, they recorded the highest field saturated hydraulic conductivity at a low antecedent water content. This is due to dry conditions where the cracks accommodate preferential flow paths. As the water content rises, the cracks begin to seal, and the saturated hydraulic conductivity decreases significantly. These field measurements reinforce the dynamic feedback between the soil cracks and their hydraulic conditions.

The wetting and shrinking of the cracks induces changes to the porosity distribution (Stewart et al., 2016) as shown in Figure 4. This porosity distribution is directly related to the saturation of the soil. While the occurrence

of soil subsidence was acknowledged, it was neglected in this study to conform to the conventional DPM setup, where the volumes are divided into the matrix and fracture domain. In this study, the volume fraction change over time depends on the change in fracture aperture defined by the superficial fracture porosity (Equation 2). Due to computational limitations, the minimum volumetric ratio of the fracture domain was set to 0.2%.

Stewart et al. (2016) studied the hydraulic properties of a multi-domain (matrix and fracture) clay-rich soil and proposed a model framework to capture this dynamic behavior. In this study, swelling dependent flow through the cracks is accounted for by the changes in matrix properties. This means that the width of the cracks is directly dependent on the saturation of the matrix. To simulate that the cracks have their highest saturated hydraulic condition when the soil is dry ($S_{e,m} = 0$) and their lowest when the soil is wet ($S_{e,m} = 1$), Stewart et al. (2016) defined the following relation:

$$b_f = b_{f\,max}\left(\frac{1 - S_e^q}{1 + pS_e^q}\right) \tag{16}$$

Where (b_f) [m] is the aperture of the fracture, ($b_{f\,max}$) [m] is the maximum fracture width and (p) [$-$] and (q) [$-$] are fitting parameters for the soil shrinkage curve. The chosen fitting parameters are 2 and 4.1, respectively, based on a study by Messing & Jarvis (1990), which investigated a clay soil with high clay content.

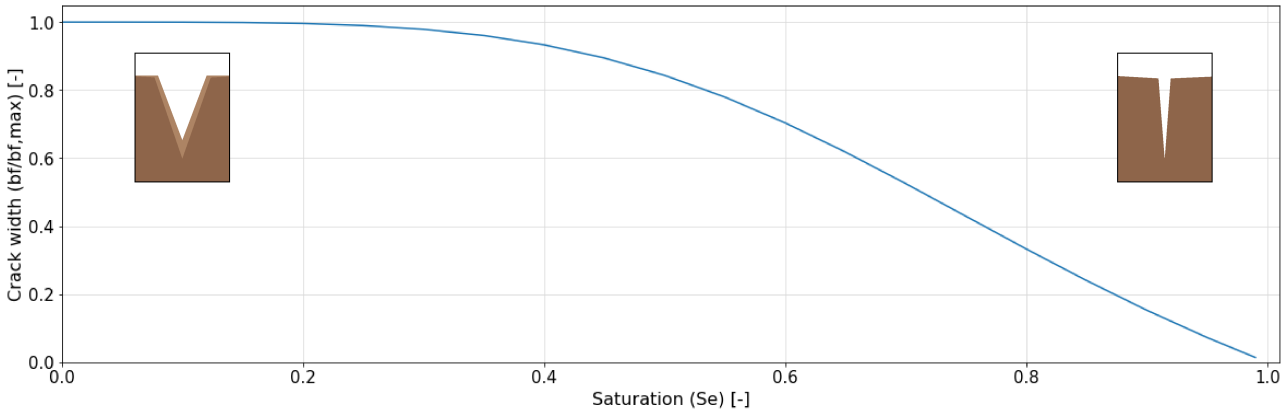

Figure 7: Crack width as a function of the effective saturation of the matrix domain.

By substituting Equation 16 in Equation 15, the dynamic saturated hydraulic conductivity is estimated as a function of the effective saturation of the matrix at the surface. According to Equation 16, the crack width changes proportionally for all cracks in the same domain. At first, this relation was applied to every point in the domain. However, only the fractures on the surface closed due to the localized dependence of the size of the cracks on the saturation of the matrix. This left the bottom fractures dry and wide as the fractures fill from top to bottom in the DPM continuum. For this reason, the fractured topsoil was decomposed into several subdomains, which ensured that the cracks changed width uniformly in each subdomain of cracked topsoil.

After the cracks observed a uniform decrease in width during the rainfall event, the cracks remained closed and did not open with a decrease in matrix saturation. This consideration was implemented based on the assumption that the drying time of these cracks is longer than the relevant study time frame. Kodikara et al. (2004) found that the drying time from supersaturation (more than 100%) to residual saturation can take up to several days in a fractured clay soil.

2.1.1.4 Rainfall infiltration boundary

Infiltration in a soil matrix is governed by two modes of transport (Novák et al., 2000): 1) vertical infiltration at the surface and 2) lateral infiltration via soil cracks. Most conceptual models aim to represent these modes of transport. Since the pressure-driven transport function between the two domains represents lateral infiltration between domains, the most notable point of discussion in DPMs is the vertical infiltration of water. The effect of preferential flow can provide rapid access to deeper soils and the underlying groundwater system (Vogel et al., 2000). Krzeminska et al. (2012) has shown that preferential flow paths increase the vertical infiltration rate, and therefore it is reasonable to assume differences in vertical infiltration rates between the two domains.

The boundaries at the top surfaces of the dike exposed to rainfall were difficult to conceptualize with a DPM as it relied on several assumptions of the fast infiltration behavior of the cracks compared to the matrix. Chui

& Freyberg (2009) introduced the mixed boundary condition necessary to conceptualize this rainfall-infiltration boundary on a homogeneous soil. This boundary involved switching between Neumann and Dirichlet boundary conditions depending on the solution at the surface of the soil as follows:

$$n \cdot \frac{K_s}{\eta} \cdot (p + \rho_f g z) = \alpha N_0 + \beta R_b (H_b - H) \tag{17}$$

The right-hand side of Equation 17 was implemented as a Neumann boundary condition in which one can switch between Dirichlet and Neumann conditions by alternating definitions of (N_0) $[m/s]$ and (R_b) $[1/s]$. The smoothing functions (α) $[-]$, β $[-]$ were used to avoid large shock effects during the alternation of the boundary conditions. These two boundary conditions describe a system filling with water and where the pressure head at the boundary governs which boundary condition is in effect.

As the system is filling due to rainfall infiltration, the non-head-dependent flux, (N_0), becomes equivalent to the precipitation rate, (P) [m/s], while the external resistance, (R_b), becomes 0.

$$N_0 = P \;\; R_b = 0 \;\; if \; H_p \leq 0 \tag{18}$$

In this case the pressure head on the boundary is less than 0. After the pressure head becomes larger than 0, the system is full and thus a ponding head will form. The non-head dependent flux will become 0 and the external resistance term will come into effect.

$$N_0 = 0 \;\; R_b > 0 \; , and \; H_b = z + h_{ponded} \;\; if \; H_p > 0 \tag{19}$$

Thus, the condition changes to a Dirichlet boundary with a ponding head, and this ponding head (h_{ponded}) $[m]$ can be a prescribed value or derived from a coupled surface model.

When implementing this alternating boundary condition, several parameters had to be parameterized based on the precipitation rate. The resistance term was defined as the quotient of the precipitation rate and the ponding head to ensure that the constant head boundary does not exceed the precipitation flux. Since implementing a coupled surface runoff model is outside the scope of this study, the ponding head at each instance was defined by the product of the precipitation rate and a time span of 1 hour. Finally, rainfall on slanted surfaces was corrected by a slope factor depending on the angle of the surface.

At first, the FEM included the division of excess fluxes between domains, once one domain became full. Implementing this resulted in sharp gradients in the rainfall boundary condition and ultimately crashed the simulation. The final FEM neglected this excess flux as it accounted for only a small portion of the total infiltrated volume. In general, Richards' equation governed the infiltration into the dike. Any excess rainfall unable to infiltrate was removed from the simulation. Therefore, the FEM did not account for overland flow when the infiltration capacity was exceeded during the rainfall event.

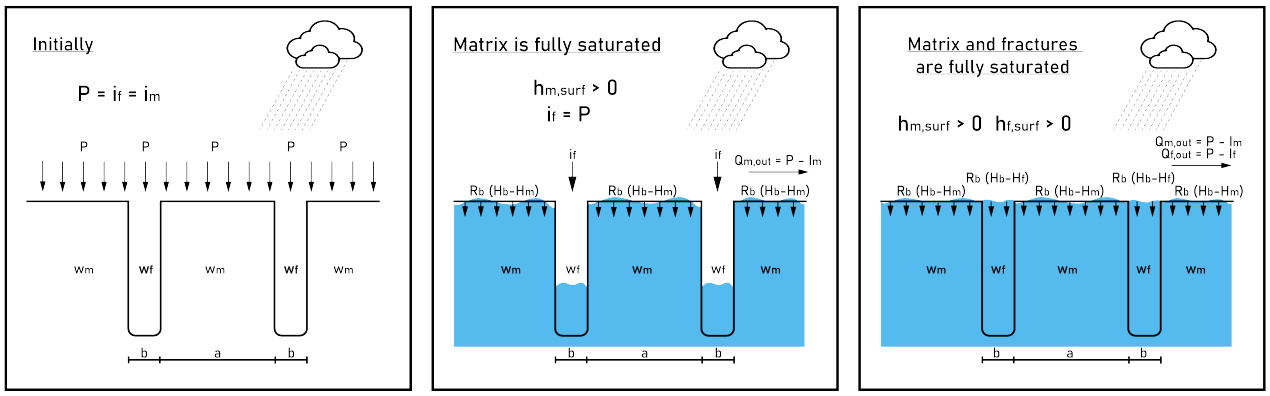

Figure 8: Implemented rainfall infiltration boundary assuming the matrix saturates first. I_f and I_m indicate the infiltration rate in each domain.

2.1.1.5 Design storm

Climatic conditions have a strong influence on the water flux through a dike. Several studies have observed an apparent increase in the steady state infiltration rate by increasing the rainfall intensity of a storm (Stone et al.,

2008; Dunne et al., 1991). Precipitation patterns of recent years were analyzed in a report by Beersma (2019) on precipitation statistics of the Netherlands. Besides confirming the climatic precipitation patterns mentioned in the fourth chapter of the latest IPCC report (IPCC, 2022) with localized statistics, precipitation intensity duration frequency (IDF) estimates were made to represent the entire calendar year. These estimates provide precipitation amounts of storms with a designated return period and associated duration lengths. The average rainfall intensity can be determined by dividing these rainfall amounts by their duration. A simple formulation of the power law (Chow, 1965) was calibrated based on annual precipitation amounts from Beersma (2019) to represent rainfall storms in the FEM. Equation 20 establishes a simple relation between the rainfall intensity, duration, and return period without requiring too many parameters to calibrate.

$$I = \frac{C T_r^m}{T_d^e} \tag{20}$$

Where (I) $[mm/h]$ is the rainfall intensity, (T_r) $[years]$ is the return period, (T_d) $[min]$ is the storm duration, (C) $[-]$ is a scaling coefficient and (m) and (e) $[-]$ are scaling parameters. After calibrating the scaling coefficient and parameters, it was found that applying this simplified equation overestimated rainfall intensities of short duration (less than ten minutes) and high return period (greater than ten years) storms. The calibrated scaling coefficient and parameters are 338.46, 0.27, and 0.75, respectively.

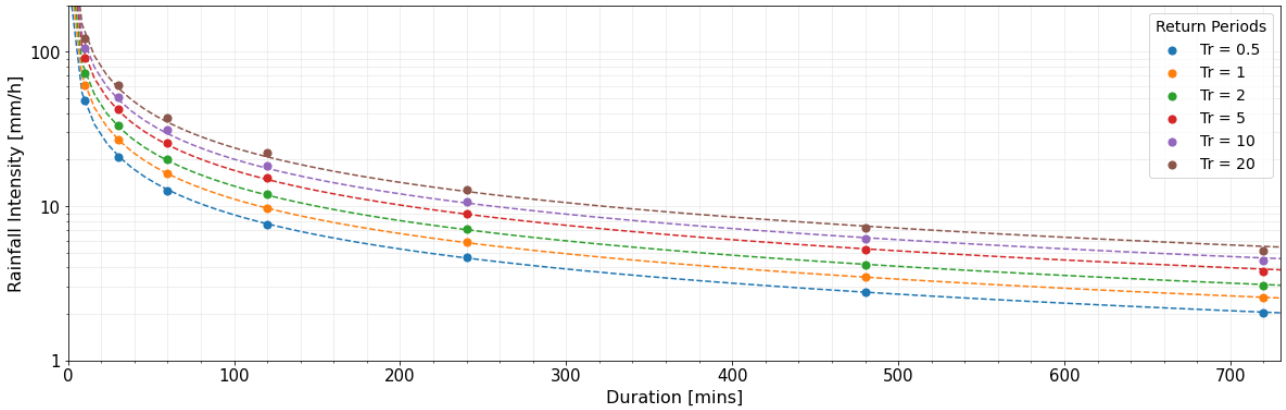

Figure 9: IDF curves and calibration points of various return periods.

A warm-up study preceded the main rainfall event simulation in the FEM. In this warm-up study, the FEM simulated a uniformly distributed rainfall event over two years with an average rainfall intensity of 659.6mm/year, which was the sum of the observed daily rainfall excess (rainfall - potential evaporation) at the site in the year 2014.

Storms can adopt many different temporal and spatial patterns. Hydrologists have utilized design storms for numerous applications, including designing drainage systems and rainfall-runoff modelling (Balbastre-Soldevila et al., 2019). These design storms are synthetic idealized storms often based on precipitation patterns. Smits et al. (2004) analyzed the temporal variation in precipitation amounts for several types of design storms in the Netherlands. These synthetic storms can have several different arrangements and may vary in the number of peaks, the size of the peak(s), and the distribution surrounding the peaks. In the FEM, the synthetic storm shape was translated into a hyetograph, conventionally shown by a histogram of fractions of the total precipitation amount (Figure 10). The hyetograph's shape depends on the storm type, which can vary in duration, maximum precipitation depth, total cumulative depth, and temporal distribution. Since an infinite number of combinations can represent the design storm, the hyetograph for each model was made based on 20 random bins. These random bins produced numbers between 0 and 2 and were multiplied by the average rainfall intensity. Therefore, the maximum possible rainfall intensity was twice the average rainfall intensity. This maximum was chosen to limit the simulation time for each run.

The hyetograph is often represented by a histogram of evenly spaced intervals (Figure 10). However, this led to sharp transitions between each consecutive bin, which resulted in longer computational times and more numerical instability. Therefore, a piecewise cubic interpolation was applied between consecutive discretized bins to increase the computational speed. However, using piecewise cubic interpolation over the nearest neighbor interpolation (with discretized bins) resulted in a slight difference in the moisture content of only 0.0033m2 for a high rainfall intensity simulation run. Hence applying a piecewise cubic interpolation has a negligible effect on the observed change in moisture content.

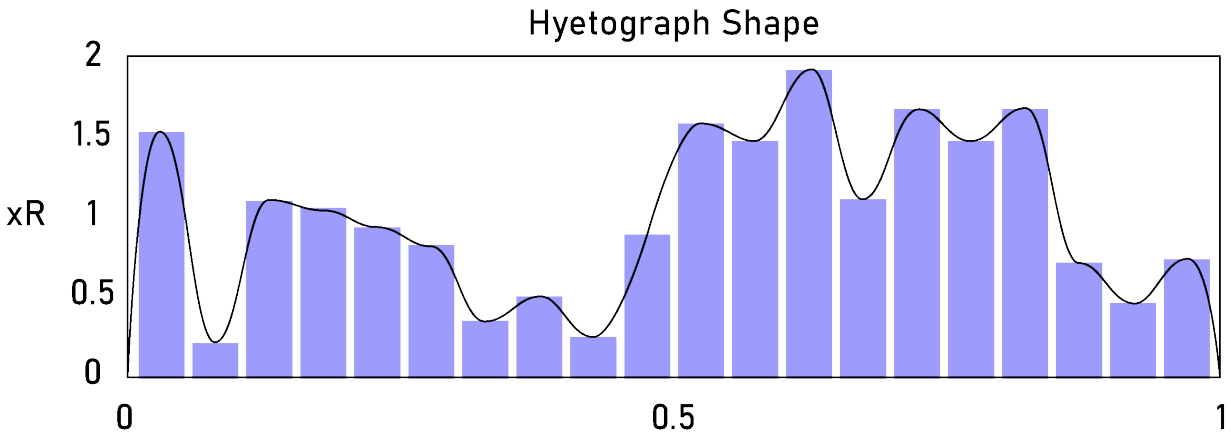

Figure 10: Randomized hyetograph based on 20 random bins which are multiplied by the average rainfall intensity (R). The black line represents a piecewise cubic interpolation over the histogram.

2.1.1.6 Slope stability

The factor of safety (FOS) is required to predict the degree of safety of a dike slope and must comply with the predefined Dutch safety standards (Kanning et al., 2017). The FOS is formally expressed as the ratio of resisting and driving forces within a slope. A FOS larger than one implies a stable slope. In this study, the FOS was determined to describe the macro-stability of the dike and how it was affected by rainfall infiltration.

A C-Phi or shear reduction method was used to determine changes in FOS over time. In this method, the strength of the soil is reduced by a parameterized FOS until failure occurs. By multiplying the reciprocal of the FOS with the cohesion and the internal friction angle, the strength of the soil is uniformly decreased (Dawson et al., 1999). Through several iterations, the FOS is determined at which the slope failed. This iterative process was conducted at several timestamps within the simulation time. In the C-Phi reduction method, no assumptions on the location of the failure plane need to be made (Dawson et al., 1999). Matrix suction affects the shear strength of the soil by altering the cohesion (c') $[kPa]$ and effective angle of friction of the soil (Φ') $[deg]$. Abd et al. (2020) found that the soil increases its effective angle of friction as the matrix suction increases. For this reason, the effective angle of friction of the fully saturated soil was multiplied by an arbitrary factor of 0.9 in the FEM. The C-Phi reduction method was performed by altering the cohesion and the effective friction angle in Equations 21 and 22.

$$c'_{n+1} = \frac{c'}{FOS_{n+1}} \tag{21}$$

$$tan\Phi_{n+1} = if(H_p < 0, \frac{tan(\Phi')}{FOS_{n+1}}, 0) + if(H_p \geq 0, \frac{tan(0.9\Phi')}{FOS_{n+1}}, 0) \tag{22}$$

An initial FOS of 0.8 was adopted for numerical stability, and the FOS was linearly increased in increments of 0.01 until failure occurred. The target FOS for each timestamp was the FOS at which the simulation failed. Due to time constraints, only 20 timestamps were evaluated to form the FOS timeseries.

The estimation of the stresses was derived from the pore pressures of the matrix domain. Additionally, the density of water was approximated by the volume of water in a single permeability system. In Table 2, (E) $[MPa]$ is the Young's modulus, (ν) $[-]$ is the Poisson's ratio and G $[g/cm^3]$ is the specific gravity of each soil. The specific gravity determines the soil's weight, which was used to determine the principal stresses within the dike.

Table 2: Soil material parameters [a,b,c,d,e] *(*Soil Profile CPT*, n.d.; Sharma et al., 1990; Teunissen & Zwanenburg, 2017; Lengkeek et al., 2018; Berhane, 2010)*

Parameter	Sandy Clay	Peat
c' [kPa]	10^a	5^a
Φ' [deg]	22.5^a	15^a
E [MPa]	5^a	0.5^c
ν [-]	0.2^b	0.45^c
G $[g/cm^3]$	2.7^e	1.4^d

2.1.1.7 Case study

In this study, a dike nearby Ursem in the Netherlands was modelled, and soil parameters were calibrated to emulate a realistic case study. Observational data on this dike was collected by HHNK (2015) and included cone penetration test (CPT) logs, daily precipitation amounts, and daily and hourly water levels at the relevant locations inside and outside the dike. This data was used to translate the dimensions and forcings of the dike into several domains and boundary conditions. The relevant locations for which monitoring data was provided is shown in Figure 11.

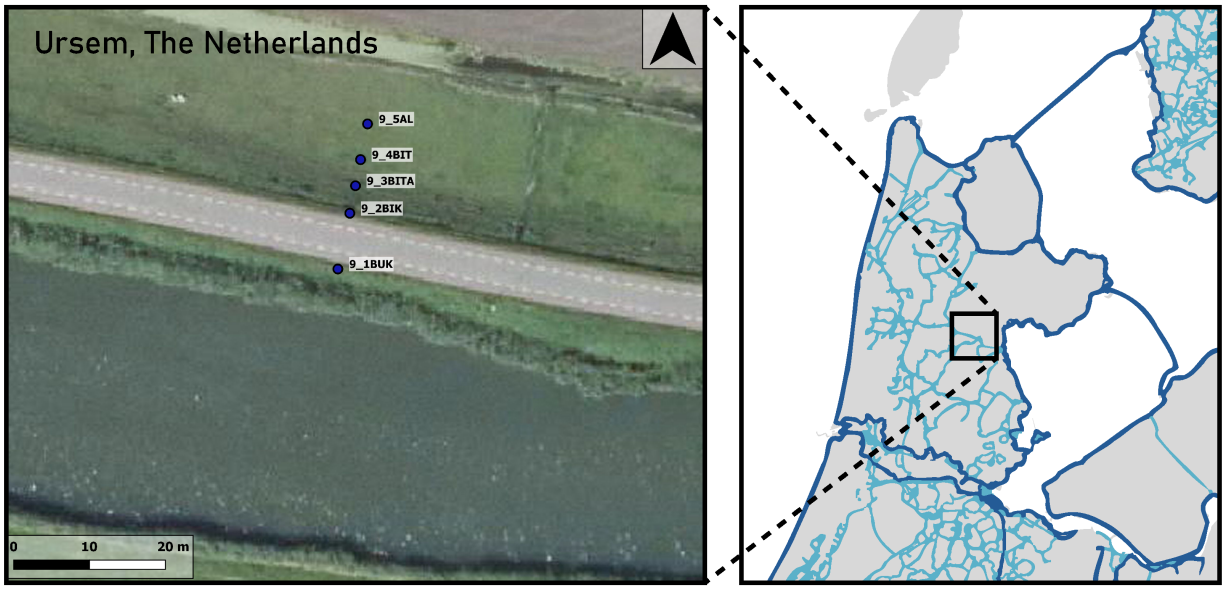

Figure 11: Location of dike and relevant monitoring stations (HHNK, 2015).

Five monitoring stations perpendicular to the canal were installed, and a road is found on the crest of the dike (Figure 11. For each monitoring station, the piezometric head was recorded every hour for roughly 15 consecutive months between 2013 and 2015. Additionally, the water levels in the canal and the toe ditch were recorded every hour. From the CPT logs, it was determined that the majority of the dike is sandy clay soil with a small peat layer between the embankment and the aquifer. In the sandy clay soil, there are several consecutive sand and clay layers, indicating the heterogeneity of the soil layers within the dike. However, these were all approximated as one large soil with homogeneous hydraulic and geotechnical properties. Therefore, the modelled hydrological response and safety factor can differ from the actual dike.

The model implemented three different layers: a peat layer, a sandy clay layer, and a cracked sandy clay layer (see Figure 12). Since this study investigated only the effect of cracked topsoil, the volumetric ratio of each domain in all other soil layers was held constant at 0.5. While the matrix of the cracked topsoil was also approximated as a sandy clay layer, only the calibrated α was implemented (and not the calibrated overall saturated hydraulic conductivity). The matrix of this layer was assigned a lower saturated hydraulic conductivity as this layer was decomposed into two domains of different hydraulic properties.

A depth of 30cm was chosen for the cracked top layer and was held constant throughout each simulation. In reality, the depth of the cracked top layer is highly influenced by the saturation, which varies throughout the year and spatially within the dike. Since this cracked top layer is more prevalent in dry periods, this model setup most realistically represents the dry summer months.

The saturated hydraulic conductivity and the α parameter of the van Genuchten SWRC of the large sandy clay layer were calibrated using the observed daily and hourly water levels in the crest of the dike (Figure 12). The boundary conditions used in this calibration were the observed water levels in the canal and toe ditch and the observed precipitation from the nearby KNMI station. The daily observations were a good measure to estimate the overall saturated hydraulic conductivity, whereas the hourly observations were a good measure of the immediate hydrological response. Hence, the hourly data was used to calibrate the α parameter. After this calibration procedure, it was found that the overall saturated hydraulic conductivity of the sandy clay soil (not the cracked

topsoil) was 1.5×10^{-5} m/s and the α parameter 1.65 1/m. It should be noted that these parameters were averaged over the entire soil and included the response of the matrix and preferential flow paths. Since the saturated hydraulic conductivity of clay soils was, on average, significantly lower than the calibrated saturated hydraulic conductivity, it can be concluded that the high saturated hydraulic conductivity of the preferential flow paths increased the overall saturated hydraulic conductivity. The hydraulic and material properties of all layers, except for the parameters calibrated for, were determined from the literature.

The FEM implemented three boundary conditions to simulate rainfall infiltration into a loaded canal dike. First, a no-flow boundary was considered at the bottom and on the crest of the dike at the road's location. Furthermore, the model implemented a constant pressure head on the left and right sides to simulate the water level in the canal and the toe ditch. These were approximated as the average water levels during the recorded observation time. Finally, a flux boundary was defined on the remaining surfaces to approximate the rainfall infiltration. These boundary conditions were applied to both domains to approximate the model as a continuum DPM.

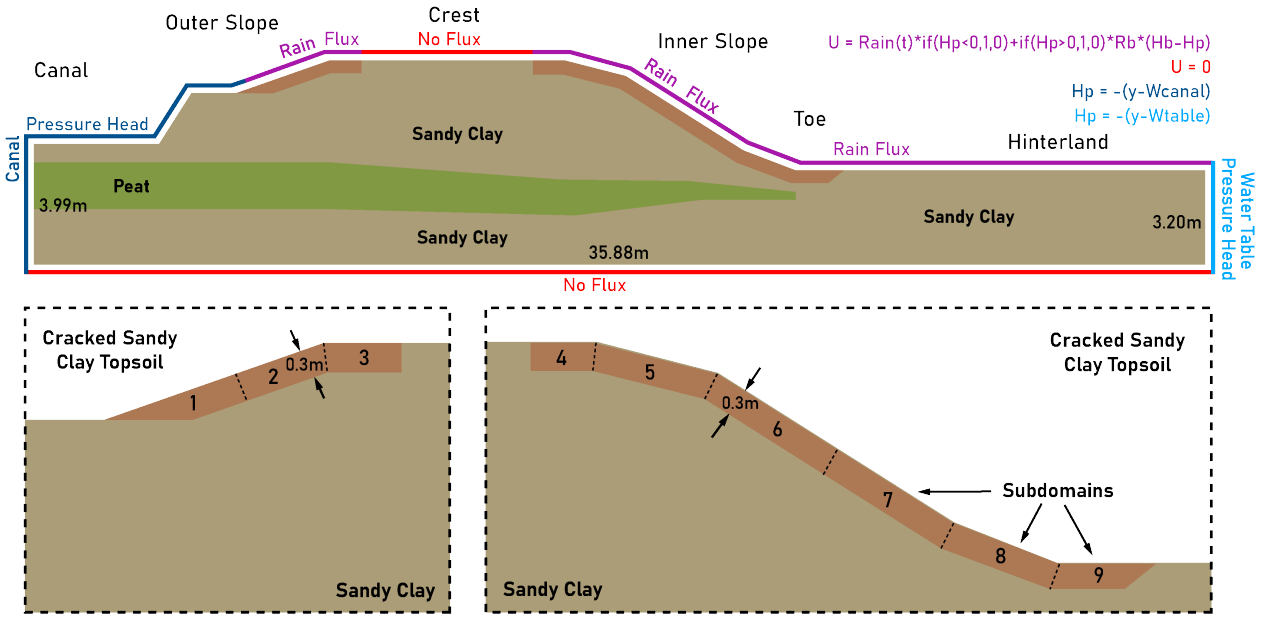

Figure 12: Implemented domains, boundary conditions and important regions of the dike. The subdomains for the cracked topsoil are indicated by the lower figures.

2.1.2 Simulated hydrology & study parameters

The hydrology in the dike depends on the imposed boundary conditions. While the influence of rainfall infiltration was studied, the influence of evaporation was neglected. This study assumed that the magnitude of the daily potential evaporation was negligible compared to the magnitude of rainfall infiltration during the storm extent. Since evaporation was neglected, the dike can only dry through the drainage of water at the boundaries. Water inflow is largely determined by the water level behind the dike and rainfall infiltration, while water outflow depends on the phreatic surface relative to the domain boundaries. Overland runoff was not considered, and all the water that could not infiltrate was neglected. Additionally, exchange between domains can lead to more or less water inflow and outflow. This exchange depends on the volumetric fractions of each domain. Hence, a larger water flux could be supplied from the matrix to the fracture domain based on its larger unitary volumetric fraction in the topsoil.

As mentioned, the study parameters were selected to investigate infiltration into fractured clay soil. Since water infiltration depends on the cracks and the rainfall, the study parameters were chosen to study their combined influence on infiltration and drainage. The chosen study parameters were the maximum width of the cracks (b), the initial volumetric crack ratio (wPf), the average rainfall intensity (R), and the associated return period of the storm (Tr) (Table 3).

The crack width and volumetric ratio decreased during the rainfall simulation due to soil swelling. Alternatively, the crack spacing grew in size, but the total considered length (a + b) remained constant throughout each simulation.

Table 3: Study parameters and their influence on the DPM

Parameter	Abbreviation	Model influence
Maximum crack width	b	Affects the crack width during the simulation and represents the crack width at the start of the simulation when the dike is dry. The observed crack width during the simulation decreases due to soil swelling and this determines the saturated hydraulic conductivity of the cracks.
Initial volumetric crack ratio	wPf	Describes the amount of cracking. Governs the exchange between the domains according to Equations 9 and 10. The volumetric crack ratio decreases during the simulation due to soil swelling
Average rainfall intensity	R	Affects the hydrological forcing applied at the rainfall boundaries. The hyetograph is determined by multiplying this parameter with a randomized rainfall pattern. Also affects the storm duration by Equation 20
Return period	Tr	Affects the storm duration by Equation 20. Ultimately also affects the total simulation time and the timesteps taken. The simulation time is taken as twice the duration of the storm to capture the drainage of the unsaturated zone.

At the start of the warm-up simulation, the initial volumetric ratio (wPf) and the maximum crack width (b) defined the initial crack spacing (a).

2.2 Results

2.2.1 Reference scenarios

Two reference scenarios were analyzed for low and high-intensity rainfall to observe the influence of the cracks on the hydrology and its resulting macro-stability. Hence, the cracks were studied under two different forcings (Table 4).

Table 4: Study parameters of the reference scenarios

	Parameters			
Storm	**b [mm]**	**wPf [-]**	**R [mm/h]**	**Tr [years]**
Low Rainfall Intensity	3	10%	2	5
High Rainfall Intensity	3	10%	20	5

2.2.2 Spatial analysis

The presence of cracks altered the infiltration pattern in the topsoil of the dike. The penetration depth of the wetting front during the storm is essential to the stability of the dike after the storm, as more infiltrated water can lead to a lower safety factor. Since the unsaturated zone drained after the storm, the phreatic surface will likely shift upward depending on the penetration depth. The infiltration flux and the exchange term fluxes were extracted for each reference scenario to determine the influence of the cracks on the hydrology(Figure 13). The infiltration fluxes were multiplied by their respective volumetric domain fractions.

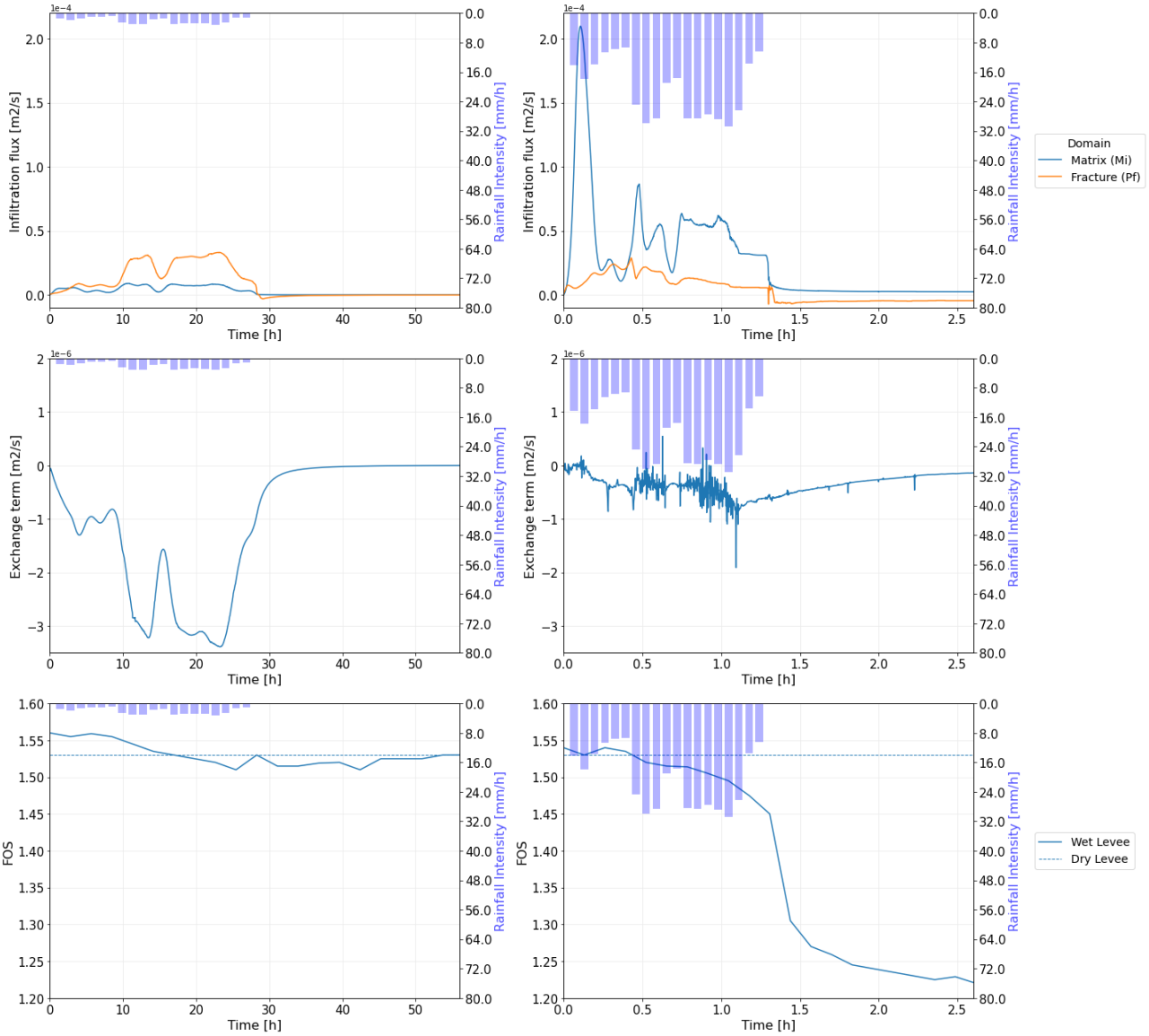

Figure 13: Infiltration and exchange term fluxes for the reference scenarios and their resulting FOS timeseries. A negative exchange term indicates flow from the matrix to the fractures.

The infiltration and exchange term fluxes both follow the shape of the hyetograph. For a low rainfall intensity storm, infiltration is dominated by the fracture domain, while during a high rainfall intensity storm, the infiltration is mostly dominated by the matrix domain. The swelling of the soil can explain this shift in dominating flux. Under the high-intensity rainfall scenario, soil swelling reduces the crack width in the cracks within the first ten minutes. This results in a large peak in infiltration by the matrix. The second peak in infiltration by the matrix is reduced due to the expansion of the pressure head boundary, which is lower in magnitude than the flux boundary imposed at the start of the simulation.

The exchange term represents the exchange fluxes without the volume fractions (Equation 9) and integrated across the cracked topsoil. When the exchange term is negative, the pressure head in the matrix domain is larger than that of the fracture domain, resulting in exchange to the fracture domain. In both simulations, this term is negative, indicating a larger total exchange flux from the matrix to the fractures. The average magnitude of this exchange term for a high-intensity storm is less than that of a low-intensity storm and observes more fluctuations. The extra source term in Richards' equation considers the product of this exchange term with the reciprocal of the volumetric ratio of each domain (see Equations 7 and 8). Since the fracture domain is very small, the source term for the fracture domain can be significant, which results in large head differences and some numerical instability.

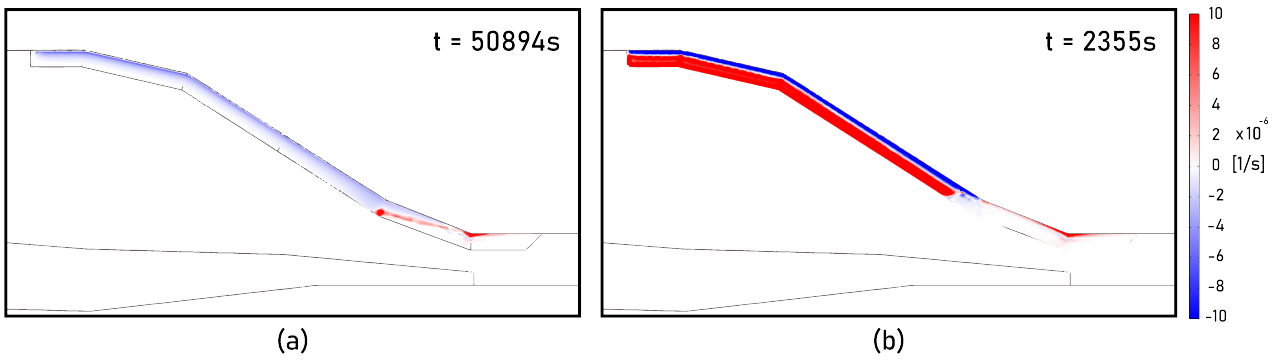

Figure 14: Exchange term halfway the storm duration for reference scenarios in the cracked topsoil in the inner slope of the dike: (a) Low rainfall intensity, long duration storm; (b) High rainfall intensity, short duration storm. A negative sign (blue) means exchange from the matrix to the fractures, while a positive sign (red) signifies an exchange from the fracture to the matrix.

The matrix exchanges water towards the fracture domain in a low rainfall intensity storm. Subsequently, water flows to the matrix domain below the phreatic surface. The high rainfall intensity storm reveals a different trend as, in the wetting front, water flows to the fractures, but below, water flows towards the matrix. This exchange of water below the wetting front can effectively increase the rate at which the wetting front advances through the topsoil, as it increases the local effective saturation of the matrix and increases the saturated hydraulic conductivity according to SWRC equation (Van Genuchten, 1980) (Equation 12), allowing for faster advancement of the wetting front. S. Li et al. (2021) found similar results, where the preferential flow domain allows the wetting front to penetrate deeper into the soil.

The low rainfall intensity storm leads to very little change in the phreatic line at the end of the simulation. In contrast, the high rainfall intensity storm results in a significant change as a region of positive pore pressures forms by the advancement of the wetting front. After the storm has passed, this accumulated wetting front is drained to the phreatic line and significantly impacts the shape of the phreatic line. Changes in the phreatic line are also reflected in the FOS timeseries (Figure 13).

2.3 Model Evaluation

Models that aim to reproduce physical phenomena require an evaluation to assess their resemblance with the real system. Therefore, field measurements of the studied phenomena are valuable when evaluating the model's performance. Several studies attempted to demonstrate the influence of meteorological conditions on changes in the phreatic line and unsaturated zone affecting the stability of the dike (Jamalinia et al., 2019; Monden et al., 2020; Rikkert, 2022). These studies demonstrated the difficulty in validating the results with field measurements. Complications in the model evaluation are largely the result of using an idealized model setup in which soil heterogeneity and varying boundary conditions are simplified. Jamalinia et al. (2019) determined the influence of meteorological conditions on the dike stability by adopting an idealized regional dike exposed to real meteorological conditions. Validation was not possible due to the homogeneous model setup, neglecting heterogeneity in the soil layers and hydrological properties. Similarly, Monden et al. (2020) modelled a dike under constant rainfall lasting several days and without using observed rainfall. Rikkert (2022) modelled several locations in a dike as a hydrological buckets model and used measurements to train and validate the model. While this approach allows for location-specific predictions of the phreatic line due to precipitation and evaporation processes, it cannot predict large changes in the unsaturated zone in response to rainfall. Matric suction can positively impact the dike stability, especially for highly cohesive soils (Hadži-Niković et al., 2015; Le et al., 2015). Hence a complete method for a reliable dike stability assessment requires measurement data well distributed in space, which is very difficult to obtain.

While the monitoring data provided by Hoogheemraadschap Hollands Noorderkwartier (2015) allows for a more realistic model setup, it could not be used for evaluating the model for several reasons. First and foremost, in this study similar to Jamalinia et al. (2019), a simplified homogeneous model setup was adopted in which the cracked topsoil is idealized. This allowed for the investigation of the impacts of such a layer. Since the data provided did not include a description of the presence of surface cracks, it was assumed that the modelled dike did not have a cracked topsoil. Therefore, in this study, the data from Hoogheemraadschap Hollands Noorderkwartier

(2015) could not be used to evaluate rainfall infiltration through cracks. Additionally, the CPT logs show that the soil layers are heterogeneous, and these layers were simplified and condensed in the model. Lastly, the temporal resolution of the provided meteorological data and recorded water levels is too coarse to capture the fast response of the cracks. For example, the recorded precipitation from high-intensity, short-duration storms is averaged over hourly intervals. Thus, these reasons result in a poor evaluation case using the provided data.

2.3.1 Model Feature Evaluation

To evaluate the DPM model established by this chapter, the model was compared to several scenarios in which specific features were removed and the impact of these features on the resulting FOS timeseries was highlighted.

2.3.1.1 Evaluation scenarios

The reference scenarios (Table 4) were compared with four evaluation scenarios (Table 5) to evaluate several model features. Additionally, a scenario without the influence of matric suction was investigated for all evaluation and reference scenarios.

Table 5: Description of evaluation scenarios and the type of model

Scenario	Model Type	Description
1	SPM	The top layer has a saturated hydraulic conductivity equal to that of the matrix of the sandy clay layer.
2	SPM	The top layer has a saturated hydraulic conductivity equal to that formed by static fractures (no swelling) imposed by the reference crack parameters.
3	DPM	A dual permeability model where soil swelling is restricted. Hence in all top layers the same crack width and saturated hydraulic conductivity are observed.
4	DPM	A dual permeability model almost identical to that of the reference. However, the bottom two fractured subdomains in the toe of the dike are removed and replaced with the underlying sandy clay layer. These are subdomains 8 and 9 (Figure 12)

The influence of the saturated hydraulic conductivity in the top layer was evaluated with the two SPMs (Table 5). These illustrate the two extremes given by a very low and high saturated hydraulic conductivity in the top layer. The final two evaluation scenarios evaluate soil swelling and the importance of the bottom cracks.

2.3.1.2 Feature comparison

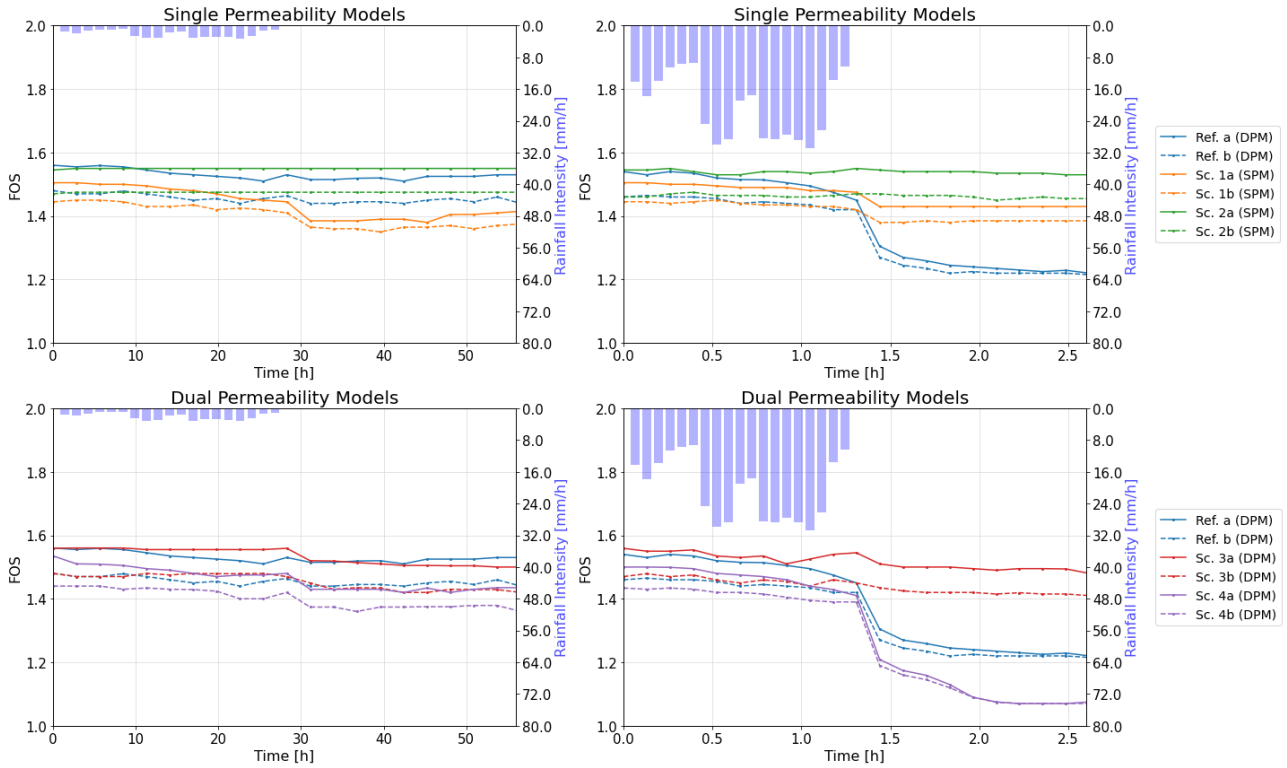

Figure 15: FOS timeseries of (a) reference/evaluation scenarios, (b) reference/evaluation scenarios without the influence of matric suction on the effective stresses.

As expected, the reference DPMs behave fundamentally differently from the evaluation scenarios, and large differences exist between low and high rainfall intensity storms. In general, the safety factor drops after the storm due to the drainage from the unsaturated zone, resulting in a rise in the phreatic surface. This subsequent drop in FOS after the storm is the largest for the reference scenario and scenario 4 under a high-intensity storm.

Comparing the scenarios establishes a trend with and without the influence of matric suction on the effective stresses in the slope stability assessment. The influence of matric suction can increase the factor of safety by 0.05 to 0.09 depending on the scenario and available water in the unsaturated zone. Scenario 1 has a smaller difference between the FOS timeseries with and without matric suction. This can be attributed to a smaller penetration depth of the wetting front due to the low hydraulic conductivity. The difference in FOS due to matric suction remains fairly constant throughout each scenario except for the reference scenario and scenario 4. These scenarios exhibit significant soil swelling in a high-intensity storm. This difference diminishes sharply after the storm, indicating a sharp decrease in matric suction due to the advancement of the wetting front (Mahmood et al., 2016).

Scenarios 2 and 3 reinforce the importance of drainage. Under a high rainfall intensity storm, scenario 2 results in a FOS that remains constant throughout the simulation. This is primarily the result of the high saturated hydraulic conductivity of the cracked top layer in the toe facilitating drainage for the dike. Scenario 3 displays a similar trend. These scenarios sharply contrast the reference scenario, where soil swelling or the absence of cracks restrict drainage in the toe of the dike. In the reference DPM, which included soil swelling, the toe of the dike is almost always saturated, resulting in a lower local saturated hydraulic conductivity. In contrast, the cracks in the top of the dike still accommodate for rainfall infiltration. Therefore, the accumulation directly relates to the residual influx due to local differences in soil swelling between the dike's top and toe regions. The spatial distribution of b and wPf before and after the rainfall simulation demonstrating soil swelling is shown in Appendix A. Scenario 4 depicts an even more dire scenario as there are not any cracks to accommodate drainage in the toe of the dike, hence more water is accumulated resulting in a sharper drop in FOS.

2.3.2 Rainfall Timeseries Evaluation

The influence of the cracks was also evaluated using a timeseries of recorded rainfall. An SPM was compared with a DPM with crack parameters equal to the reference scenarios (Table 4). The topsoil in the SPM had no cracks and adopted the calibrated saturated hydraulic conductivity. For three days, hourly rainfall from a nearby KNMI station was applied to the rainfall boundaries in both models to simulate rainfall infiltration. Furthermore, the connectivity of the cracks was evaluated by simulating additional evaluation scenarios.

2.3.2.1 Evaluation scenarios

In the crack evaluation scenarios, the underlying soil replaced the subdomains of the cracked topsoil (Table 6).

Table 6: Crack evaluation scenarios where the underlying soil replaced several cracked subdomains. The cracked subdomains are shown in Figure 12.

Scenario	Model Type	Crack subdomains replaced
5	DPM	8 & 9
6	DPM	7, 8 & 9
7	DPM	6, 7, 8 & 9
8	DPM	1, 2 & 3
9	DPM	7

Scenarios 5, 6 and 7, replaced the subdomains in the toe of the dike. By replacing one subdomain at a time, the severity of the reduced drainage paths was evaluated. Scenario 8 tested the influence of the cracks on the outer slope of the dike. Finally, scenario 9 replaced the middle subdomain on the inner slope to test the connectivity between cracks on the upper and lower inner slope.

2.3.2.2 SPM vs DPM

The FOS timeseries of an SPM without cracks was compared with the FOS timeseries of a DPM with cracks (Figure 16).

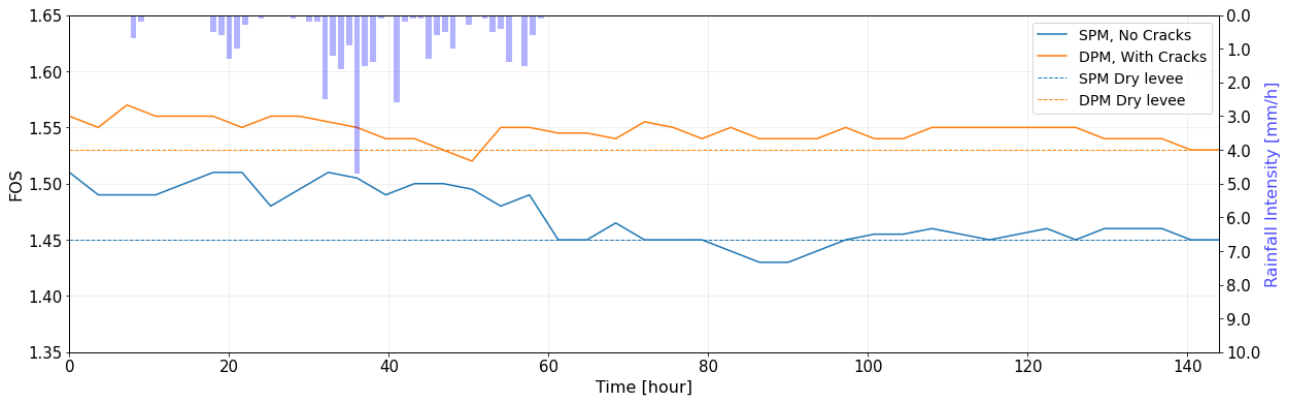

Figure 16: FOS timeseries for an SPM and a DPM with recorded rainfall.

At the start of the rainfall simulation, the FOS of the SPM maintains a considerably lower level than that of the DPM. Furthermore, the difference in FOS between the wet and dry dike is larger for the SPM than for the DPM (Figure 17).

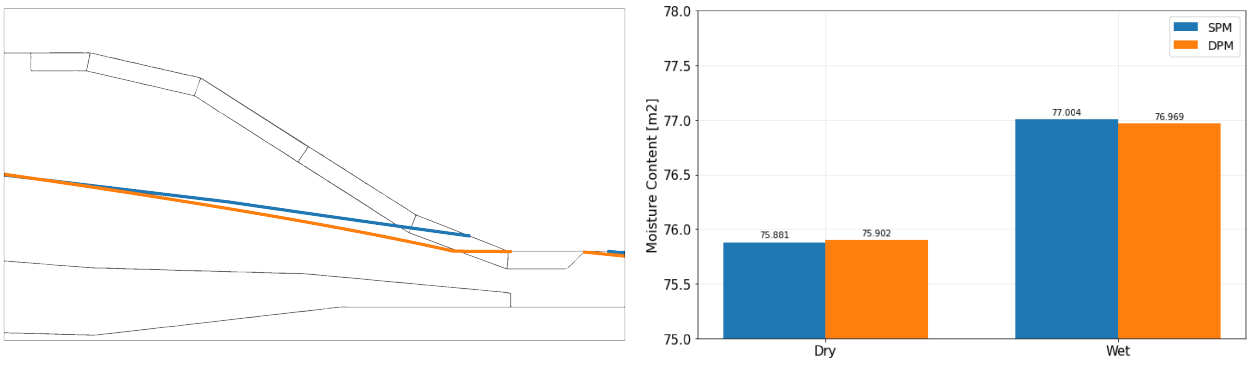

Figure 17: The location of the phreatic surface in the toe of the dike and the moisture content before and after the warm up period (dry and wet).

The cracks in the toe of the dike provide drainage to the DPM, which effectively lowers the phreatic surface and results in a higher FOS. The smaller difference in FOS between the dry and wet dike (before and after the warm up study) for the DPM can be attributed to the smaller increase in moisture content. Therefore, there is less water in the unsaturated zone to provide matric suction and increase the FOS. The SPM has a larger response to the recorded rainfall in terms of the FOS, both during and after storm (Figure 16). This indicates that the connected cracked top layer in the DPM facilitates drainage and reduces the buildup of positive pore pressures in the toe of the dike. As indicated by Figure 13, the larger increase in infiltration through the cracks does not always yield a lower FOS.

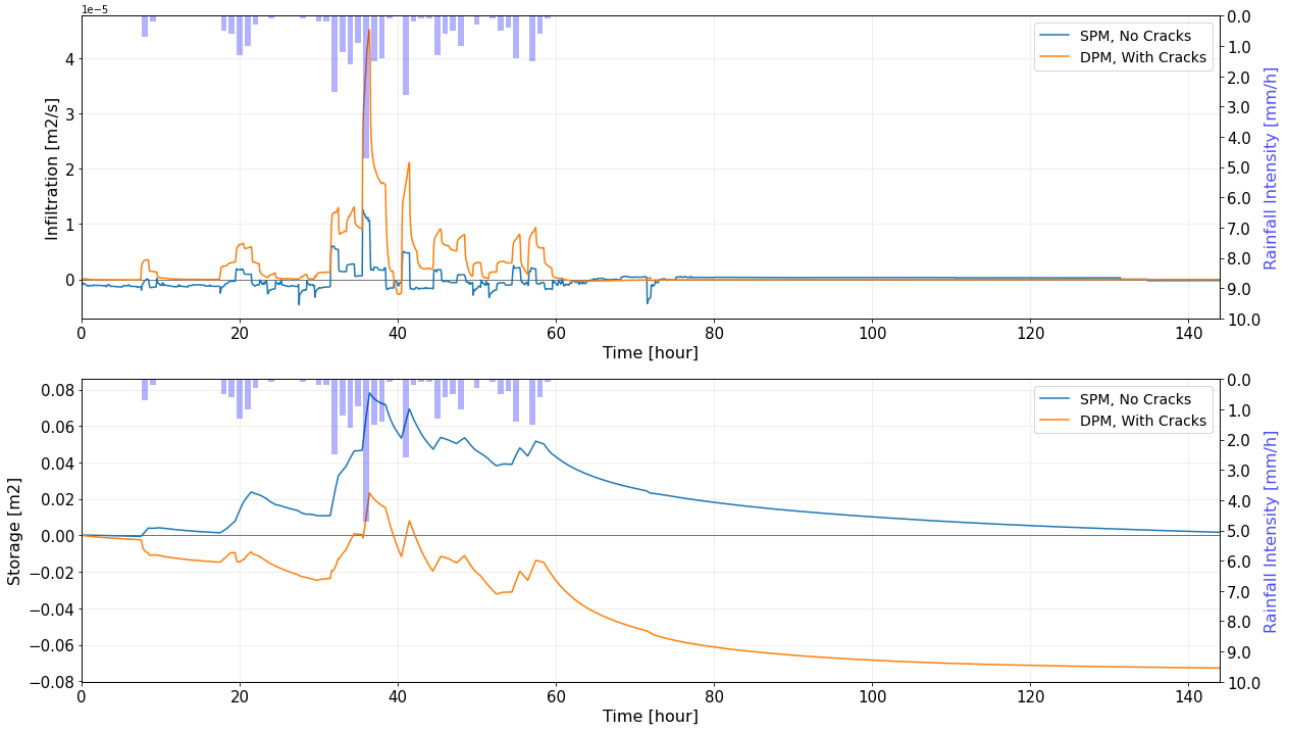

Figure 18: Infiltration through rainfall boundaries and the resulting change in storage or moisture content over time in the topsoil during the simulation. A negative change in storage means moisture content decreases, while a positive change in storage signifies an increase in moisture content.

While an SPM does not have a cracked topsoil, the topsoil is still discretized separately, but its properties are identical to the underlying soil. This allows for a similar comparison of the change in infiltration and water content in this region of the dike. Figure 18 reinforces the notion that the cracks allow for more infiltration while facilitating additional drainage. The amount of drainage is greater than the excess infiltration, thus resulting in a higher FOS and a safer slope. Contrary to the DPM, the SPM infiltrates significantly less while increasing the total water content during the simulation. This is because of the slower water movement through the topsoil in the SPM compared to the DPM.

2.3.2.3 Connectivity of the surface cracks

The likelihood of surface cracks forming on the inner toe is less than near the crest of the dike as the toe region is closer to the phreatic surface and more saturated. However, since the cracks can provide drainage, the local influence of the cracks on the dike's drainage ability was examined. Section 2.3.2.1 explains the studied crack evaluation scenarios, and Figure 19 evaluates the FOS timeseries produced by the FEM for these scenarios.

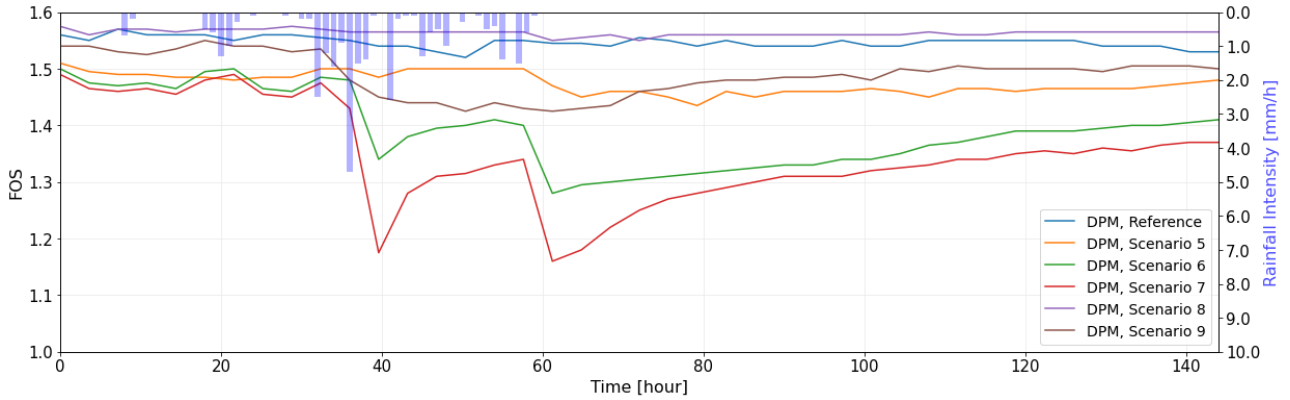

Figure 19: FOS timeseries produced by the crack evaluation scenarios and reference DPM model under observed rainfall.

The connectivity among the surface cracks affects the drainage of water out of the dike. Restricting drainage at the toe of the dike caused water to accumulate, severely affecting the macro-stability. Scenarios 5, 6, and 7 demonstrate how positive pore pressures build up to affect the phreatic surface and the macro-stability. Scenarios 6 and 7 also respond faster to the peak of the storm. Scenario 8 demonstrates that cracks on the outer slope have little influence on the FOS timeseries. Finally, Scenario 9, which replaced the middle crack subdomain on the inner slope, reveals that drainage mostly occurs along the connected cracked surface.

The connectivity of the cracked subdomains is essential to the drainage of the slope. However, this study only considers surface cracks. Surface cracks formed at the top of the dike may form connected preferential flow paths within the dike due to concentrated leak erosion. Concentrated leak erosion is a form of internal erosion where concentrated leakage flows through soil defects such as cracks, roots, or burrows, initiating the detachment of soil particles (Benahmed & Bonelli, 2012). A study of the concentrated leak erosion behavior of cohesive soils found that the erosion rate of clay soils may be increased by a higher saturation level (Benahmed & Bonelli, 2012). Therefore consecutive rainfall events inciting flow through the clay fractures may promote concentrated leak erosion to provide the dike with more drainage. From this analysis, macro-stability is most affected during rainfall after sustained dry conditions. This could be due to cracks forming on the top of the dike without forming internal preferential flow paths, which provide drainage.

2.3.3 Water balance

The water balance was evaluated for the reference scenarios to understand the water fluxes within the dike and prevent any significant mass errors. This was done by comparing the change in total moisture content or water storage with the sum of all the fluxes at each timestep. The change in moisture content was evaluated by integrating the water content in both domains. The fluxes were defined as the sum of the integration of the boundary and exchange fluxes in both domains. The rainfall study was performed with a relative tolerance of 0.01, and 2001 timesteps were evaluated.

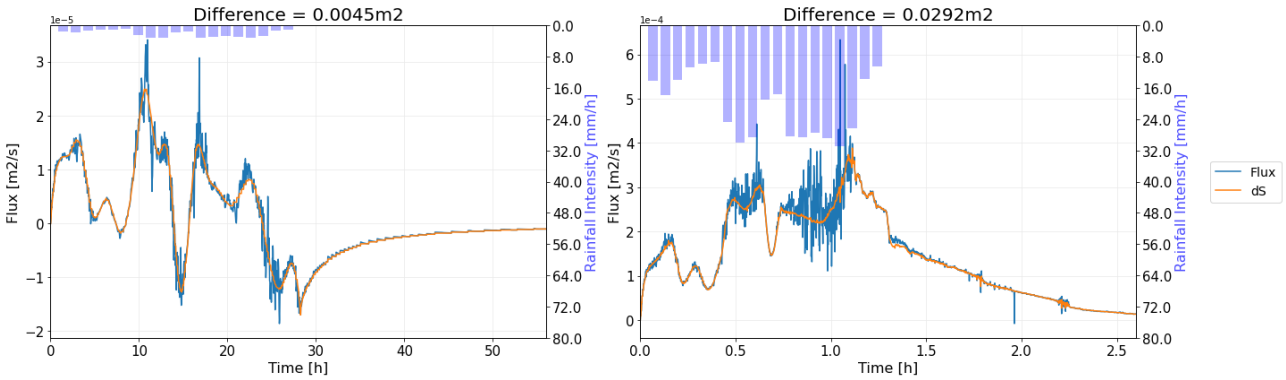

Figure 20: Change in storage (dS) or moisture content and fluxes over time for low and high intensity rainfall and their differences.

The observed fluxes correspond closely with the change in storage (dS). The spikes in the total amount of fluxes represent the head-driven exchange fluxes. At these times, the fracture domain observes a significantly larger gain or loss than the matrix domain due to the exchange term, normalized by volumetric ratios of each domain according to Equations 7 and 8. The differences between the change in storage and the fluxes amount to 0.0045m^2 and 0.0292m^2 for low and high-intensity rainfall, respectively. These differences result in a relative error compared to the change in storage of 2.9% and 1.3%. To investigate the influence of the spikes on the change in fluxes, a model run on the high rainfall intensity storm was performed with a refined tolerance of 0.0001. From this run, the difference between the change in storage and the fluxes was reduced from 0.0292m^2 to 0.0170m^2. However, the spikes in the fluxes persist, confirming they correspond to the exchange fluxes. While the reduced tolerance improves the discrepancy between the changes in storage and fluxes, the previously noted tolerance of 0.01 was used for the rest of the study to ensure a faster computational speed.

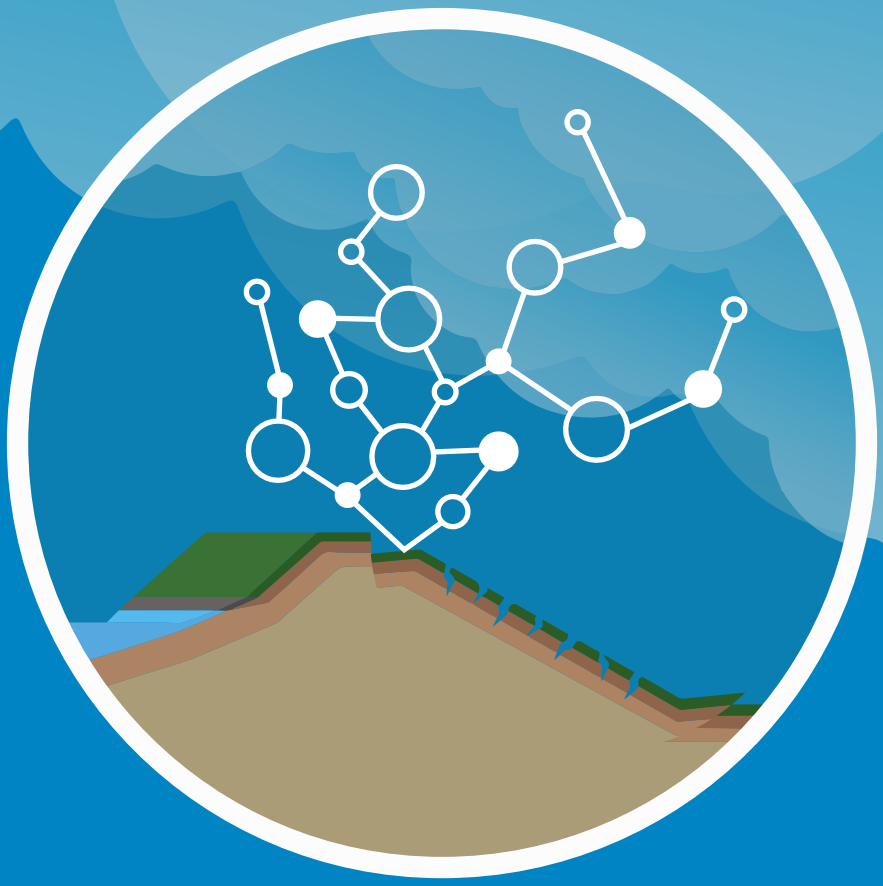

3. Surrogate Model

3 Surrogate model

This chapter proposes a surrogate model framework to emulate the response surface of the FEM with a smaller computational budget. This surrogate model was used to study the response surface of the FEM and perform a stochastic analysis of the study parameters on the failure probability.

Section 3.1 provides a brief introduction to surrogate modelling. Then, sections 3.2 & 3.3 discuss the point and parameter sampling strategies used by this study. Training data generation and augmentation are explained in section 3.5. Subsequently, the machine learning architecture is described in section 3.6 and evaluated with the FEM in section 3.7.

3.1 Introduction to surrogate modelling

Most fields of science and engineering require computer simulations such as a FEM to evaluate the influence of variables on a design objective or physical phenomena. These simulations can be computationally expensive, as was the case for the FEM presented in chapter 2. Thus, the computational budget restricts the number of evaluated simulations. Surrogate modelling is a commonly used approach to overcome this issue and aims to emulate the original model. This approach spends its available computational budget on generating representable training data to train the surrogate model. Then, once properly trained, the surrogate model can produce significantly more results than the FEM under the same computational budget (Sobester et al., 2008). The performance of the surrogate model depends on the choice of training data and the model itself. Therefore, a good parameter sampling strategy is required.

3.2 Point sampling strategy

Pore pressure changes affect the effective stresses within the dike and the resulting macro-stability. The FEM models changes in the pore pressure distribution under rainfall infiltration using Richards' equation. Points in the dike were sampled to capture these changes in the surrogate model. Then, based on the pressure head in these points, an image can be created per timestep using Kriging interpolation. A point sampling strategy was used to sample 40 points to maximize the efficiency of the surrogate model to reproduce this image. Point sampling consists of choosing the most important points based on the spatial trend.

A principal component analysis (PCA) was used to highlight the several correlated regions to sample points from. A brief introduction to PCA is given in Appendix B. This PCA was performed on pressure head data generated by the high rainfall intensity reference scenario (Table 4). The observational data set was generated by extracting the hydraulic head from 122 well-distributed points in the matrix domain at each time instance. The first two Principal Components (PCs) account for 92.6% of the variance in the data and make up the majority of the explained variance. Therefore the rest of the PCs were neglected. The coefficient matrix characterizes each PC, which is a linear combination of the input variables. Thus every point has a coefficient for every PC.

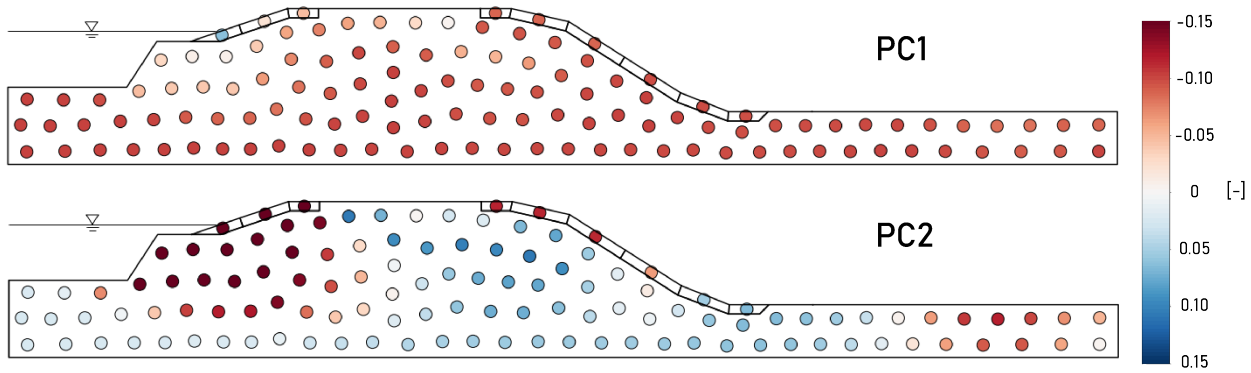

Figure 21: The coefficient matrix of PC1 and PC2 for the 122 plotted points. PCA study was conducted on a high intensity reference scenario simulation (Table 4).

Regions of strongly positive or negative coefficients are most important for the variation in data for each respective PC. As observed in the coefficients of PC1, regions lower in the cross-section, which remained saturated during

the entire simulation, have strongly negative coefficients. In contrast, several regions in the unsaturated zone have slightly negative to slightly positive coefficients. The coefficients of PC2 are strongly negative in the upstream region of the dike and the cracked top layers.

The coefficients of PC1 and PC2 highlight regions with large spatial variations. However, temporal variations in smaller local regions are also essential to describe the mass flux through the dike. This allows for the determination of the variance of each point (Figure 22).

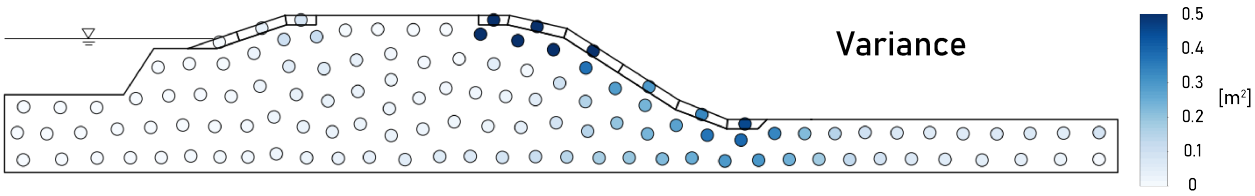

Figure 22: Variance at each point, based on a high intensity reference scenario simulation (Table 4).

Large temporal variations occur in the toe and the inner slope of the dike (Figure 22). This could indicate the wetting front, which develops after the infiltration capacity is exceeded. 40 points were sampled from four highlighted regions based on the spatial trends captured by the variance and PCA analyses (Figure 23).

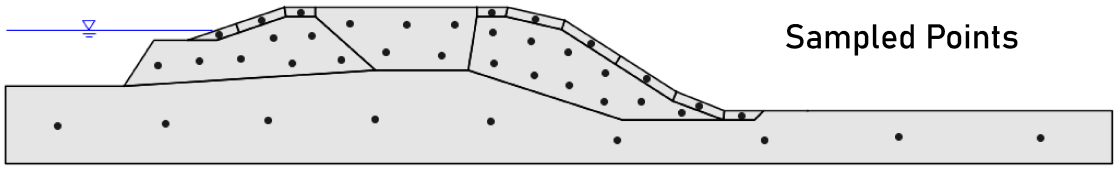

Figure 23: Final sampled points with the highlighted regions.

3.3 Parameter sampling strategy

The choice of the study parameter significantly influences the response of the FEM. The FEM has many different parameters that can be studied and varied in the surrogate model. These parameters include the soil, SWRC, swelling, rainfall, and crack parameters. The number of chosen parameters were reduced to the study parameters defined in Table 3. These parameters describe the variability of rainfall infiltration through soil cracks.

An efficient parameter sampling strategy is required as surrogate models have great difficulty with extrapolation but are generally good at interpolation (Sobester et al., 2008). This sampling strategy can be used to sample the simulation's input parameters. Each set of input parameters results in a single observation or model output and can be represented by a single input vector. Therefore, a point in the sampling space can represent this input vector. A sampling plan is a set of input vectors to train the surrogate model. The computational budget often limits the number of input vectors and the number of simulations. Therefore, the sampling plan must be space-filling (Sobester et al., 2008), which is when the input vectors are well distributed in the sampling space to provide enough coverage for interpolation between the observations. This helps the surrogate model train efficiently.

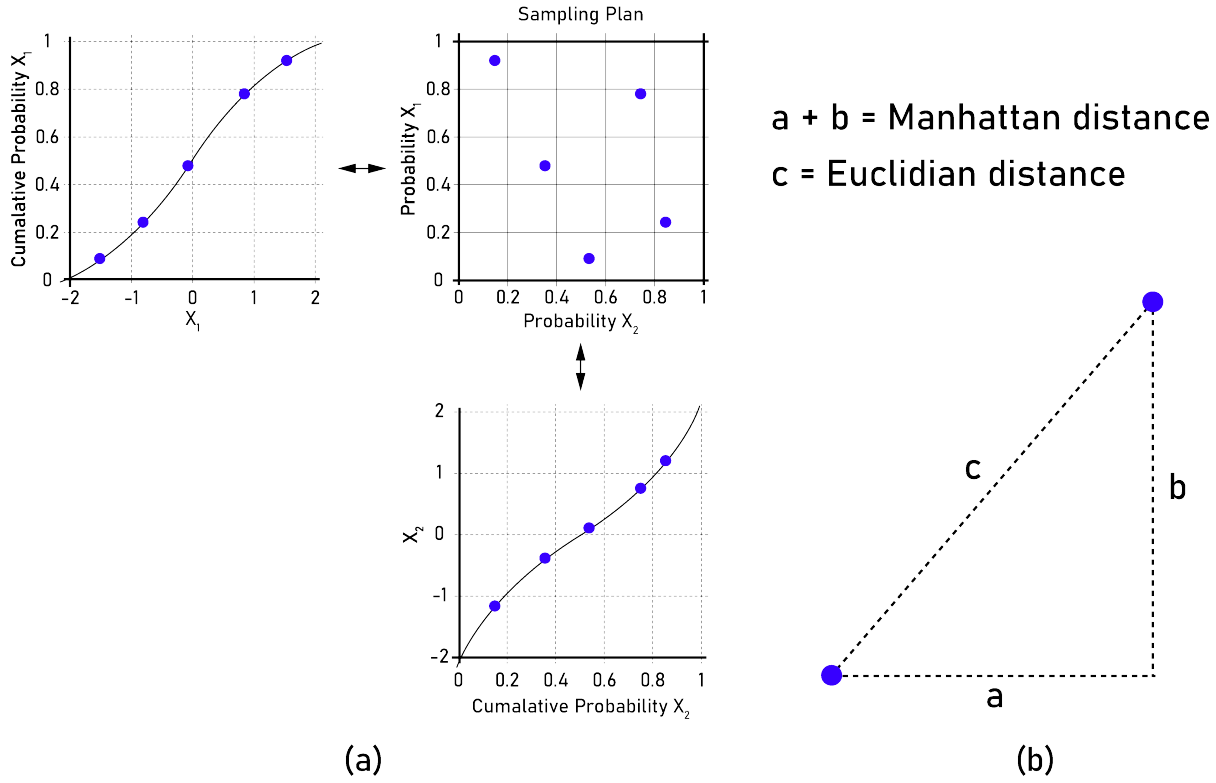

Figure 24: (a) Example of a LHS sampling plan for 2 variables with a normal distribution. (b) Euclidian and Manhattan distance.

This research used a Latin Hypercube Sampling (LHS) strategy. LHS ensures that samples only appear once for every row and column by stratifying the cumulative distributions of the input variables into intervals (Sobester et al., 2008). First, a sampling plan is created by providing the number of variables and the number of desired samples. The variables are projected in this generated sampling plan with uniform distributions in their discrete intervals. However, this does not necessarily yield a very space-filling sampling plan as each variable is randomly generated. Hence, an optimization method is required to optimize the space-filling capacity of the sampling plan (Figure 24). This can be done by computing the p-norm, the distance between the points in the sampling space (Viana, 2013).

$$d(x_1, x_2) = (\sum_{n=1}^{k} |x_1^i - x_2^i|^p)^{1/p} \tag{23}$$

The value of p determines the distance, where p=1 indicates the Manhattan distance and p=2 the Euclidian distance (Figure 24). The p-norm is effectively used in a maximin optimization scheme where the distance between the points is maximized while the number of pairs of points is minimized. In this study, the effect of four input parameters was studied and several LHS plans were generated with 10, 100, 200 and 1000 input parameter sets. The final space-filling sampling plan was generated using LHS which utilized a maximin optimization scheme with 1E5 iterations.

3.4 Parameter cumulative distributions

As mentioned, LHS was used to generate a space-filling sampling plan of the four input variables by producing numbers between 0 and 1 for each variable representing their probability of occurrence. These were fed into the unique cumulative distributions of each variable (Figure 24)

3.4.1 Parameter b

The geometric crack parameters vary mainly depending on the amount of water and clay content in the soil (J. H. Li et al., 2011). Several studies aimed to describe the distribution of geometric crack parameters for several different types of clay soils. J. Li & Zhang (2010) describe the REV of a crack network in silty clay soil (roughly 35% clay content) and found that the average crack aperture (b) was 0.49mm. Dyer et al. (2009) studied cracks in clay flood embankments in the UK and found that crack apertures varied between 5 to 25mm. Konrad & Ayad (1997)

found similar results and also studied the geometric properties of fractured clay soils. While not explicitly indicated, the studied soils in the latter two studies likely have greater clay contents than in J. Li & Zhang (2010). However, there is a common consensus among these papers that the magnitude variability in the crack aperture follows a lognormal distribution (J. Li & Zhang, 2010; McKay et al., 1993; Konrad & Ayad, 1997).

In this study, the crack aperture varies during a simulation based on the water content and the maximum crack width (b). Thus, the variability of the aperture for every cracked subdomain is a function of the water content. However, for simplicity, a lognormal distribution that encompasses the range of absolute crack apertures was adopted for this maximum crack aperture (b). The chosen lognormal distribution has a mean of 0.003149 and a standard deviation of 0.5973. The aperture in this distribution is indicated in meters.

3.4.2 Parameter wPf

J. Li & Zhang (2010) found lognormal distributions in both the crack aperture (b) and crack spacing (a). Since these variables were used to calculate the volumetric ratio of the crack domain according to Equation 2, it was assumed they adopt the same type of distribution. Furthermore, the crack porosity also depends on the water and clay content, so the literature varied again. J. Li & Zhang (2010) described a feasible average value for the REV of clays as 0.02. Huang et al. (2019) found that the crack ratio in high clay content soils (roughly 50%) can increase over several dry-wetting cycles ranging from 2% to 12%. A lognormal distribution was chosen to encompass this wide range and has a mean of 0.06 and a standard deviation of 0.4.

3.4.3 Parameter R

The average rainfall intensity (R) distribution depends on the local climatic conditions. Hourly data of a nearby KNMI station (station Berkhout) (KNMI, n.d.) was used to estimate a suitable distribution for the average rainfall intensity. The KNMI station in Berkhout is less than 10km away from the modelled dike and has hourly rainfall data records from 1990. The average hourly rainfall intensity was derived from the observed precipitation amount divided by the recorded hourly rainfall duration. A probability density function (PDF) of the monthly maximum recorded rainfall intensity was made, yielding a distinct bimodal distribution with a small peak at 5mm/h and a large peak at 10mm/h. A Frechet distribution was chosen to encompass both peaks with shape, scale, and location parameters equal to 2.1279, 8.6604, and -0.02, respectively.

3.4.4 Parameter Tr

The return period distribution was determined by applying generalized extreme value theory on daily rainfall measurements from the KNMI station West Beemster (KNMI, n.d.), which lies around 8km from the modelled dike. This KNMI station has daily precipitation observations from the year 1951. The maximum annually recorded rainfall amounts were translated to return periods. The PDF of these return periods were captured by a Pareto distribution of shape, scale, and location parameters equivalent to 4.40116, 13.40, and -13.40, respectively.

3.4.5 Final distributions and LHS

The resulting probability density function and cumulative density function (CDF) of the study parameters are shown in Figure 25. The sampling plan from the LHS was fed into the CDF distribution for each variable to obtain the final parameter sets.

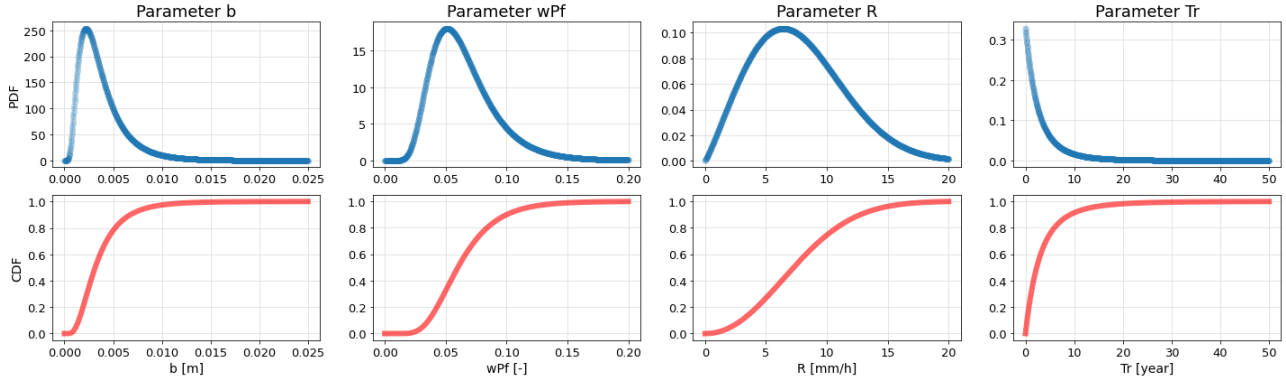

Figure 25: The PDF and CDF of sample parameters.

Since the LHS plan maximizes the distances between the parameter sets, adding more samples is impossible after the LHS plan is generated. To illustrate how the number of parameter sets influences the results of the surrogate model, LHS plans of sample size 10, 100, and 200 were generated in addition to the LHS plan with 1000 samples.

3.5 Training data generation & augmentation

The FEM DPM crack model can take up to two hours to generate a single training data set. Thus, the computational budget severely limited the training data generation. Machine learning architectures are notoriously data-hungry; therefore, the training data was augmented. A batch script was made in MATLAB to generate the training data to run the COMSOL FEM with the LHS sampling plans of the input study parameters. These outputs to the FEM were the timeseries of the hyetograph, the pressure head in the sampled points, and the factor of safety for a duration of twice the length of the storm. These timeseries have 2000 timesteps with variable timesteps depending on the combination of input parameters (R and Tr). These timeseries were augmented by a sliding window consisting of a window size of 500 and 1000 timesteps and a stride of 100 timesteps. However, the size of the sliding window reduced the timeseries that the surrogate model could reproduce to the largest sliding window size. Since the largest sliding window size was equivalent to the storm's duration, the surrogate model sequence length was limited to this timespan.

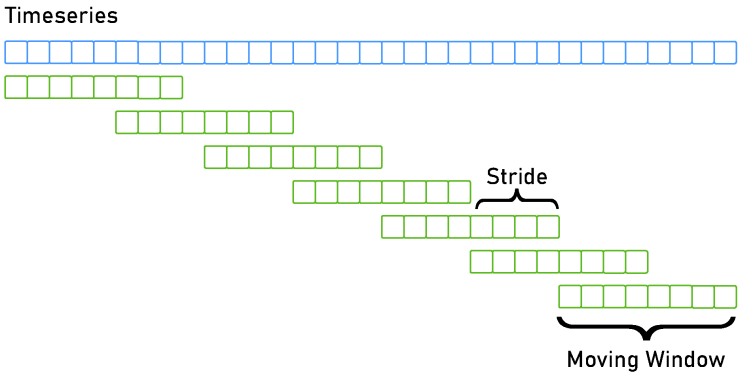

Figure 26: Data augmentation of the timeseries. The stride indicates how much the moving window slides over the timeseries. The size of the moving window controls the modelled sequence length.

In timesteps, when the dike fails (FOS < 1, see section 2.1.1.6), the FEM produced empty timesteps for the FOS. Since this only happens after the storm has ended, the timeseries of the pressure heads, the hyetograph, and the factor of safety were reduced to only include the extent of the storm. This was done to avoid any unreliable FOS timeseries. In addition, data augmentation of the timeseries resulted in a larger training data set for each of the LHS sampling plans, as observed in Table 7.

Table 7: Increase in training data due to augmentation.

# LHS Parameter Sets	Augmented Dataset
10	206
100	1958
200	4358
1000	21875

After experimenting with variable sequence lengths, a length of 21 timesteps was chosen to match the 20 random bins chosen in chapter 2.1.1.5. As expected, the performance of the surrogate model also decreased with longer sequence lengths. To match the sequence length, 21 timesteps were sampled from the augmented datasets of window sizes 500 and 1000 timesteps. These timesteps were sampled at regular intervals and matched the peaks and troughs in the hyetograph.

3.6 Model architecture

In this study, the static inputs to the surrogate model consisted of the study parameters and the initial pressure heads in the sampled points at the start of the simulation. By including the initial pressure heads as input in the surrogate model, the timeseries in each training data set could be augmented to produce more training data (see

section 3.5. Furthermore, the dynamic input was the hyetograph timeseries which allowed for the investigation of several design storms. The surrogate model produced a timeseries of the FOS and the pressure head in the sampled points as a function of the static and dynamic inputs. Before training the model, the training data was normalized for each LHS plan.

A flexible machine learning architecture was chosen to process dynamic input features, such as the hyetograph timeseries, and static input features, like the study parameters and the initial pressure heads. As observed in chapter 2, the influence of rainfall infiltration on the macro-stability depends on the memory of the moisture content. Therefore, a long short term memory (LSTM) model was chosen to mimic and reproduce the memory of the hydrology within the dike. LSTM networks are a type of recurrent neural network (RNN) capable of learning order dependence. An LSTM uses memory states with several gates to control information flow, making them efficient in sequence problems (Miebs et al., 2020). In a study by Miebs et al. (2020), three possible architectures were proposed to process both dynamic and static input features in an RNN. The first architecture included an LSTM to process dynamic features, which was subsequently concatenated with a dense layer that processed the static features. The second fed the dense layer of the forward neural network (FNN) directly into the hidden and state cells of the LSTM. Finally, the third included a combination of the former mentioned in which static features were fed into the hidden and cell states of the LSTM and concatenated with the outputs of the LSTM. All three architectures were replicated, and while the third and second architectures have similar performance, the second architecture was chosen for its lower number of trainable parameters.

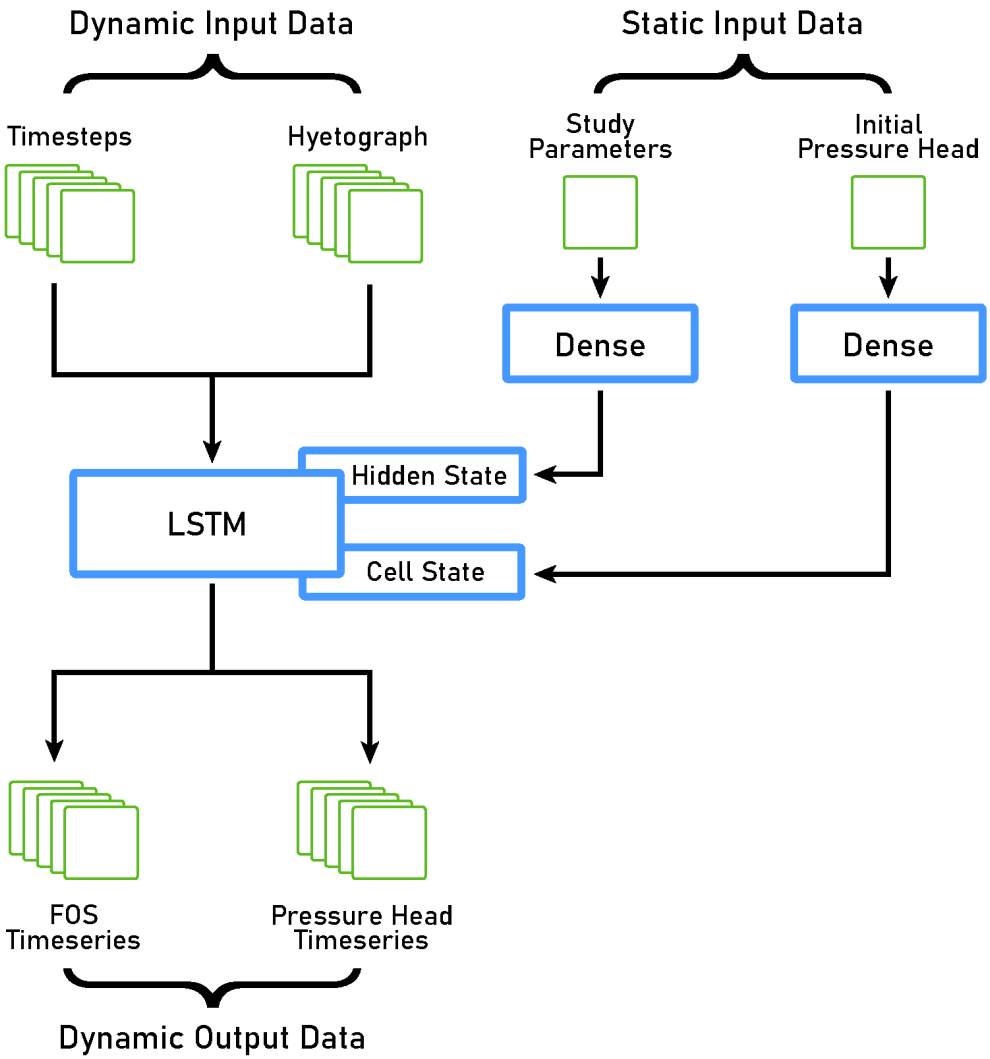

Figure 27: The final surrogate model architecture. The surrogate model consists of a FNN-LSTM model architecture which takes both dynamic and static input features.

The amount of available training data restricted the number of trainable parameters. For this reason, it was decided

to only include a single dense layer for each static input feature. The number of neurons in these dense layers was also restricted because the LSTM requires its hidden and cell states to have the same number of neurons as the LSTM.

In efforts to reduce overfitting the model, several hyperparameters were fine-tuned. These hyperparameters are summarized in Table 8. Additionally, the learning rate was reduced by 75% upon reaching a plateau in the validation loss.

Table 8: Hyperparameters used in training the surrogate model. The surrogate model architecture was built in Tensorflow Keras. This python package includes the hyperparameters (Abadi et al., 2015).

Parameter	Value
Batch size	32
Initial learning rate	0.001
Optimizer	Adam
Loss	MSE
Metric	RMSE
Epochs	2000

As a result of the data augmentation, the model can only predict the storm's duration. However, as seen in chapter 2, the largest decline in the FOS occurs after the storm. The surrogate model was propagated twice to assess the FOS after the storm. Hence the outputs from the first surrogate model simulation were used as inputs to the second surrogate model simulation. A slight overlap of three timesteps gave the best performance, and the model could recognize the end of the storm. However, this reduced the final combined sequence length from 42 to 39 timesteps. In terms of the storm length duration, this meant that the final modelled duration was slightly less than twice the storm length duration. However, in most cases, the largest decline in FOS already occurred within that timeframe.

3.7 Model evaluation

The final surrogate model architecture was evaluated for models with 48, 64, and 80 neurons. First, the validation RMSE was plotted against the size of the training data set (by several LHS parameter sets) for surrogate models with 48, 64, and 80 neurons. Note that the LHS plan of 200 parameter sets slightly differed in FEM settings and thus performed slightly differently from the other training data, as seen in Figure 28.

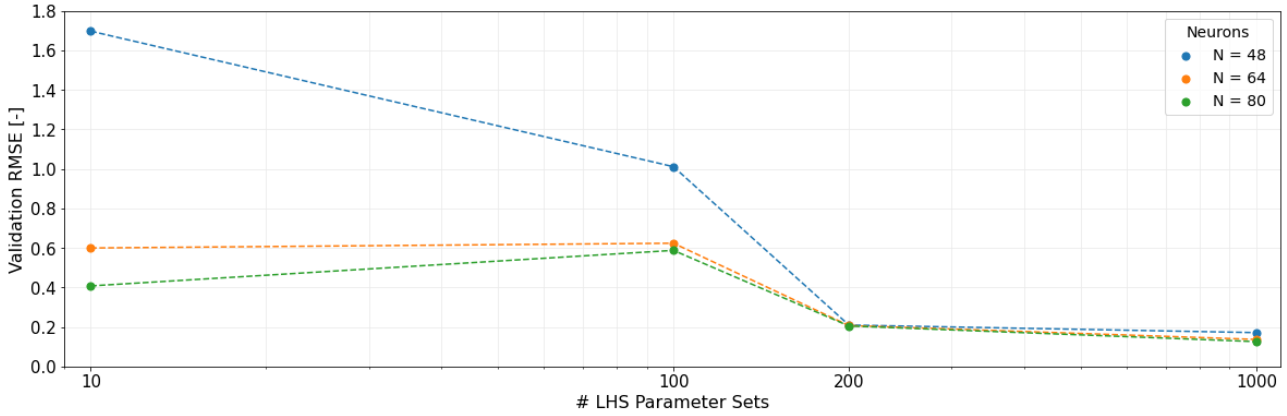

Figure 28: Validation RMSE (on normalized data) for each LHS plan.

The model with 80 neurons performs the best for all LHS plans. Figure 28 also demonstrates the efficiency of Latin hypercubes as performance only slightly improves between the 200 and 1000 LHS plans.

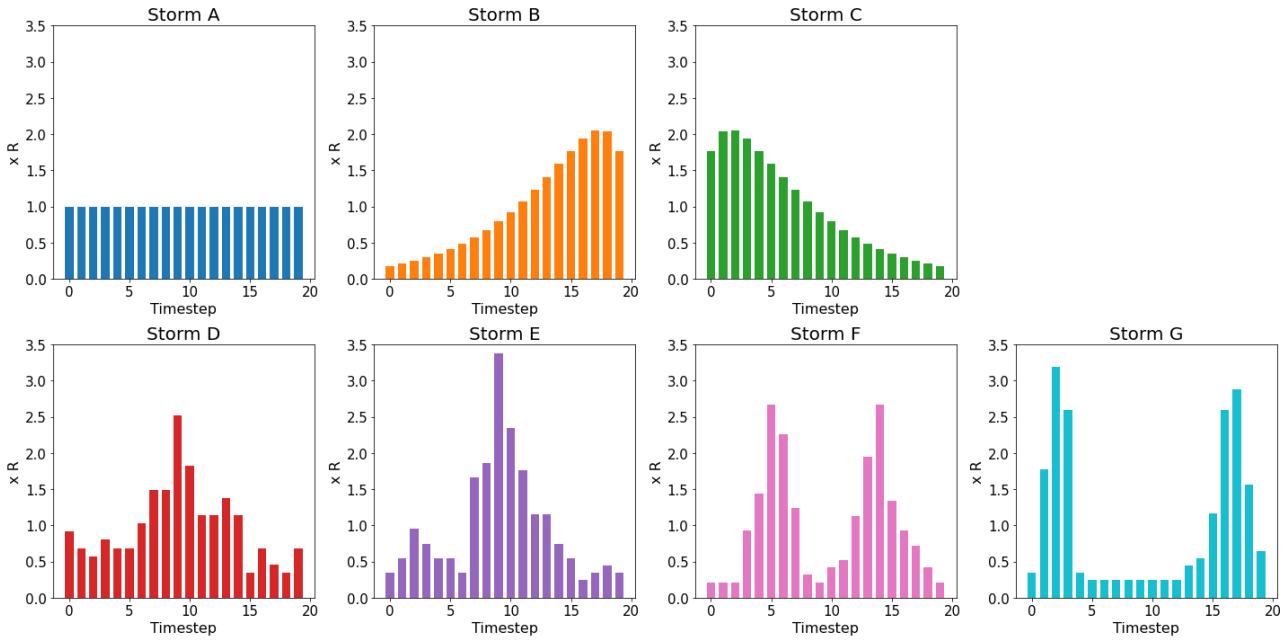

Figure 29: Reference rainfall patterns. The magnitude is multiplied by the average rainfall intensity (R). Storm shapes D-G are derived from Smits et al. (2004).

To assess the generalization capacity of the three possible models (with 48, 64, and 80 neurons), several rainfall patterns were modelled and compared with the results from the FEM. Smits et al. (2004) analyzed several precipitation patterns for the Netherlands and defined several common storm shapes. These storm shapes include univariate storms with a single variable peak and variable dual peak storms with a short and long time between peaks. Four of these storms were chosen to evaluate the choice of model. Three synthetic storms were fabricated as a reference, including a storm with a constant rainfall intensity, a storm that increases in rainfall intensity in time, and a storm that decreases in rainfall intensity in time. The latter two were defined by a gamma distribution with alpha and beta parameters equivalent to 1.5 and 5. A summary of the reference storm shapes can be found in Figure 29. In reference storms D to G, the magnitude of the resulting hyetograph exceeded 2 in the peaks. Since the training data only included storms with a maximum rainfall intensity equivalent to twice the average rainfall intensity, the surrogate model was evaluated for its capacity to extrapolate in these storms. The surrogate model combinations (48, 64, or 80 neurons) were tested for the reference storms under a high-intensity storm (Table 4). The state of the FEM after the warming-up period was the initial state of the surrogate model.

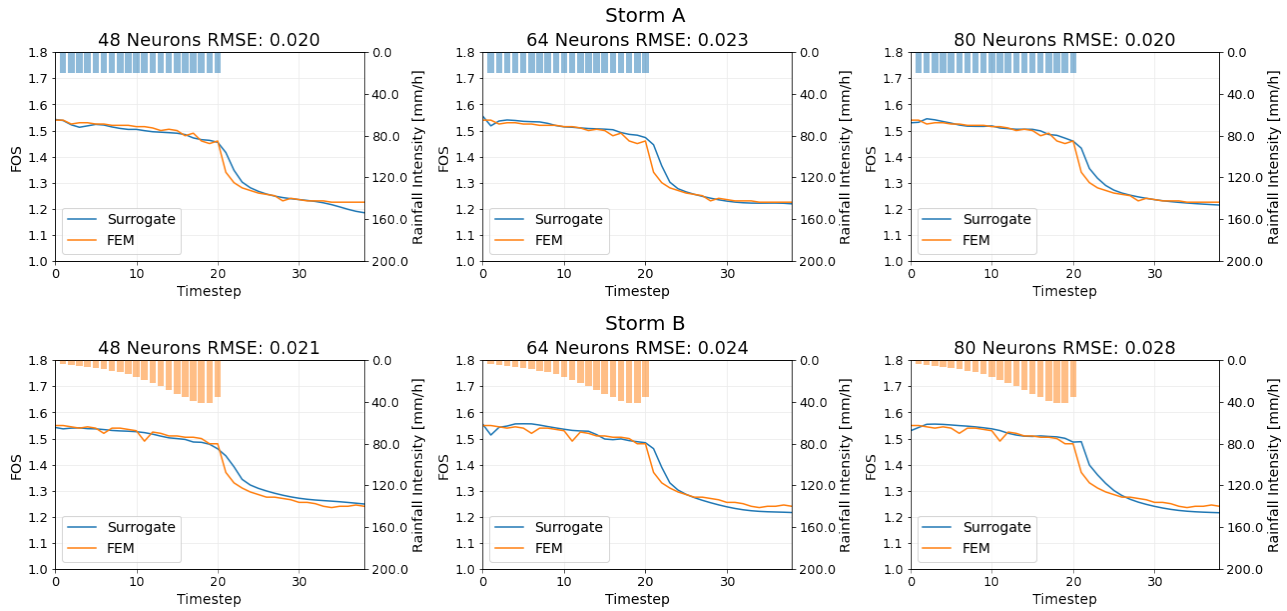

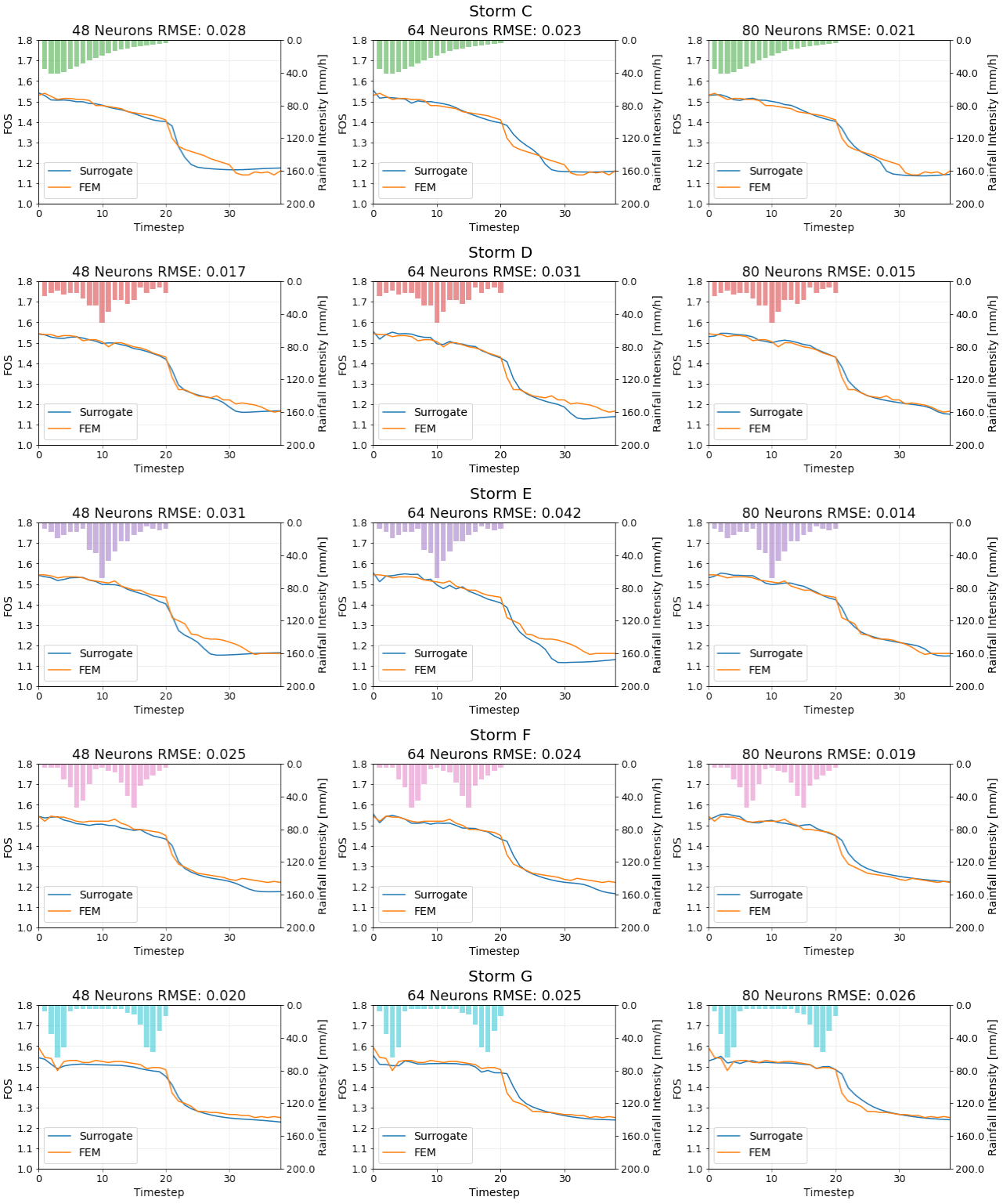

Figure 30: Storm A-G evaluated for surrogate models with 48, 64 and 80 neurons with the FEM FOS timeseries.

As observed in Figure 30, the surrogate model effectively captures the effect of the reference storm on the resulting FOS timeseries most of the time. In storms D-G, the larger magnitude of the peaks did not lead to a significant decline in performance compared to storms A-C. Hence the model can extrapolate the influence of larger rainfall intensities than it was trained on. Even the surrogate model with only 48 neurons can reproduce the FOS timeseries during the storm. However, both surrogate models with only 48 and 64 neurons show a decrease in performance after the storm has passed. Thus, out of the three combinations, a model with 80 neurons shows the best performance as it can capture the decline in FOS after the storm. Therefore, 80 neurons are used in the final surrogate model. However, this means that the surrogate model architecture includes 33,561 trainable parameters, significantly more than the training data set after augmentation for the largest LHS plan (Table 7). To bridge this

large difference, the final model was trained on the stacked LHS, which increased the total training data to 28,397.

Since in the final model, the surrogate model, was consecutively run, where the output of one surrogate model became the input of the next, the error of the output features was amplified. The initial pressure heads became the first state of the cell state. Any error in this initial estimate of the pressure head at the end of the first simulation was amplified by the second simulation. This offers a possible explanation as to why the models in Figure 30 have trouble reproducing the FOS timeseries right after the storm's end.

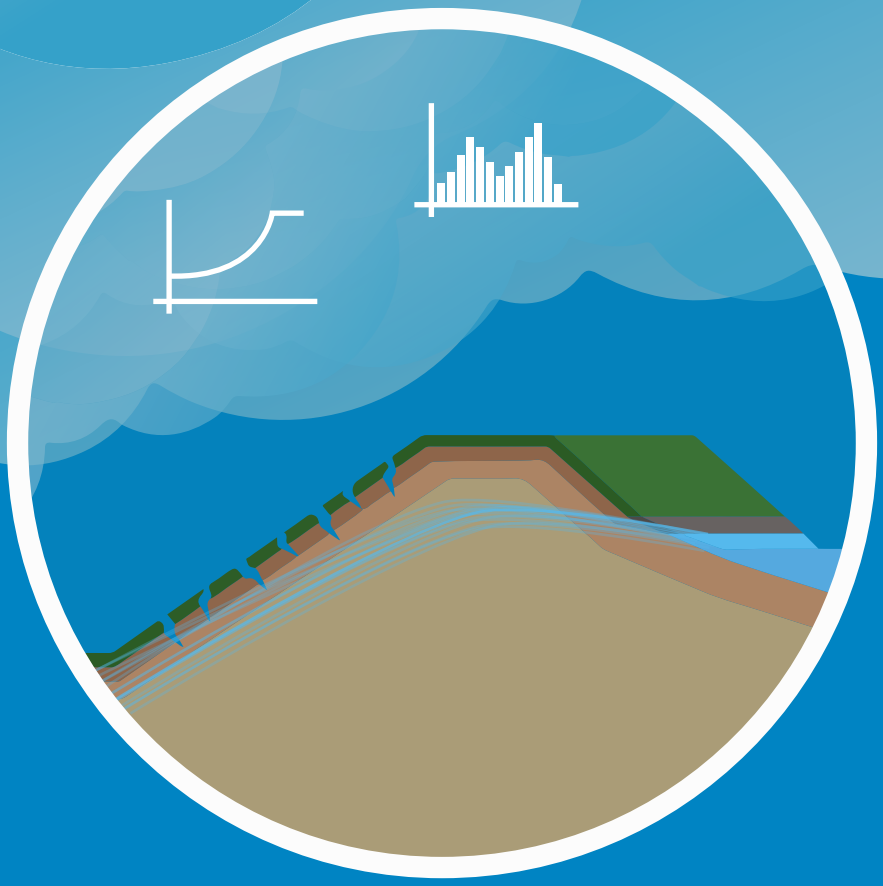

4. Sensitivity & Safety Assessment

4 Sensitivity & Safety Assessment

The surrogate model aimed to reproduce the underlying response surface of the FEM to study the influence of the study parameters on the macro-stability and the phreatic surface. As mentioned in section 2.1.2, the study parameters were the maximum crack aperture (b), the volumetric ratio of the cracks (wPf), the average rainfall intensity (R), and the associated return period (Tr) of the storm. Although the crack parameters varied during the simulation due to swelling, the effect of the input crack parameters (b and wPf) is considered in this chapter. While building the surrogate model, a fifth and final study parameter was added. This study parameter was the rainfall pattern (rainfall intensity over time), which was randomized in the training data.

A global and local sensitivity analysis is conducted in section 4.1. Subsequently, the shape of the phreatic line for the lowest FOS in each timeseries is evaluated in section 4.2. Lastly, in section 4.3, the reliability index (beta index) is determined for each storm shape and compared with Dutch legislation.

4.1 Sensitivity analysis

Sensitivity analysis studies how various sources of uncertainty in the input can contribute to the variation in the output of a model. It is often used to quantify uncertainties associated with the model input parameters (Saltelli et al., 2004). A global and local sensitivity analysis was conducted to examine the response of the study input parameters on the minimum FOS. A variance-based global sensitivity analysis was used to describe the entire response surface of the input parameters and to identify the uncertain input parameters. Unfortunately, this method does not include specific values of the model output (Jaxa-Rozen et al., 2021). Since the minimum FOS is of value as it describes the largest decline in macro-stability, a local sensitivity analysis was also performed. In the local sensitivity analysis, where a limited response surface is studied, a one-at-the-time (OAT) method was used. This method allows for studying the effect of varying one parameter on the FOS timeseries and the minimum FOS of each timeseries.

4.1.1 Global sensitivity analysis

To conduct the global sensitivity analysis, the Sobol sensitivity indices were calculated using Monte Carlo estimators. Sobol sensitivity is a variance-based sensitivity analysis where the indices decompose the variance of the output by the contribution of each input parameter and their combined influence (Sobol', 1990). The first-order Sobol sensitivity index measures the main effect of an individual input parameter on the variance of the output. The second-order sensitivity index measures the interaction effect of two input parameters on the variance of the output. While higher-order sensitivity indices exist, they are conventionally disregarded as their contribution is often relatively small (Azzini et al., 2021). Finally, the total sensitivity index is the sum of all the sensitivity indices (Sobol', 1990). Due to the decomposition of variance, the Sobol indices are not additive. The first and total Sobol indices (S_u and ST_u) are defined by Equations 24 and 25.

$$S_u = \frac{\mathbb{V}[\mathbb{E}[y|u]]}{\mathbb{V}[y]} \tag{24}$$

$$ST_u = \frac{\mathbb{E}[\mathbb{V}[y|u]]}{\mathbb{V}[y]} \tag{25}$$

Where ($\mathbb{V}$) and ($\mathbb{E}$) are the unconditional variance and the conditional operators. Sobol' (1990) proposed Monte Carlo estimators to determine these indices. To generate multiple input sequences, these estimators require sampling the input parameters according to a low-discrepancy sequence such as a Latin hypercube. Azzini et al. (2021) proposed an updated strategy to determine the Sobol indices using Monte Carlo estimators. According to the law of total variance, the proposed Monte Carlo estimators ensure that the total Sobol index is always greater than the first Sobol index. These Monte Carlo estimators are only applied on the first and total Sobol indices (Azzini et al., 2021). However, the combined higher-order Sobol indices can be inferred by comparing the first and total Sobol indices. In the sampling method, two Latin hypercubes are generated and subsequently augmented by replacing each column in the first Latin hypercube with the same column in the second Latin hypercube and vice versa. After doing this for each parameter column, a total of 10 Latin hypercubes are constructed, each consisting of 4 parameter columns with 10,000 parameter sets. Hence, let (y^A, y^B, y^{Au}, y^{Bu}) be different model output samples, where (u) refers to each parameter column augmented by either Latin hypercube A or B. These

outputs for each n-th element can be defined as follows:

$$y_n^A = f(u_n^A, v_n^A) = f(x_n^A) \tag{26}$$
$$y_n^B = f(u_n^B, v_n^B) = f(x_n^B) \tag{27}$$
$$y_n^{Au} = f(u_n^A, v_n^B) = f(x_n^{Au}) \tag{28}$$
$$y_n^{Bu} = f(u_n^B, v_n^A) = f(x_n^{Bu}) \tag{29}$$

In this study, the Sobol indices were determined according to the following estimators in Equations 30 and 31.

$$\widehat{S}_u = \frac{2\sum_{n=1}^{N}(y_n^{Au} - y_n^B)(y_n^A - y_n^{Bu})}{\sum_{n=1}^{N}((y_n^A - y_n^B)^2 + (y_n^{Au} - y_n^{Bu})^2)} \tag{30}$$

$$\widehat{ST}_u = \frac{\sum_{n=1}^{N}((y_n^B - y_n^{Au})^2 + (y_n^A - y_n^{Bu})^2)}{\sum_{n=1}^{N}((y_n^A - y_n^B)^2 + (y_n^{Au} - y_n^{Bu})^2)} \tag{31}$$

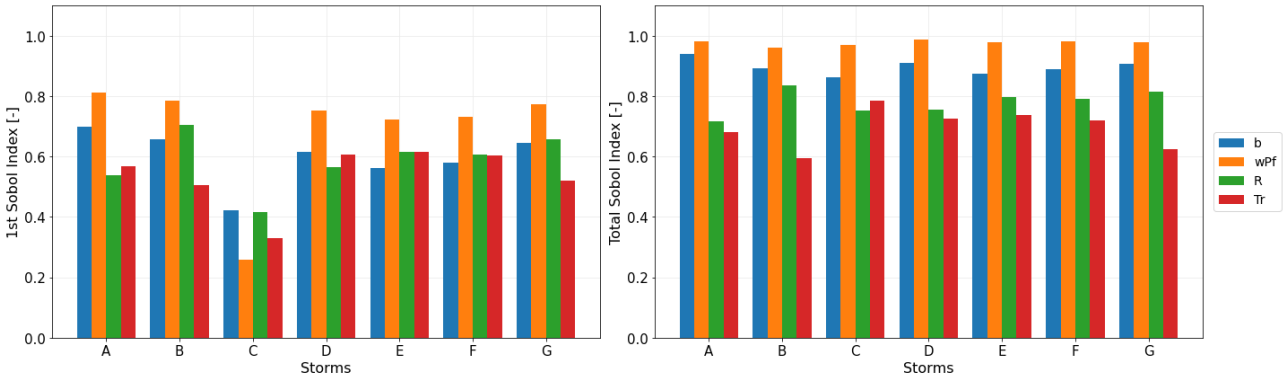

Figure 31: 1st and total Sobol indices for storms A-G. The first and total Sobol indices describe the main and total contribution of an individual parameter on the output variance.

The contribution of the first-order Sobol index is the majority of the total Sobol index for each parameter. This is the case except for the receding storm, C, where the first-order contributions are smaller than the other storms. Therefore, the second-order contributions (the combined parameter influence) is much higher for this storm than the other tested storms. The higher order contributions (difference between total and 1st Sobol indices) demonstrate the study parameters' interdependence on the output variation. Parameter wPf has the highest total Sobol index, which signifies that it yields the greatest variation in the output. Since the Sobol indices only describe the spread of the output as a result of each variable, the highest total Sobol index does not mean it results in the lowest FOS. However, the probability of a lower FOS is increased as the distribution in the lower tail increases in density with a greater spread. Parameter b has the second highest contribution after parameter wPf, meaning that the crack parameters profoundly impact the FOS timeseries. Although the contribution of the rainfall parameters is lower than those of the crack parameters, their total Sobol indices indicate that they are still responsible for a significant contribution to the overall variance.

4.1.2 Local sensitivity analysis

After determining which parameters result in the greatest influence on the variance of the output, a local sensitivity analysis was conducted to indicate which parameters are responsible for the lowest FOS. In contrast to a global sensitivity analysis, a local sensitivity refers to the sensitivity of parameters with respect to a fixed parameter set. In the OAT method, one parameter is varied while the others remain fixed (Morio, 2011). A reference parameter set was adopted, which consists of the mean of each study parameter given by the input distributions as indicated by Figure 25. For parameters b, wPf, R, and Tr, the adopted mean was equivalent to 3.15mm, 6%, 6.89mm/h, and 1year, respectively. Note that the mean of the Pareto distribution describing the return period is approaching zero, but for model purposes, a return period of 1 year was adopted. In the local sensitivity analysis, each parameter was varied one at a time, while the other parameters were held constant to their mean. The local sensitivity analysis quantified the influence of the variation of each parameter on the FOS timeseries and minimum FOS for each rainfall pattern. Since storm B results in the lowest FOS using the mean parameter set, this storm was used as an example for this local sensitivity analysis (the other storms are included in Appendix C).

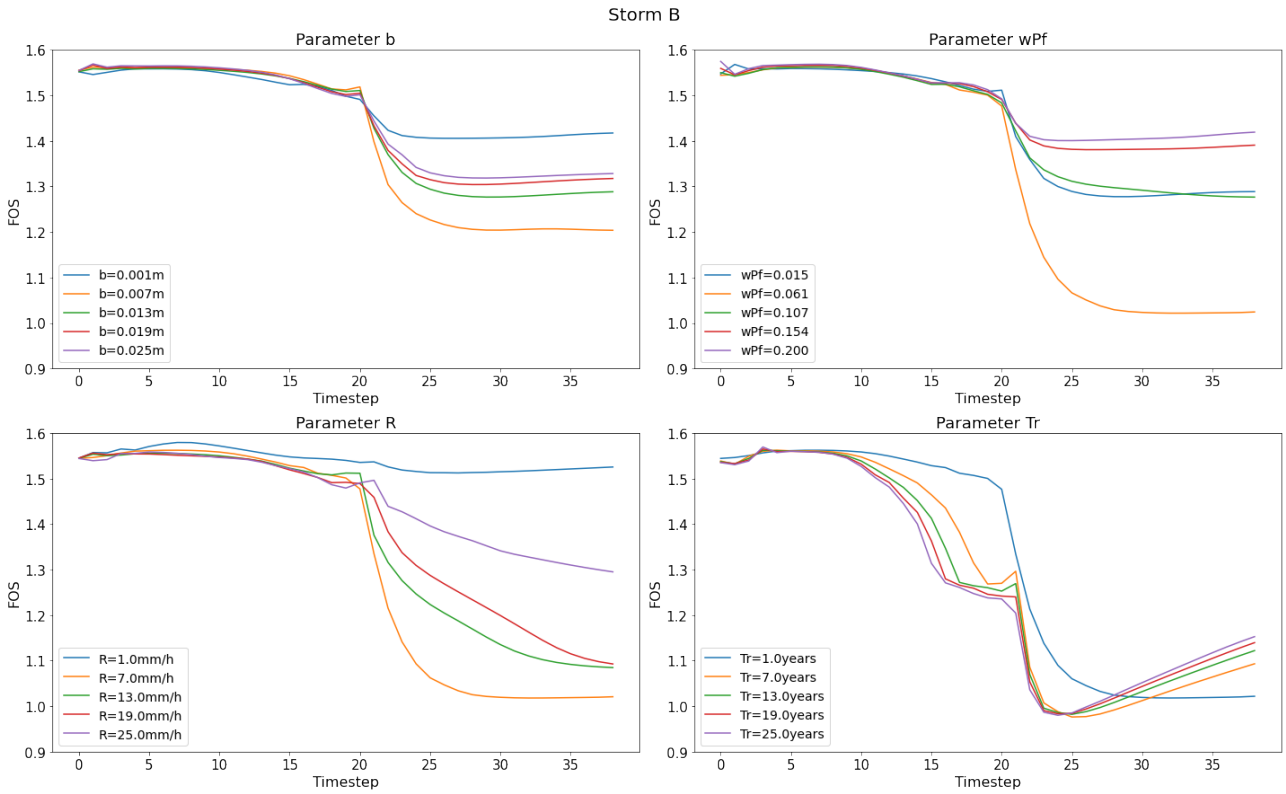

Figure 32: OAT analysis of the study parameters on the FOS timeseries of storm B.

The crack parameters (b and wPf) affect the minimum FOS reached after the storm. The average rainfall intensity (R) controls the hydrological forcing and mainly affects the rate at which the FOS decreases after the storm. The return period (Tr) affects the FOS during and after the storm. For high return periods (Tr $\geq$ 1 year), a minimum FOS is reached during the storm but this minimum is higher than the minimum reached after the storm. This minimum FOS during the storm could suggest that the dike has reached maximum drainage.

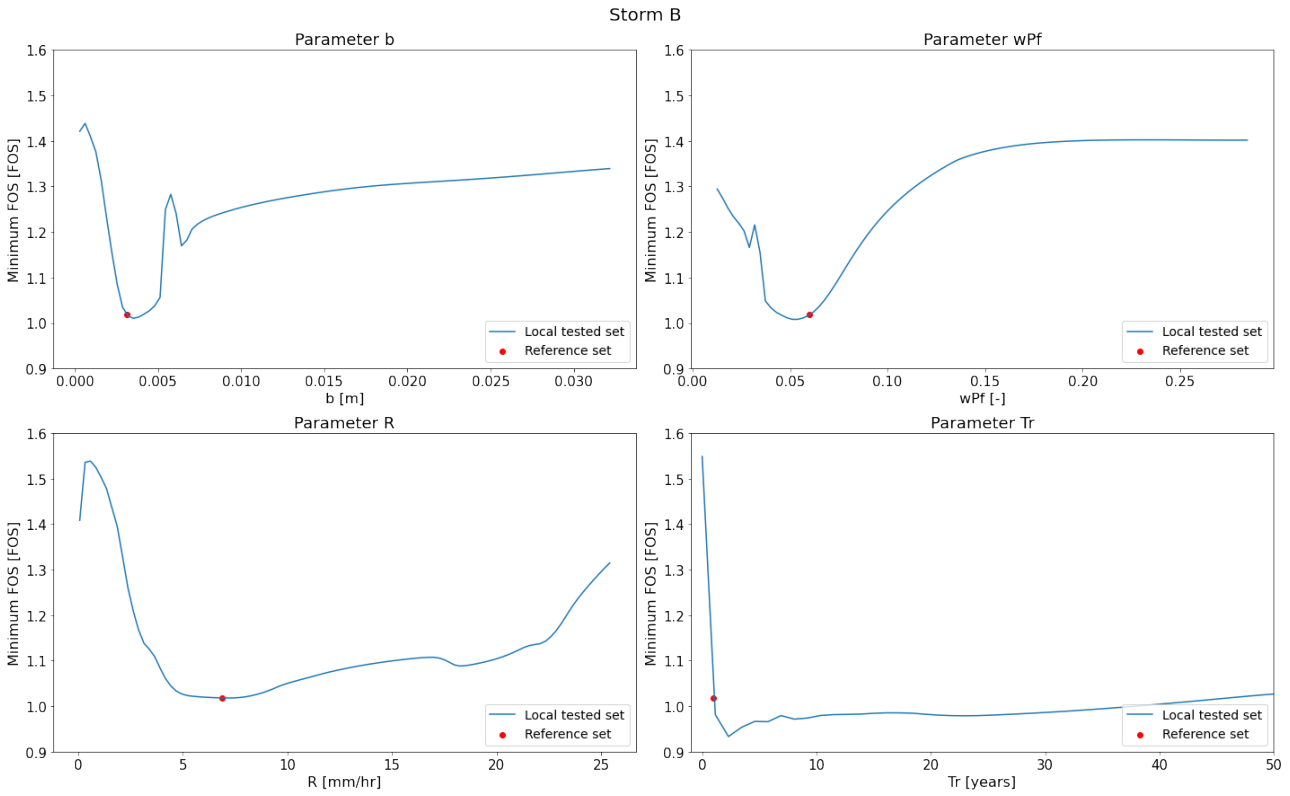

Figure 33: OAT analysis of the study parameters on the minimum FOS of storm B. The minimum FOS of the reference parameter set (b=3.15mm, wPf=6%, R=6.89mm/h, Tr=1year) was plotted in red.

When the crack parameters fall below a threshold, the cracks facilitate more water infiltration than drainage, resulting in a lower dike stability. Above this threshold, the cracks provide more drainage resulting in a higher observed minimum safety factor. Given the reference parameter set, this threshold for For the maximum crack width (b) is roughly 6mm, and for the volumetric crack ratio (wPf) at roughly 15%. In Figure 33, this threshold is found when the minimum FOS is maintained or slightly increases for larger crack parameters. At a wide crack aperture (b), the cracks have a higher saturated hydraulic conductivity enhancing flow to facilitate water drainage out of the dike. Similarly, an increase in the volumetric crack ratio (wPf) results in a faster and larger exchange from the matrix to the fractures, which provides drainage. The rainfall parameters (R and Tr) indicate the hydrological forcing. An increase in rainfall parameters decreases the minimum observed FOS up to a certain point. The average rainfall intensity (R) shows an increasing trend after a rainfall intensity of 6mm/h, and the return period (Tr) increases after two years. At a higher rainfall intensity, the amount of infiltration is limited by the infiltration capacity. Additionally, the storm duration decreases with an increase in rainfall intensity according to the IDF relation (Equation 20). Furthermore, by studying the influence of the high return period in the FEM, it was found that the dike is fully saturated after a return period of 2 years. At high return periods, the timesteps become larger. Therefore the minimum FOS cannot be captured by the timesteps taken, resulting in an increasing trend after a return period of 2 years.

The OAT analysis found in Figures 32 and 33 illustrates the local response of the study parameters on the FOS timeseries. This analysis depends on the reference parameter set and the rainfall pattern. By comparing the OAT analysis of the tested rainfall patterns (Appendix C), it was found that similar parameter trends occur in every storm. These trends include the threshold behavior of the crack parameters (b and wPf) controlling infiltration and drainage and the sharp decline in the minimum FOS for low rainfall parameters (R and Tr). However, the local response surface shifts with a change in the reference parameter set and rainfall pattern. Therefore, the rainfall and crack parameters have an interdependent influence on the dike stability.

4.2 Phreatic surface analysis

To investigate the influence of the phreatic surface on the minimum FOS, the phreatic surface was interpolated for 10,000 surrogate simulations for storm B at the timestep of the lowest FOS. In addition, 95% confidence intervals were calculated for several FOS ranges.

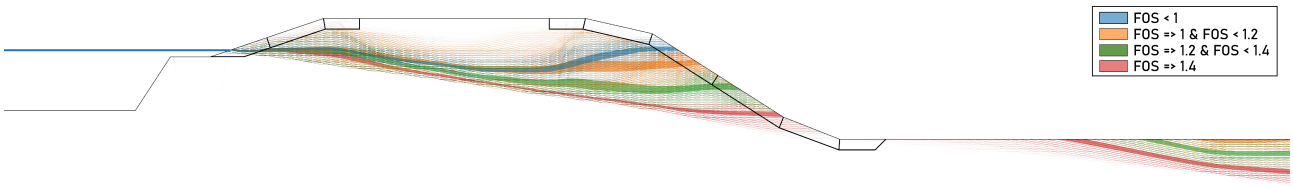

Figure 34: Phreatic surfaces from 10,000 runs for different FOS ranges. The full colors are the 95% confidence intervals.

The phreatic surface rises in the toe of the dike for a decrease in FOS. The influence of the no-flow boundary at the road results in a lower phreatic surface beneath the road and larger differences in the phreatic surface in the toe of the dike. The phreatic surface is assumed to be convex shaped in a conventional dike stability assessment (Lendering, 2016). However, according to this analysis, this assumption is too simplistic as the phreatic surface is influenced by the rainfall, the road, and the shape of the dike. In fact, for the lowest FOS, the phreatic surface curves upward and for a higher FOS, the phreatic surface appears straight.

4.3 Reliability index analysis

The reliability of a dike is often quantified by its probability of failure, p_f, for its failure modes (Lanzafame & Sitar, 2019). According to Dutch legislation, the maximum total failure probability integrates the failure probabilities of different failure mechanisms that could occur (Overleg, 1999). The failure mechanisms that contribute the most to the failure probability of regional dikes are mainly focused on wave overtopping and macro instability of the inner slope, which are attributed 10% and 80% of the failure probability (Overleg, 1999). The modelled dike near Ursem has an associated return period of 1/100 years (HHNK, 2022). In line with Overleg (1999), the dike's estimated failure probability of the dike is 20% of the return period, and thus the modelled dike has a failure probability of 1/500. Since 80% is attributed to the macro-stability of the inner slope, the associated failure probability for this failure mode is 1/625.

The failure probability, (p_f), defined by the surrogate model, can be quantified by the probability that the minimum FOS falls below 1 in Equation 32.

$$p_f = P[F(x) \leq 1] \tag{32}$$

Where (x) is a vector of input parameters defined by their respective parameter distributions, ($F(x)$) is the resulting minimum FOS as an output of the surrogate model, and P describes the probability of this minimum FOS to fall below 1. The requirement of $F(x) \leq 1$ for slope instability does not mean failure of the entire dike but is rather an anticipation of failure, which may lead to a complete failure with time.

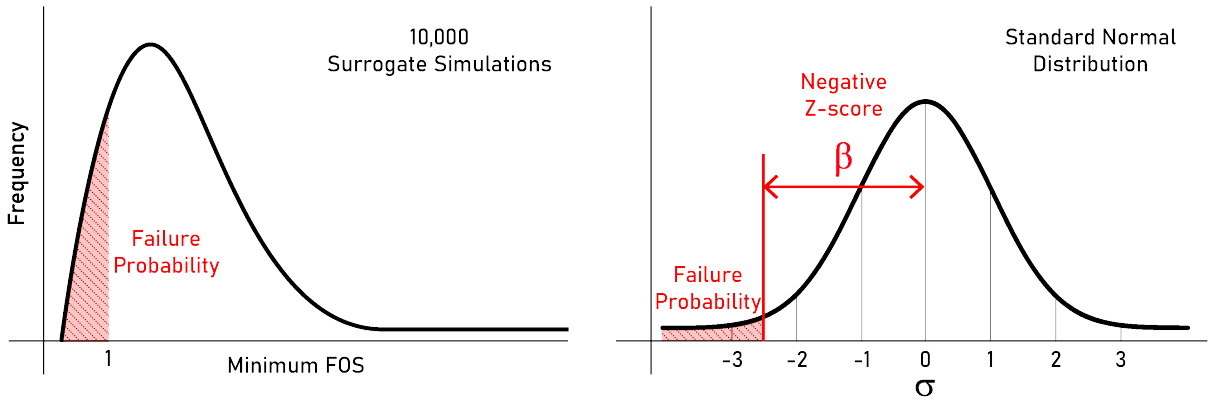

Figure 35: The reliability index is calculated as the negative z score of the failure probability under a standard normal distribution

The failure probability is often quantified as a safety or reliability index (Rijkswaterstaat, 2016; Roos et al., 2011). The reliability index can be approximated as the negative z score of the failure probability in a standard normal distribution (Figure 35). This failure probability indicates the failure region in the limit state probability distribution,

which is the difference between the resistance and load distributions (Roos et al., 2011). Considering the maximum failure probability for the modelled dike, the reliability index for the macro-stability of the inner slope, according to legislation, is 2.95. A Latin hypercube of 10,000 input parameter sets from the input distributions was used to run the surrogate model and calculate the failure probabilities per storm return period. Finally, the reliability index per storm return period was calculated for several storms (defined in Figure 29) and compared with legislation in Figure 36.

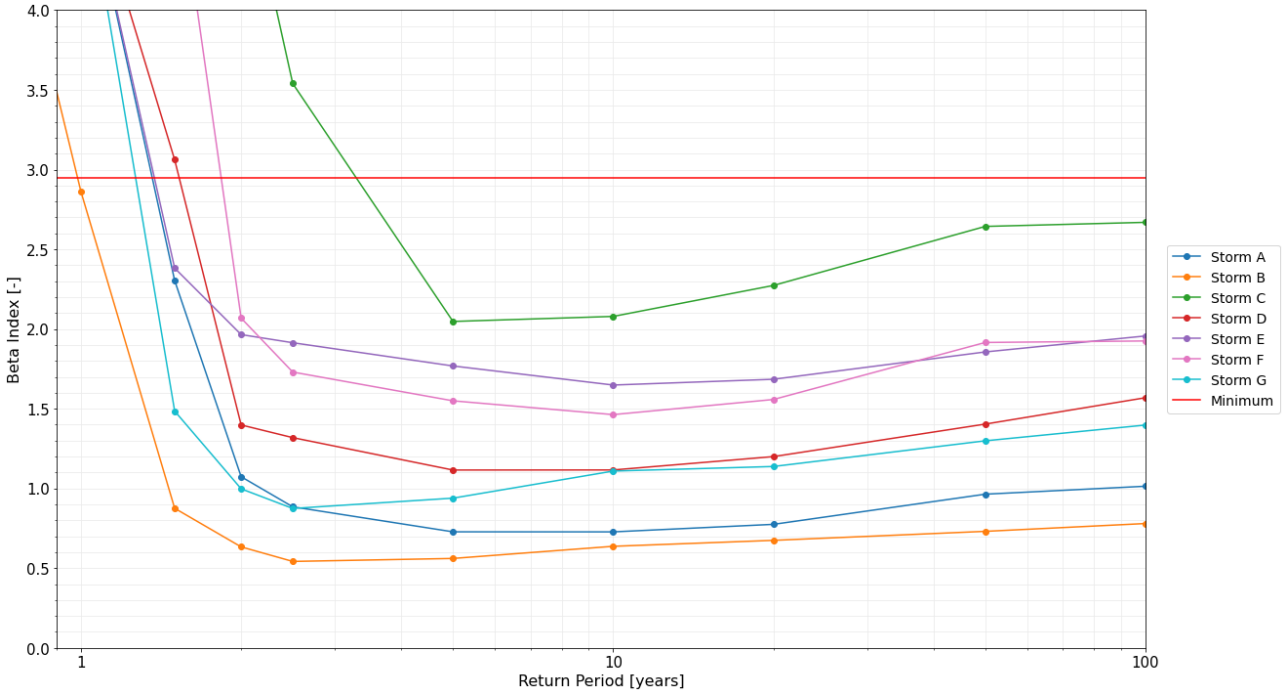

Figure 36: Reliability index per return period for different storms compared to the minimum required by legislation.

Figure 36 indicates that most storms with an associated return period of 1 year and above fall below the minimum reliability index of 2.95. This figure evaluates the dynamic influence of preferential flow on the reliability index with different storm shapes. Storms B, A, and G are the most dangerous and yield the lowest reliability indices. In contrast, storm C has the highest reliability index out of all tested storms. However, once the storm return period exceeds five years, it also falls below the minimum of 2.95 set by legislation.

Several studies aimed to demonstrate the influence of rainfall patterns on slope stability (Liu et al., 2021; Ghani et al., 2020; Rahardjo et al., 2001). These studies investigated rainfall patterns similar to storms A to C and found that delayed storms with a late peak, such as storm B, yield a slower but larger buildup of pore water pressures leading to slope failure. Furthermore, advanced storms with an early peak, such as storm C, result in a faster but lower buildup of pore water pressures (Liu et al., 2021). Thus, slope stability is governed by the rate of increase in pore pressures and the decrease of matric suction when rainwater infiltrates, as this decreases the effective stresses of the soil (Ghani et al., 2020). Figure 36 shows a similar trend as storm B and storm C show the lowest and highest reliability indices. This indicates that they lead to the highest and lowest failure frequency out of the studied rainfall patterns. Therefore, the FOS of the dike is strongly affected by the rainfall pattern.

5. Discussion

5 Discussion

In section 5.1, the limitations of the methodology are explained. Due to the theoretical nature of this research, the results rely heavily on the assumptions. Finally, the results are discussed in section 5.2.

5.1 Limitations of the method

5.1.1 Numerical representation of hydrological processes and slope assessment

Any assumptions in conceptualizing the FEM and the surrogate model will affect the model results. First, the limitations and simplifications of the FEM are discussed. Subsequently, the limitations of the surrogate model performance are evaluated.

The DPM applies Richards' equation (Richards, 1931) to approximate water flow in the unsaturated zone based on gravity and capillary flow (Farthing & Ogden, 2017). Wang & Narasimhan (1993) noted that the aperture of the fractures has a limited range of validity under capillary theory. The radius of the meniscus inside parallel plates will gravitate towards infinity for very large apertures resulting in no capillary rise. Hence, fractures occupying a maximum width larger than 3.83mm cannot be described using the capillary rise relation and should be assigned the highest possible α value (Aguilar-López et al., 2020). However, as noted in Figure 25, parameter b is sampled for larger radii than 3.83mm. For simplicity, the α value in the fractures was maintained at 1.41. Additionally, the approximation of laminar viscous fluid flow represented as porous media flow depends on the assumption that the inner fluxes remain in the laminar regime (Snow, 1965; Aguilar-López et al., 2020). To evaluate the inner fluxes, the maximum velocity in the cracked top layer was determined for the high-intensity reference scenario (Table 4). This maximum velocity is 0.0033 m/s, resulting in a Reynolds number of 10.05, classifying it as laminar flow. The maximum inflow velocity and the resulting Reynolds number depend on the fracture aperture (b) and the rainfall intensity (R) imposed at the boundaries. Hence, an input parameter combination may result in a simulation where the inner fluxes could be classified as turbulent. Parameter combinations that may result in turbulent flow are located in the right tail end of the input distributions of parameters b and R (Figure 25).

Several assumptions were made to emulate the cracked top layer. The cracks were distributed in a uniform 30cm deep cracked top layer along the rainfall surfaces and split into several subdomains. However, since the toe of the dike has a higher moisture content as its closer to the phreatic surface, the cracks are less likely to develop near the toe than in the crest of the dike (Elias et al., 2001). In this study, each cracked subdomain has one crack width to approximate the saturated hydraulic conductivity in a DPM framework. However, in reality the crack width is greatest at the surface and decreases with depth (Dyer et al., 2009). Additionally, the matrix saturation at the surface approximated soil swelling for each subdomain. This approximation disregards any differential soil swelling below the surface. Furthermore, crack formation, and soil swelling depend on the clay content of the soil (Dyer et al., 2009; J. Li & Zhang, 2010; Konrad & Ayad, 1997; McKay et al., 1993; Messing & Jarvis, 1990). The approximated sandy clay dike may have different soil and swelling parameters than those found in the literature. By adopting a dual permeability framework with Richards' equation, the fractures fill from top to bottom. However, given the high saturated hydraulic conductivity of the fractures, water will infiltrate to the bottom of the fractures within seconds. This was also demonstrated by Aguilar-López et al. (2020). These assumptions were necessary to approximate the fast-flowing behavior of the clay fractures.

In the Netherlands, dikes often have a vegetative cover which increases the resistance to erosion and restricts the development of cracks (J. Li et al., 2016). This study does not include this vegetative cover which is likely to influence the infiltration at the surface and the water retention capacity of the soil (Duan et al., 2011).

As mentioned, evaporation and overland flow were not simulated by the FEM, but if considered, they can have large implications on the results. Early configurations of the FEM included the inner drying of the cracks. Due to the nonlinear behavior of the steep retention curve in the cracks, the draining of the cracks resulted in long simulation times and numerical instability. Therefore, it was chosen to fixate the saturation once the pressure head became greater than the field capacity (-3.3m). This means that the cracks become fully saturated as soon as infiltration starts. In reality, cracks can desaturate very quickly due to drainage or evaporation, which should influence the propagation of the wetting front. Since flow through the cracks is limited under low saturation, the exchange of water toward the matrix below the wetting front is restricted. When drying is considered, the speed at which the wetting front advances reduces after the storm. Evaporation was also ignored under the assumption that the magnitude was much lower than the inflow imposed at the boundaries and that it takes much longer than the

storm extent. However, this assumption is less valid under low-intensity storms with a high return period as these storms have a low magnitude of the imposed inflow and a long storm extent. Another assumption of the FEM was that overland flow was disregarded. When the infiltration capacity at the surface is exceeded, overland flow occurs, which influences the ponding head. The increase in ponding head increases the Dirichlet flux at the rainfall boundaries once the pressure head at the surface is greater than zero. In a similar study by S. Li et al. (2021), a coupled surface runoff model was used to study the influence of the ponding depth on the infiltration rate at the surface and also considered a DPM with a matrix and preferential flow domain. S. Li et al. (2021) found that an increase in the ponding head can significantly affect the wetting front depth in the preferential flow domain and that the rainfall intensity weakly influences the infiltration rate. However, they considered high-intensity rainfall where the infiltration capacity was exceeded within a short timespan to generate surface runoff. Therefore, if changes in the ponding head were considered in this research, it would affect the rate of infiltration and the resulting change in macro-stability.

The C-Phi reduction method was used to assess the change in macro-stability due to the presence of cracks. The shear strength of cohesive soils with low permeability, such as clay and peat, is affected by their stress history. Given that regional dikes are often subjected to traffic loads, the induced consolidation is likely to affect the slope stability (Simanjuntak et al., 2019). One approach which includes the influence of the stress history on the shear stress is the SHANSEP approach which stands for Stress History and Normalized Soil Engineering Property (Simanjuntak et al., 2019). The shear strength is subjected to a defined stress path in this approach. A series of laboratory tests are performed to determine the stress path and calculate the over-consolidation ratio, which directly affects the undrained shear strength of the soil. Since the modelled dike consists of a low permeable cohesive soil, the consolidation history will likely affect the stability. Furthermore, Iereidis (2019) found that the SHANSEP method results in a larger and deeper slip surface than the C-Phi reduction method. To assess the benefits of considering the stress history, a comparison should be made between the SHANSEP and C-Phi reduction methods for assessing slope stability under rainfall infiltration. In this study, the soil material parameters (Table 2) remained constant in each simulation. This allowed for the investigation of the effect of moisture content changes on the dike's effective stresses. The FOS throughout the rainfall simulation was determined based on these soil parameters and changes in the moisture content in the dike. A change in the soil material properties will change the FOS in all timesteps of the rainfall simulation (Zhang & Chen, 2006; Fredlund & Thode, 2015).

5.1.2 Surrogate model errors

Any error found in the FEM is effectively translated into the surrogate model. Therefore, the quality of the training data is imperative to the accuracy and precision of the surrogate model, as it interpolates between the training data points. Numerical instability in the FEM was found both in the rainfall simulation and the slope stability assessment of the FEM. Errors found in the FOS timeseries from the C-Phi reduction method have affected the accuracy of several timesteps. These errors occur due to the continuation of the slope assessment, which leads to an overestimation of the FOS. The performance of the surrogate model is affected to a larger extent if the error is found in consecutive timesteps. Furthermore, the surrogate model was executed twice to extend the timeseries window, which amplified the error of the initial pressure head points.

In this research, the surrogate model was tested for its extrapolation capability. Firstly, the training data was limited to timeseries where the FOS is above 1. This was because the FOS timeseries became unreliable when the FOS was below 1. Nevertheless, in the reliability index comparison, the surrogate model was used to evaluate when the FOS fell below 1. Thus, the surrogate model utilized patterns found in the training data to extrapolate the extreme scenarios when the FOS fell below 1. Hence, the accuracy of the surrogate model for these extremes is limited by its extrapolation capability. Furthermore, when the surrogate model was tested on several rainfall patterns, it was extrapolating as training data was limited to storms with a maximum rainfall intensity of twice the average rainfall intensity. However, at several timesteps in the tested storms, the maximum rainfall intensity was greater than twice the average rainfall intensity. Therefore, the surrogate model was extrapolating for these timesteps. After comparing the FOS timeseries produced by the surrogate model with the results from the FEM for storms D-G in Figure 29, it can be concluded that this has a minimal influence on the accuracy.

5.2 Examination of results

The results revealed that several design choices limited the numerical representation of the hydrological processes in the canal dike.

In the low-intensity rainfall reference scenario (Table 4), the dike's macro-stability depends on the connectivity

among the cracks. This can be concluded by the evaluation scenarios in section 2.3.2.3, where the connectivity among the cracks was evaluated. It was shown that an absence of connected surface cracks reduces the drainage of the slope towards the toe resulting in a lower safety factor. Moreover, soil swelling in the cracks near the toe of the dike restricts drainage. The surrogate model was trained on results from the FEM, which considered a uniform layer of connected surface cracks. The local sensitivity analysis found that low-intensity rainfall (R ¡ 3mm/h) results in a higher FOS than high-intensity rainfall. Since the connectivity between preferential flow paths enhances water drainage out of the dike, the results from the surrogate model rely on a model setup with connected surface cracks. Therefore, the fully connected surface cracks are the largest source of uncertainty under low-intensity rainfall.

In the high-intensity rainfall scenario (Table 4), the presence of soil cracks expedites the propagation of the wetting front, resulting in a large decline in the macro-stability of the dike after the storm. For numerical stability and time efficiency, cracks under soil swelling were assigned a minimum volumetric crack ratio (wPf). By adopting this minimum threshold, the cracks never fully close. The minimum observed fracture width under the high-intensity reference scenario was 0.06mm, which indicates that the cracks are almost fully closed. Reducing the minimum wPf, limited the propagation of the wetting front, but resulted in longer computational times (from minutes to several hours). Baram et al. (2012) conducted field measurements in Israel on clayey soils and found that cracks never fully closed over successive winter seasons. In another study by Yesiller et al. (2000), multiple cycle tests were performed on clay soil, and they found that wetting provided some healing, but the cracks did not fully heal. These studies indicate that although soil swelling during saturation may provide healing, the cracks remain weak zones. The results found under high-intensity rainfall rely on the assumption that the cracks do not fully close. The surrogate model found slope failure (FOS < 1) mainly occurred under high-intensity rainfall. Therefore, the failure probabilities determined from the surrogate model also depend on the assumption that the cracks do not fully close. If the cracks are closed and fully healed over the winter, the speed at which the wetting front moves through the cracked top layer reduces sharply. This will effectively reduce the amount of infiltrated water and ultimately decrease the observed failure probabilities found by the surrogate model.

In the local sensitivity analysis, the study parameters were varied for a wider range than the surrogate model was trained on. In Figure 33, this was most noticeable for the average rainfall intensity, as under a high rainfall intensity ($R \geq 22$mm/h), the minimum FOS increased sharply. These high parameter values were sampled less in the training data; therefore, the surrogate model's extrapolating capacity was limited for these extremes.

The study parameters were treated as independent input variables to the surrogate model. However, the sensitivity analyses found that the input variables are correlated with one another. This was demonstrated by the higher order sensitivity indices (difference between total and first Sobol indices) in the global sensitivity analysis and the large changes in the local sensitivity analysis when the reference parameter set changes. This is reasonable considering that the crack parameters (b and wPf) affect the intermittent crack spacing a, influencing the exchange between the domains in the cracked topsoil. Additionally, the rainfall parameters (R and Tr) influence the storm's duration through the IDF relation. Therefore, changes in the dike's macro-stability due to changes in the study parameters are partially attributed to their combined influence on these variables. This made it more difficult to isolate the influence of each study parameter. The reliability assessment was conducted using a Latin hypercube sampling plan of 10,000 parameter sets based on the input parameter distributions (Figure 25). Therefore, when comparing the reliability indices with the legislative minimum, the validity of the input distributions should be considered. Since the input distributions aim to be all-encompassing and may include more extremes, the calculated failure probability can be lower in reality.

6. Conclusion & Recommendations

6 Conclusion & recommendations

This thesis presents the effect of rainfall-induced preferential flow through cracks on the macro-stability of a canal dike. An FEM was built to study the complex phenomena of preferential flow through soil cracks. A surrogate model was built using training data generated by the FEM to analyze the effects of a wide range of rainfall and crack parameters. In section 6.1, the main conclusions are presented by answering the research questions. Recommendations for further research are made in section 6.2.

6.1 Conclusion

This section answers the main research question: *"How does rainfall-induced preferential flow in soil cracks affect the macro-stability of canal dikes?"*

6.1.1 How to model rainfall infiltration through cracks on the slope stability of a canal dike?

Rainfall infiltration through soil cracks into a canal dike depends on the cracks, the soil, and the rainfall. A dual permeability model can capture the fast hydrological response of the cracks to rainfall. Furthermore, the C-Phi reduction method can quantify the effect of rainfall infiltration through soil cracks on the dike stability.

Under low-intensity rainfall, the dike stability is controlled by the connectivity among soil cracks. In general, cracks in the crest of the dike enhance infiltration, while cracks in the toe facilitate drainage of water out of the dike. In a model setup with connected cracks along the inner slope, the high connectivity among the cracks results in more water drainage out of the dike. Therefore, the dike stability decreases only slightly after the storm. In a model setup without cracks in the toe of the dike, the stability reduces sharply after the storm. It is found that infiltration increases through cracks in the crest without sufficient drainage of water in the toe, resulting in the buildup of water and a lower dike stability. Under high-intensity rainfall, cracks in the crest and inner slope of the dike expedite the advancement of the wetting front in the soil matrix. This is due to the exchange of water from the fracture to the matrix below the wetting front. A faster advancement of the wetting front increases the buildup of water in the toe of the dike, effectively reducing the dike stability after the storm. Evaluation scenarios reveal that soil swelling in the toe restricts water drainage out of the dike, resulting in a lower dike stability. Furthermore, the addition of matric suction has a beneficial effect on the dike stability.

6.1.2 How to build a surrogate model of rainfall infiltration through cracks and its effect on the slope stability?

A surrogate model was made to emulate the effect of rainfall infiltration through cracks on the slope stability. The inputs and outputs to the surrogate model should describe the variability of results of the underlying FEM. The slope stability at each instance is affected by the memory of the moisture content and the incoming rainfall. Therefore, a machine-learning model that can model the memory of the hydrology in the dike was chosen as the surrogate model architecture. The crack (maximum crack aperture and the amount of cracking) and rainfall parameters (average rainfall intensity and return period) were included as static input parameters to the surrogate model to reproduce the fast hydrological response of the cracks. In addition, a hyetograph timeseries was included as a dynamic input parameter to model the change in the slope stability in response to a simulated storm. The dynamic outputs included the timeseries of the pressure head in forty well-distributed points and the timeseries of the safety factor to quantify the effect of the change in moisture content on the slope stability. The surrogate model was sufficiently trained due to data augmentation and an efficient parameter sampling strategy. By comparing the results of the surrogate model with the results of the FEM, it was found that the surrogate model can reproduce the safety factor timeseries in response to rainfall infiltration.

6.1.3 What is the effect of varying the crack and rainfall parameters on the slope stability?

The local sensitivity analysis reveals that the cracks facilitate more infiltration when the crack parameters (maximum crack width and the amount of cracking) are below a threshold, resulting in a lower dike stability. Above this threshold, the cracks can facilitate more drainage of water out of the dike. An increase in the rainfall parameters (average rainfall intensity and return period) decreases the dike stability. In an analysis of the effect of the rainfall and crack parameters on the phreatic surface, it is found that soil cracks influence the shape of the phreatic surface by increasing the buildup of water in the toe of the dike. Additionally, the shape of the phreatic surface affects the dike stability. Furthermore, a delayed storm, where the rainfall intensity incrementally increases over time, provides the highest failure probability.

The influence of rainfall-induced preferential flow through soil cracks on the macro-stability of a dike is controlled by a delicate balance between infiltration and drainage. Water infiltration and drainage in a cracked dike depend on rainfall characteristics such as the average rainfall intensity, duration, and pattern and on the crack features such as the crack width, amount of cracking, and the connectivity of the cracks.

6.2 Recommendations for further studies

Based on the results of this study, several recommendations for further research are made.

1. **Study the spatial variation in surface cracks.** This study has shown that the macro-stability of a dike can depend strongly on the infiltration and drainage provided by surface soil cracks. Under high-intensity rainfall, the wetting front reached the bottom of the cracked layer. Therefore the depth of the cracks is a limiting factor and can affect the amount of infiltration. It is recommended to investigate how the depth and the crack parameters spatially vary along the seepage boundaries and their influence on the macro-stability of the dike.

2. **Fixed geometry of the dike.** The geometry of the dike was fixed in this study. Furthermore, as indicated by the phreatic surface analysis, the road profoundly influences the rise in the phreatic surface. Furthermore, the width of the dike can have a large influence on the macro-stability. This is due to the location of the phreatic line relative to the surface. Hence a larger unsaturated zone might be found in a wider dike. By adopting a single geometry, the application range is also limited.

3. **Include evaporation and draining of cracks.** In this study, the cracks remained fully saturated during the simulation. This was a limitation implemented to improve the numerical stability. However, in reality, the cracks dry very quickly due to evaporation and drainage. Therefore, it is recommended to study how seepage in these cracks affects the found infiltration pattern.

4. **Geomechanic effect of cracks on the slope stability.** This study focused only on the hydrological response of the cracks on the slope stability. Therefore it is recommended to study the geomechanical influence of the cracks on the slope stability.

5. **Compare slope stability assessments.** The C-Phi reduction method was adopted to perform the slope stability assessment. However, since the modelled dike was a sandy clay dike prone to compaction, the stress history may influence the slope stability. Therefore a comparison should be made between the C-Phi reduction method and the SHANSEP method, which includes the effect of the stress history of the soil.

6. **Conduct field infiltration experiments.** As with many slope stability experiments, it is difficult to validate the results found. Therefore, performing an infiltration experiment on a dike with visible surface cracks is recommended. In addition, it is advised to observe the phreatic water level within the dike at several locations, as a change in the phreatic surface is the largest proxy for slope stability.

References

Abadi, M., Agarwal, A., Barham, P., Brevdo, E., Chen, Z., Citro, C., & Zheng, X. (2015). *TensorFlow: Large-scale machine learning on heterogeneous systems.* Retrieved from https://www.tensorflow.org/. (Software available from tensorflow.org)

Abd, I. A., Fattah, M. Y., & Mekkiyah, H. (2020). Relationship between the matric suction and the shear strength in unsaturated soil. *Case Studies in Construction Materials*, *13*. doi: 10.1016/j.cscm.2020.e00441

Aguilar-López, J. P., Bogaard, T., & Gerke, H. H. (2020). Dual-permeability model improvements for representation of preferential flow in fractured clays. *Water Resources Research*, *56*. doi: 10.1029/2020WR027304

Assouline, S., & Or, D. (2014). The concept of field capacity revisited: Defining intrinsic static and dynamic criteria for soil internal drainage dynamics. *Water Resources Research*, *50*. doi: 10.1002/2014WR015475

Azzini, I., Mara, T. A., & Rosati, R. (2021). Comparison of two sets of monte carlo estimators of sobol'indices. *Environmental Modelling & Software*, *144*, 105167.

Balbastre-Soldevila, R., García-Bartual, R., & Andrés-Doménech, I. (2019). A comparison of design storms for urban drainage system applications. *Water*, *11*(4), 757.

Baram, S., Kurtzman, D., & Dahan, O. (2012). Water percolation through a clayey vadose zone. *Journal of Hydrology*, *424*, 165–171.

Beersma, J. J. (2019). *Neerslagstatistiek en -reeksen voor het waterbeheer 2019*. STOWA.

Benahmed, N., & Bonelli, S. (2012). Investigating concentrated leak erosion behaviour of cohesive soils by performing hole erosion tests. *European Journal of Environmental and Civil Engineering*, *16*(1), 43–58.

Berhane, G. (2010). Engineering geological soil and rock characterization in the mekelle town, northern ethiopia: implications to engineering practice. *Momona Ethiop J Sci*, *2*(2), 64–86.

Beven, K., & Germann, P. (2013). Macropores and water flow in soils revisited. *Water Resources Research*, *49*. doi: 10.1002/wrcr.20156

Carsel, R. F., & Parrish, R. S. (1988). Developing joint probability distributions of soil water retention characteristics. *Water resources research*, *24*(5), 755–769.

Celia, M. A., Bouloutas, E. T., & Zarba, R. L. (1990). A general mass-conservative numerical solution for the unsaturated flow equation. *Water resources research*, *26*(7), 1483–1496.

Chertkov, V., & Ravina, I. (2001). Effect of interaggregate capillary cracks on the hydraulic conductivity of swelling clay soils. *Water Resources Research*, *37*(5), 1245–1256.

Chotkan, S., van der Meij, R., Klerk, W. J., Vardon, P. J., & Aguilar-López, J. P. (2022). A data-driven method for identifying drought-induced crack-prone levees based on decision trees. *Sustainability*, *14*(11), 6820.

Chow, V. T. (1965). Handbook of applied hydrology. *International Association of Scientific Hydrology. Bulletin*, *10*. doi: 10.1080/02626666509493376

Chui, T. F. M., & Freyberg, D. L. (2009). Implementing hydrologic boundary conditions in a multiphysics model. *Journal of Hydrologic Engineering*, *14*(12), 1374–1377.

Dawson, E., Roth, W., & Drescher, A. (1999). Slope stability analysis by strength reduction. *Geotechnique*, *49*(6), 835–840.

Duan, R., Fedler, C. B., & Borrelli, J. (2011). Field evaluation of infiltration models in lawn soils. *Irrigation Science*, *29*(5), 379–389.

Dunne, T., Zhang, W., & Aubry, B. F. (1991). Effects of rainfall, vegetation, and microtopography on infiltration and runoff. *Water Resources Research*, *27*(9), 2271–2285.

Dyer, M., Utili, S., & Zielinski, M. (2009). Field survey of desiccation fissuring of flood embankments. *Proceedings of the Institution of Civil Engineers: Water Management*, *162*. doi: 10.1680/wama.2009.162.3.221

Elias, E., Salih, A., & Alaily, F. (2001). Cracking patterns in the vertisols of the sudan gezira at the end of dry season. *International agrophysics*, *15*(3).

Fan, Y., & Miguez-Macho, G. (2011). A simple hydrologic framework for simulating wetlands in climate and earth system models. *Climate dynamics*, *37*(1), 253–278.

Farthing, M. W., & Ogden, F. L. (2017). Numerical solution of Richards' equation: A review of advances and challenges. *Soil Science Society of America Journal*, *81*(6), 1257–1269.

Fong, J. (2019). *The advantages of the finite element method.* Retrieved September 28, 2022, from https://innovationatwork.ieee.org/the-advantages-of-fem.

Fredlund, M., & Thode, R. (2015). Poisson ' s ratio effect of slope stability calculations..

Gangopadhyay, S., Das Gupta, A., & Nachabe, M. (2001). Evaluation of ground water monitoring network by principal component analysis. *Groundwater*, *39*(2), 181–191.

Gerke, H. H., Dusek, J., & Vogel, T. (2013). Solute mass transfer effects in two-dimensional dual-permeability modeling of bromide leaching from a tile-drained field. *Vadose Zone Journal*, *12*. doi: 10.2136/vzj2012.0091

Gerke, H. H., Dusek, J., Vogel, T., & Köhne, J. M. (2007). Two-dimensional dual-permeability analyses of a bromide tracer experiment on a tile-drained field. *Vadose Zone Journal*, *6*(3), 651–667.

Gerke, H. H., & Van Genuchten, M. T. (1993a). A dual-porosity model for simulating the preferential movement of water and solutes in structured porous media. *Water resources research*, *29*(2), 305–319.

Ghani, A. N. C., Taib, A. M., & Hasbollah, D. Z. A. (2020). Effect of rainfall pattern on slope stability. In *Geotechnics for sustainable infrastructure development.* Springer.

Goemans, T., & Visser, T. (1987). The delta project: The Netherlands experience with a megaproject for flood protection. *Technology in Society*, *9*(1), 97–111.

Hadži-Niković, G., Rakić, D., & Djoković, K. (2015). Effect of changes in matric suction on slope stability in natural unsaturated soil..

Hendrickx, J. M., & Flury, M. (2001). Uniform and preferential flow mechanisms in the vadose zone. *Conceptual models of flow and transport in the fractured vadose zone*, 149–187.

HHNK. (2015). *Meten waterspanningen in kade per kadetype te Alkmaar in opdracht van Hoogheemraadschap Hollands Noorderkwartier.*

HHNK. (2022). *Legger waterkeringen.* Retrieved September 2, 2022 from https://www.hhnk.nl/legger-waterkeringen.

Huang, Z., Wei, B., Zhang, L., Chen, W., & Peng, Z. (2019). Surface crack development rules and shear strength of compacted expansive soil due to dry–wet cycles. *Geotechnical and Geological Engineering*, *37*(4), 2647–2657.

Iereidis, C. (2019). *Implementation of the new Dutch guidelines on the macrostability assessment of dikes using different constitutive models: Case study: Kijk dike in the Netherlands* (Master's thesis, TU Delft). Retrieved from https://repository.tudelft.nl/islandora/object/uuid%3Aa8cdff86-66a7-4251-afa4-c9a040e7ae7b.

IPCC. (2022). Sixth assessment report impacts, adaptation and vulnerability. *IPCC Sixth Assessment Report*.

Jabro, J. D. (1996). Variability of field-saturated hydraulic conductivity in a hagerstown soil as affected by initial water content. *Soil Science*, *161*(11), 735–739.

Jamalinia, E., Vardon, P. J., & Steele-Dunne, S. C. (2019). The effect of soil–vegetation–atmosphere interaction on slope stability: a numerical study. *Environmental Geotechnics*, *8*(7), 430–441.

Jaxa-Rozen, M., Pratiwi, A. S., & Trutnevyte, E. (2021). Variance-based global sensitivity analysis and beyond in life cycle assessment: an application to geothermal heating networks. *International Journal of Life Cycle Assessment*, *26*. doi: 10.1007/s11367-021-01921-1

Jolliffe, I. T. (2002). Principal component analysis, second edition. *Encyclopedia of Statistics in Behavioral Science*, *30*. doi: 10.2307/1270093

Kanning, W., Teixeira, A., van der Krogt, M., Rippi, K., Schweckendiek, T., & Hardeman, B. (2017). Calibration of factors of safety for slope stability of dikes.. doi: 10.1061/9780784480717.001

KNMI. (n.d.). *Daggegevens van het weer in Nederland.* Retrieved June 20 from https://daggegevens.knmi.nl/klimatologie/monv/reeksen.

Kodikara, J. K., Nahlawi, H., & Bouazza, A. (2004). Modelling of curling in desiccating clay. *Canadian Geotechnical Journal*, *41*(3), 560–566.

Konrad, J.-M., & Ayad, R. (1997). Desiccation of a sensitive clay: field experimental observations. *Canadian Geotechnical Journal*, *34*(6), 929–942.

Krzeminska, D., Bogaard, T., Van Asch, T. W., & Van Beek, L. (2012). A conceptual model of the hydrological influence of fissures on landslide activity. *Hydrology and Earth System Sciences*, *16*(6), 1561–1576.

Kukemilks, K., Wagner, J.-F., Saks, T., & Brunner, P. (2018). Conceptualization of preferential flow for hillslope stability assessment. *Hydrogeology journal*, *26*(2), 439–450.

Lanzafame, R., & Sitar, N. (2019). Reliability analysis of the influence of seepage on levee stability. *Environmental Geotechnics*, *6*(5), 284–293.

Le, T. M. H., Gallipoli, D., Sánchez, M., & Wheeler, S. (2015). Stability and failure mass of unsaturated heterogeneous slopes. *Canadian Geotechnical Journal*, *52*(11), 1747–1761.

Lendering, K. (2016). Failure probability of regional flood defences.. doi: 10.1051/e3sconf/20160701002

Lengkeek, H., De Greef, J., & Joosten, S. (2018). CPT based unit weight estimation extended to soft organic soils and peat. In *Cone penetration testing 2018.* CRC Press.

Li, J., Li, L., Chen, R., & Li, D. (2016). Cracking and vertical preferential flow through landfill clay liners. *Engineering Geology*, *206*, 33–41.

Li, J., & Zhang, L. (2010). Geometric parameters and REV of a crack network in soil. *Computers and Geotechnics*, *37*(4), 466–475.

Li, J. H., Wang, Z. F., & Zhang, L. M. (2011). Spatial variability of aperture in a rough-walled crack in surface soil.. doi: 10.1061/41183(418)22

Li, S., Jiang, Z., Que, Y., Chen, X., Ding, H., Liu, Y., & Xue, B. (2021). Water field distribution characteristics under slope runoff and seepage coupled effect based on the finite element method. *Water (Switzerland)*, *13*. doi: 10.3390/w13243569

Liu, Y., Deng, Z., & Wang, X. (2021). The effects of rainfall, soil type and slope on the processes and mechanisms of rainfall-induced shallow landslides. *Applied Sciences*, *11*(24), 11652.

Mahmood, K., Kim, J. M., & Ashraf, M. (2016). The effect of soil type on matric suction and stability of unsaturated slope under uniform rainfall. *KSCE Journal of Civil Engineering*, *20*(4), 1294–1299.

McKay, L. D., Cherry, J. A., & Gillham, R. W. (1993). Field experiments in a fractured clay till: 1. hydraulic conductivity and fracture aperture. *Water Resources Research*, *29*(4), 1149–1162.

Messing, I., & Jarvis, N. (1990). Seasonal variation in field-saturated hydraulic conductivity in two swelling clay soils in Sweden. *Journal of soil science*, *41*(2), 229–237.

Miebs, G., Mochol-Grzelak, M., Karaszewski, A., & Bachorz, R. A. (2020). Efficient strategies of static features incorporation into the recurrent neural network. *Neural Processing Letters*, *51*(3), 2301–2316.

Miller, C. T., Dawson, C. N., Farthing, M. W., Hou, T. Y., Huang, J., Kees, C. E., & Langtangen, H. P. (2013). Numerical simulation of water resources problems: Models, methods, and trends. *Advances in Water Resources*, *51*. doi: 10.1016/j.advwatres.2012.05.008

Mills, J. (n.d.). *Case study experiment - decline in organic matter in peat soils.* Retrieved April 22, 2022 from https://www.recare-hub.eu/case-studies/veenweidegebied-the-netherlands.

Monden, M., van Opstal, R., & Zwartedijk, B. (2020). *Optimalisatie van dijkversterkingen op basis van meting en modellering van het freatisch vlak.* Retrieved June 20, 2022, from https://www.gww-bouw.nl/artikel/optimalisatie-van-dijkversterkingen-op-basis-van-meting-en-modellering-van-het-freatisch-vlak/.

Morio, J. (2011). Global and local sensitivity analysis methods for a physical system. *European journal of physics*, *32*(6), 1577.

Novák, V., Šimåunek, J., & van Genuchten, M. T. (2000). Infiltration of water into soil with cracks. *Journal of Irrigation and Drainage Engineering*, *126*. doi: 10.1061/(asce)0733-9437(2000)126:1(41)

Novák, V., Šimåunek, J., & van Genuchten, M. T. (2002). Infiltration into a swelling, cracked clay soil. *Journal of Hydrology Hydromechanics*, *50*(1), 3–19.

Overleg, I. (1999). IPO-richtlijn ter bepaling van het veiligheidsniveau van boezemkaden. *IPO, Den Haag, The Netherlands*.

Rahardjo, H., Li, X., Toll, D. G., & Leong, E. C. (2001). The effect of antecedent rainfall on slope stability. In *Unsaturated soil concepts and their application in geotechnical practice*. Springer.

Richards, L. A. (1931). Capillary conduction of liquids through porous mediums. *Physics*, *1*(5), 318–333.

Rijkswaterstaat. (2016). Schematiseringshandleiding macrostabiliteit-WBI 2017. *RWS-WVL, Rapport, definitief, versienummer*, *1*(1), 169.

Rikkert, S. J. H. (2022). *A system perspective on flood risk in polder drainage canal systems* (Doctoral dissertation, TU Delft). Retrieved from https://repository.tudelft.nl/islandora/object/uuid%3A61e6645a-f275-4b69-aa29-1150d3cda2b1.

Roos, E., Wackenhut, G., Lammert, R., & Schuler, X. (2011). Probabilistic safety assessment of components. *International Journal of Pressure Vessels and Piping*, *88*(1), 19–25.

Saltelli, A., Tarantola, S., Campolongo, F., & Ratto, M. (2004). *Sensitivity analysis in practice. a guide to assessing scientific models. in: Probability and statistics series.*

Shao, W., Bogaard, T., Bakker, M., & Greco, R. (2015). Quantification of the influence of preferential flow on slope stability using a numerical modelling approach. *Hydrology and Earth System Sciences*, *19*(5), 2197–2212.

Sharma, H. D., Dukes, M. T., & Olsen, D. M. (1990). Field measurements of dynamic moduli and Poisson's ratios of refuse and underlying soils at a landfill site.. doi: 10.1520/stp25299s

Simanjuntak, T., Goeman, D., de Koning, M., & Haasnoot, J. (2019). *SHANSEP approach for slope stability assessments of river dikes in the Netherlands*. doi: 10.1201/9781351003629-39

Smits, I., Wijngaard, J., Versteeg, R., & Kok, M. (2004). Statistiek van extreme neerslag in Nederland. *STOWA, Utrecht*.

Snow, D. T. (1965). *A parallel plate model of fractured permeable media*. University of California, Berkeley.

Sobester, A., Forrester, A., & Keane, A. (2008). *Engineering design via surrogate modelling: a practical guide*. John Wiley & Sons.

Sobol', I. M. (1990). On sensitivity estimation for nonlinear mathematical models. *Matematicheskoe modelirovanie*, *2*(1), 112–118.

Soil profile cpt. (n.d.). Retrieved April 25, 2022 from https://bit.ly/3EQZH5J.

Stewart, R. D., Abou Najm, M. R., Rupp, D. E., & Selker, J. S. (2016). Modeling multidomain hydraulic properties of shrink-swell soils. *Water Resources Research*, *52*(10), 7911–7930.

Stone, J. J., Paige, G. B., & Hawkins, R. H. (2008). Rainfall intensity-dependent infiltration rates on rangeland rainfall simulator plots. *Transactions of the ASABE*, *51*(1), 45–53.

Ten Bokkel Huinink, J. (2016). *Assessment of the probability distribution of the phreatic surface in a regional flood defence: Finite element computation for a better understanding of the influence of precipitation on the phreatic surface* (Master's thesis, TU Delft). Retrieved from https://repository.tudelft.nl/islandora/object/uuid%3A7b3841dd-1eda-4fd9-aa32-5e1b074cf7c1.

Teunissen, H., & Zwanenburg, C. (2017). Modelling strains of soft soils. *Procedia Engineering*, *175*, 165–174.

van den Akker, J., Hendriks, R., Frissel, J., Oostindie, K., & Wesseling, J. (2014). *Gedrag van verdroogde kades : fase b, c, d: onstaan en gevaar van krimpscheuren in klei- en veenkades*. Alterra.

Van Genuchten, M. T. (1980). A closed-form equation for predicting the hydraulic conductivity of unsaturated soils. *Soil science society of America journal*, *44*(5), 892–898.

Viana, F. A. C. (2013). Things you wanted to know about the latin hypercube design and were afraid to ask. *10th World Congress on Structural and Multidisciplinary Optimization*.

Vogel, T., Gerke, H. H., Zhang, R., & Van Genuchten, M. T. (2000). Modeling flow and transport in a two-dimensional dual-permeability system with spatially variable hydraulic properties. *Journal of hydrology*, *238*(1-2), 78–89.

Wang, J., & Narasimhan, T. (1993). *Unsaturated flow in fractured porous media*. doi: 10.1016/b978-0-12-083980-3.50011-5

Yesiller, N., Miller, C., Inci, G., & Yaldo, K. (2000). Desiccation and cracking behavior of three compacted landfill liner soils. *Engineering geology*, *57*(1-2), 105–121.

Zhang, P. W., & Chen, Z. Y. (2006). Influences of soil elastic modulus and Poisson's ratio on slope stability. *Yantu Lixue/Rock and Soil Mechanics*, *27*.

Appendices

Appendix A: Soil swelling in reference scenarios

Observable changes in the study parameters b and wPf due to soil swelling at the start and end of the reference scenarios (low and high intensity rainfall). Do note that they have the same starting setup as the only difference between the reference scenarios is the average rainfall intensity. The dark blue line indicates the phreatic line.

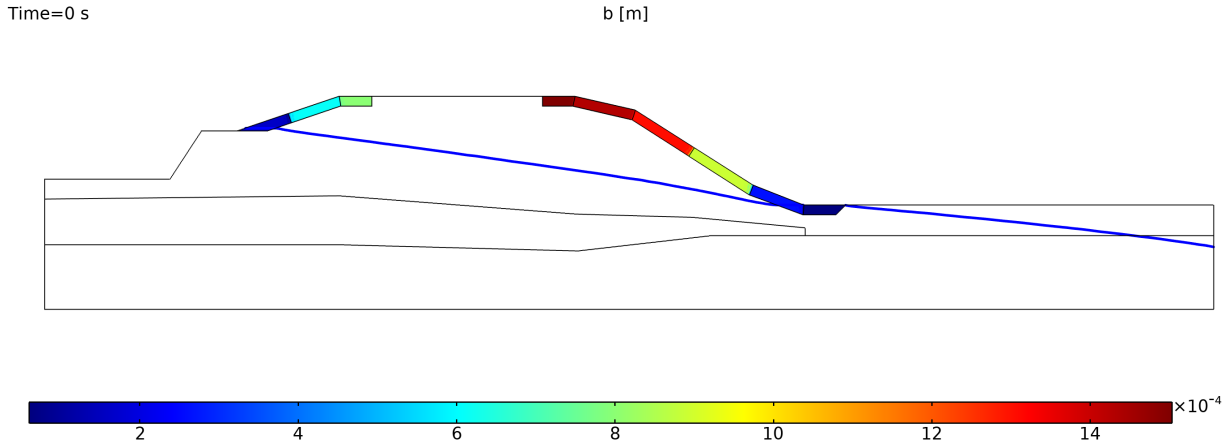

Figure 37: Spatial distribution of b at the start of the storm

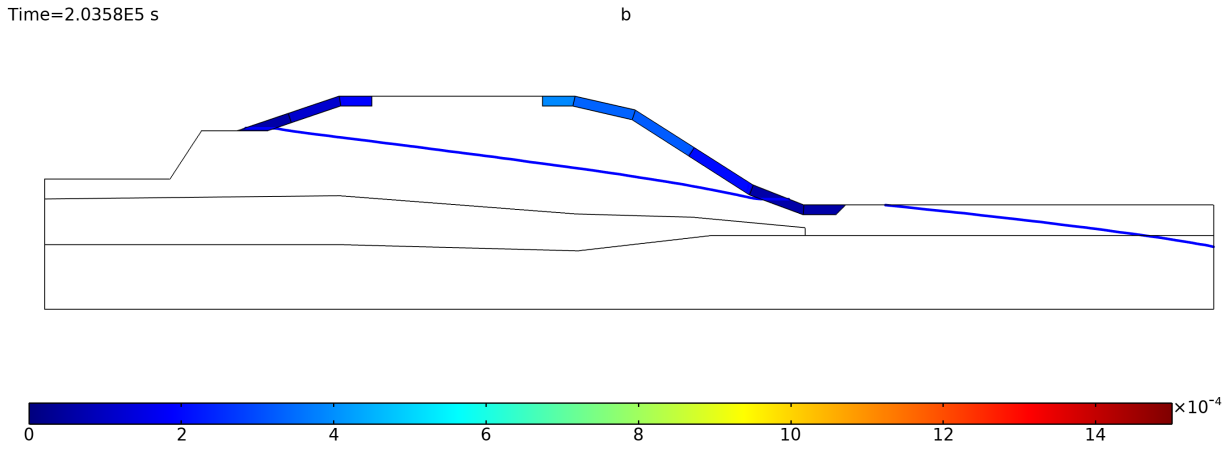

Figure 38: Spatial distribution of b at the end of a low rainfall intensity storm

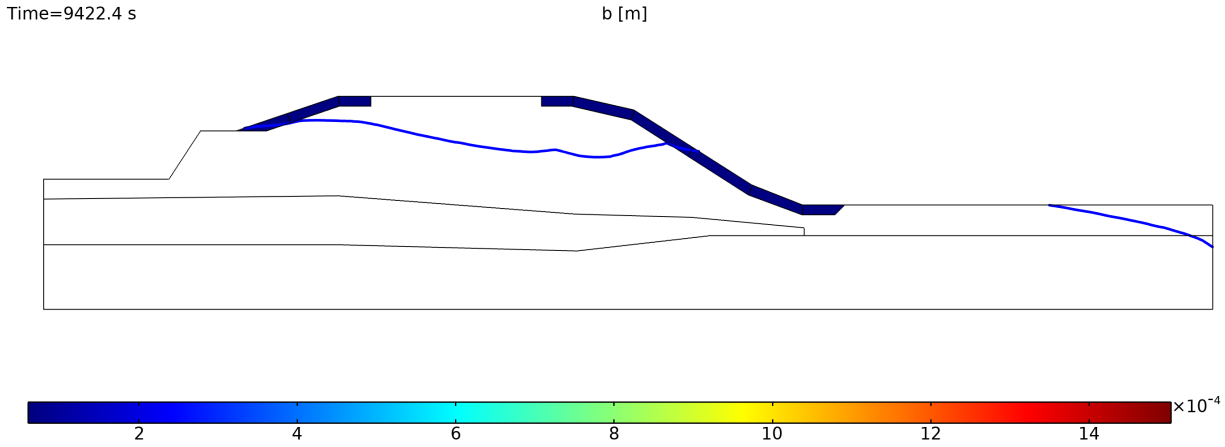

Figure 39: Spatial distribution of b at the end of a high rainfall intensity storm

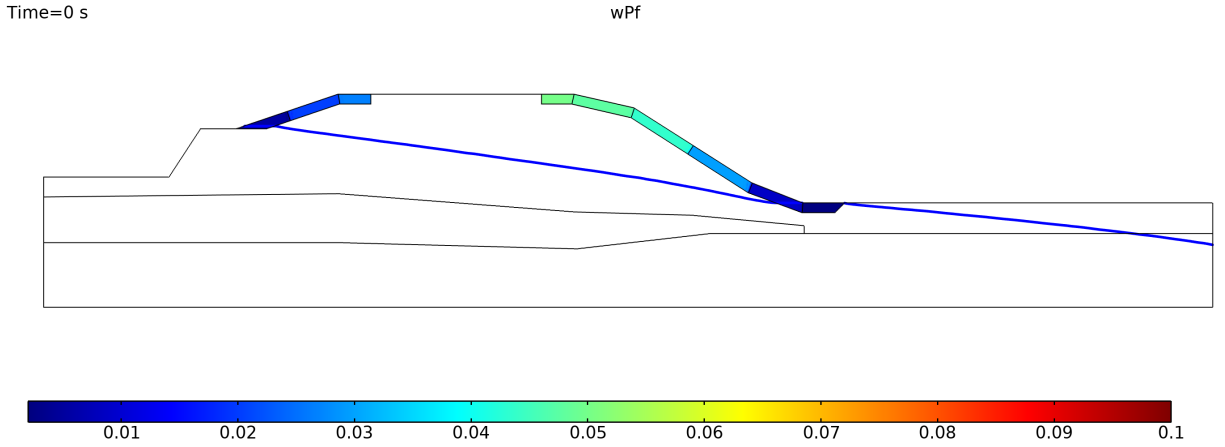

Figure 40: Spatial distribution of wPf at the start of the storm

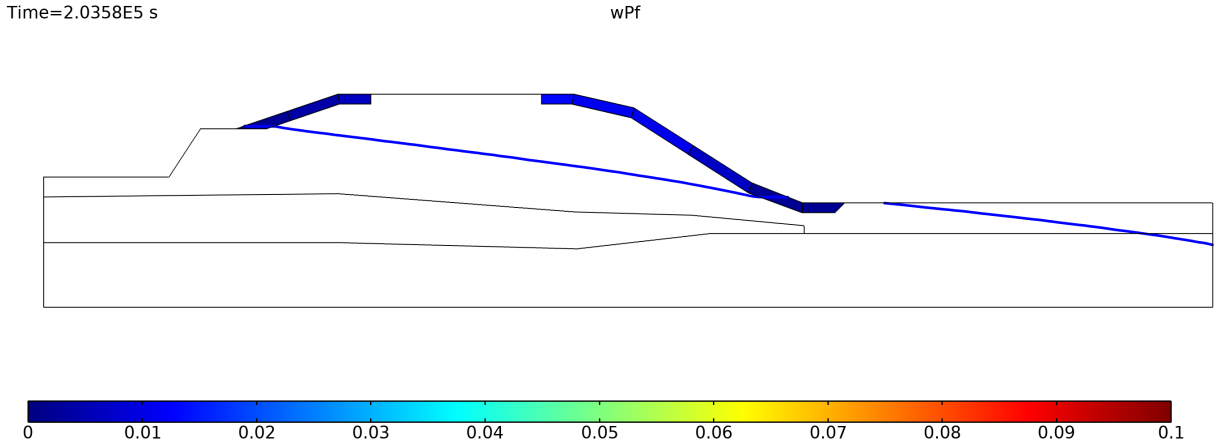

Figure 41: Spatial distribution of wPf at the end of a low rainfall intensity storm

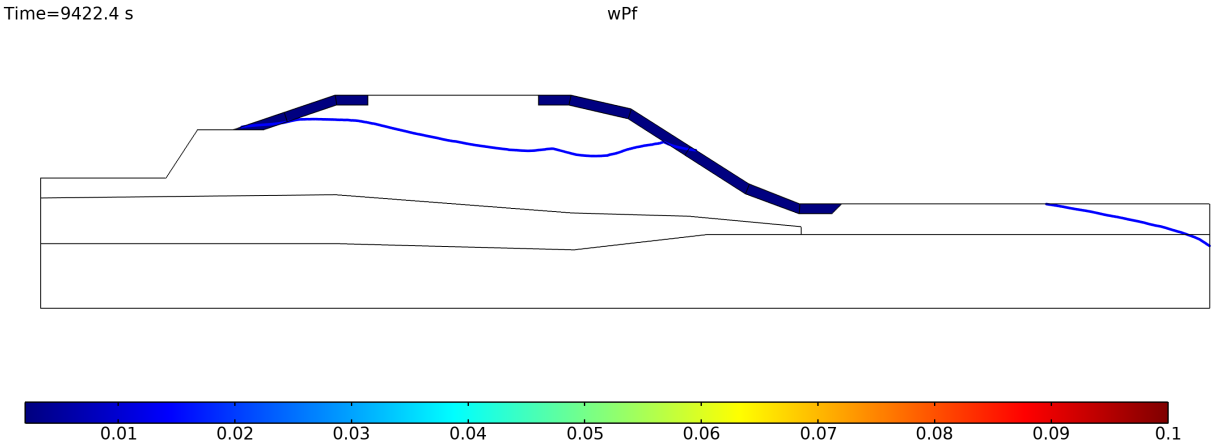

Figure 42: Spatial distribution of wPf at the end of a high rainfall intensity storm

Appendix B: Introduction to principal component analysis

Principal component analysis (PCA) is a common strategy used in machine learning for data dimensionality reduction while maintaining the variation in the data set (Gangopadhyay et al., 2001). PCA describes the total variance of individual correlated measurements using a selected number of principal components. Hence PCA derives relationships between the hydraulic head measurements to form components that describe the most variation of the system. These components are called principal components (PCs) and are linear combinations of the original variables. The first principal component (PC1) describes the most variance of the system, followed by the second principal component (PC2), and so on. Each principal component is perpendicular to one another. This analysis transforms the original correlated data into a new coordinate system of uncorrelated variables. The number of generated PCs, (m), is related to the number of observations, (n) and variables, (p), through $m = min(n-1, p)$ (Jolliffe, 2002).

Appendix C: Local sensitivity analysis

A OAT analysis was done for each reference rainfall pattern. Storm B is presented in figures 32 and 33.

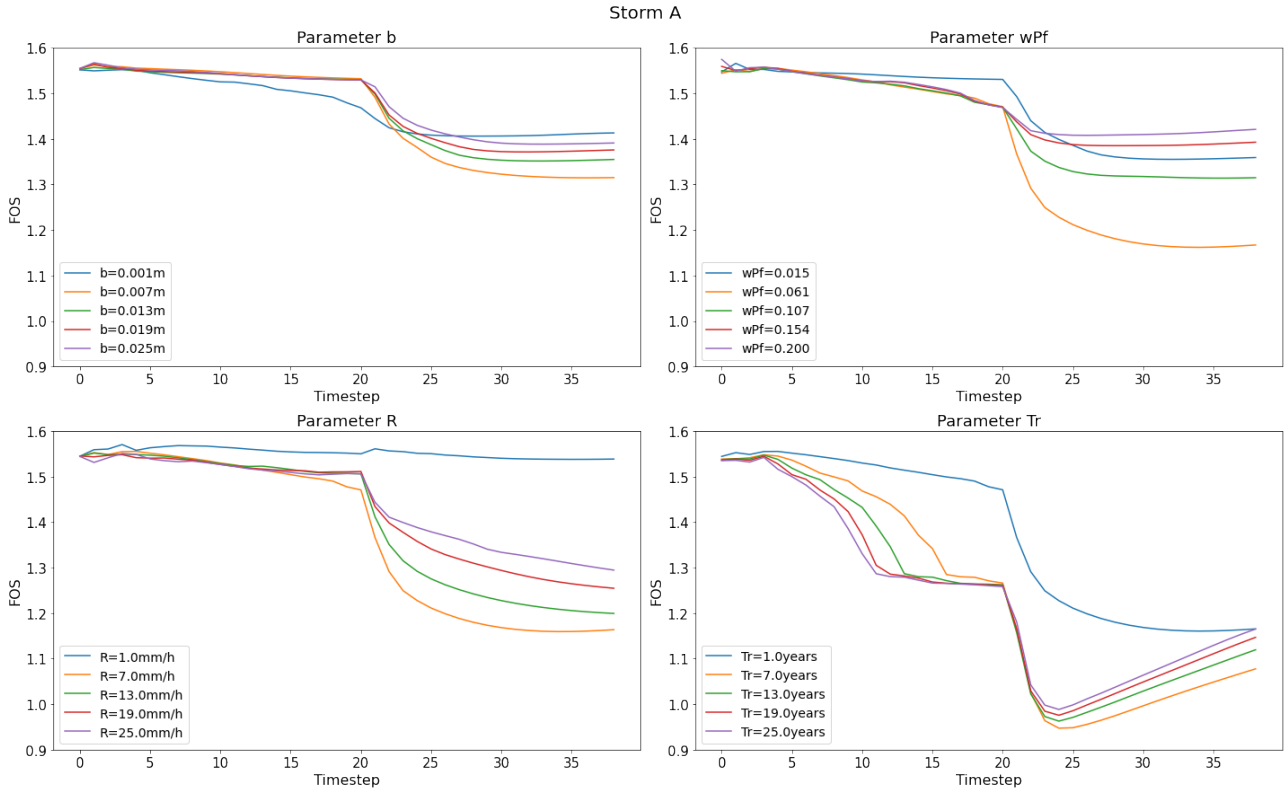

Figure 43: OAT analysis of the study parameters on the FOS timeseries of storm A.

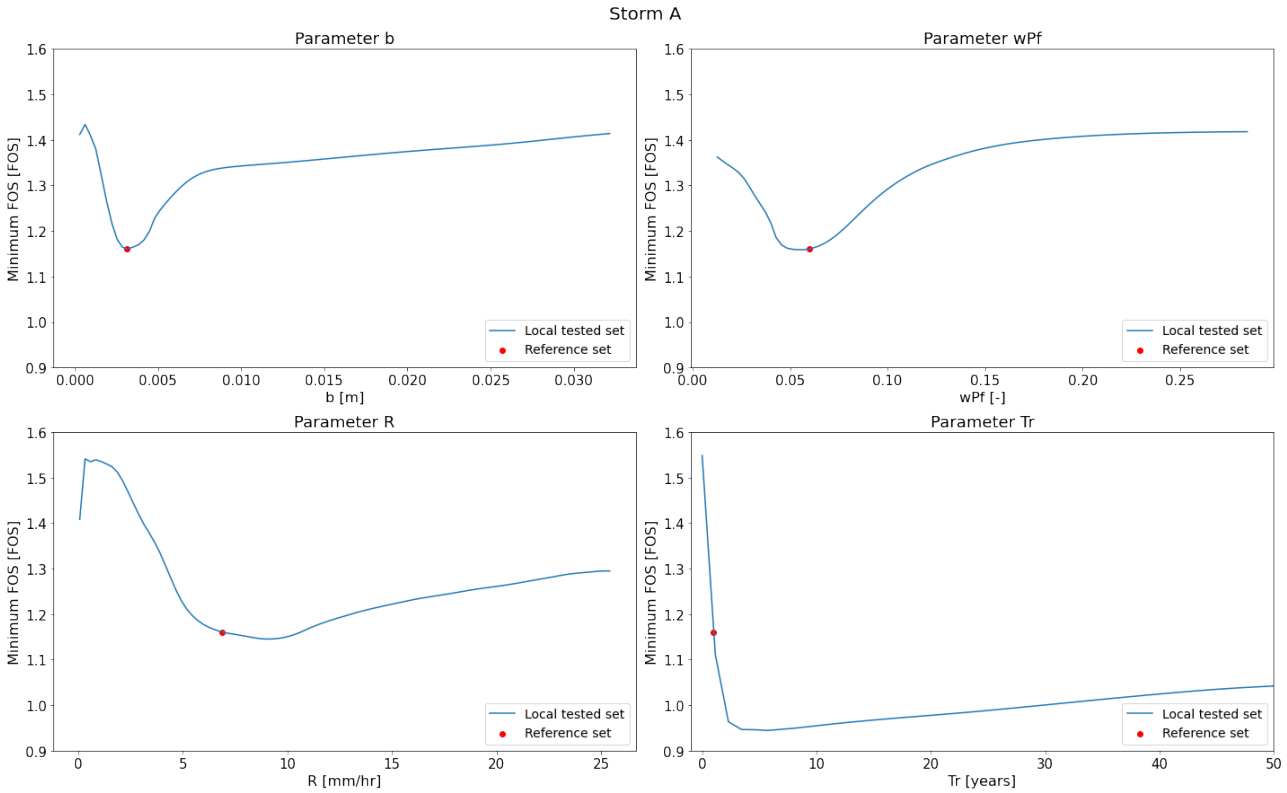

Figure 44: OAT analysis of the study parameters on the minimum FOS of storm A. The minimum FOS of the reference parameter set (b=3.15mm, wPf=6%, R=6.89mm/h, Tr=1year) was plotted in red.

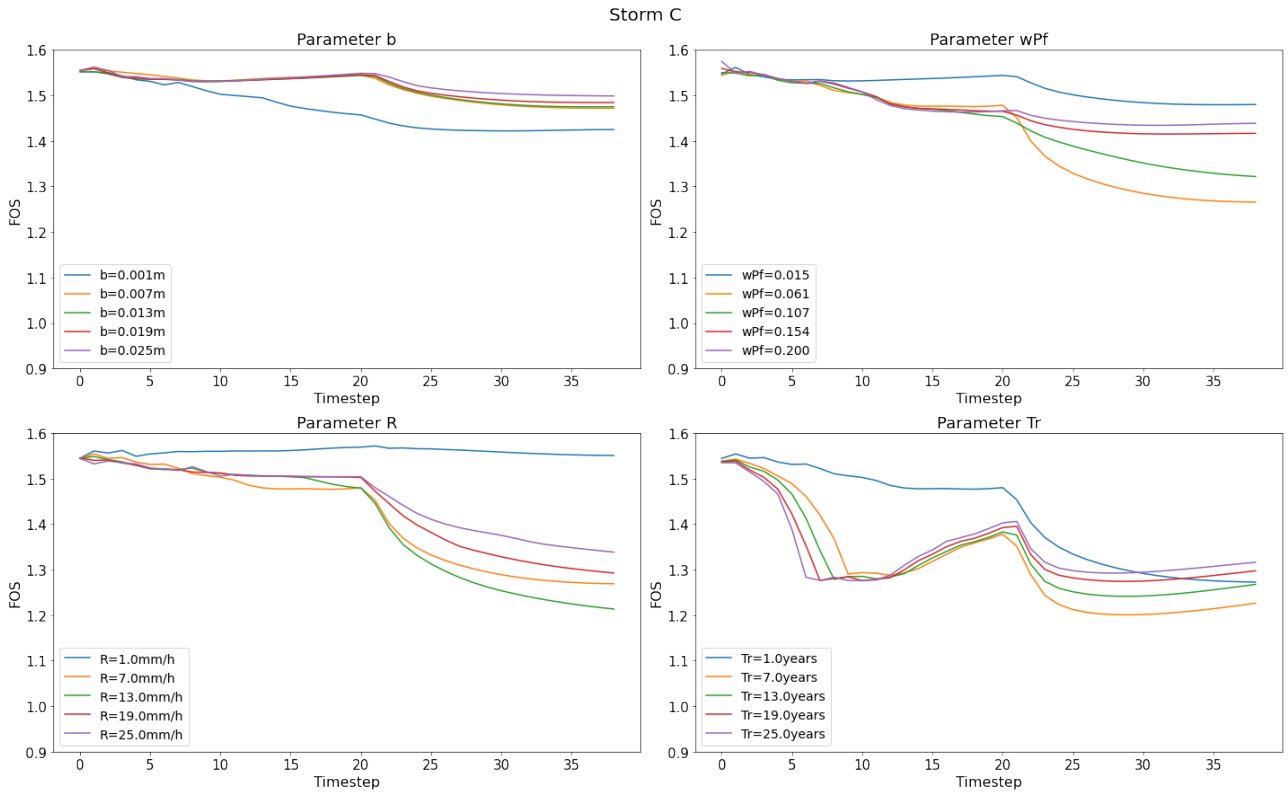

Figure 45: OAT analysis of the study parameters on the FOS timeseries of storm C.

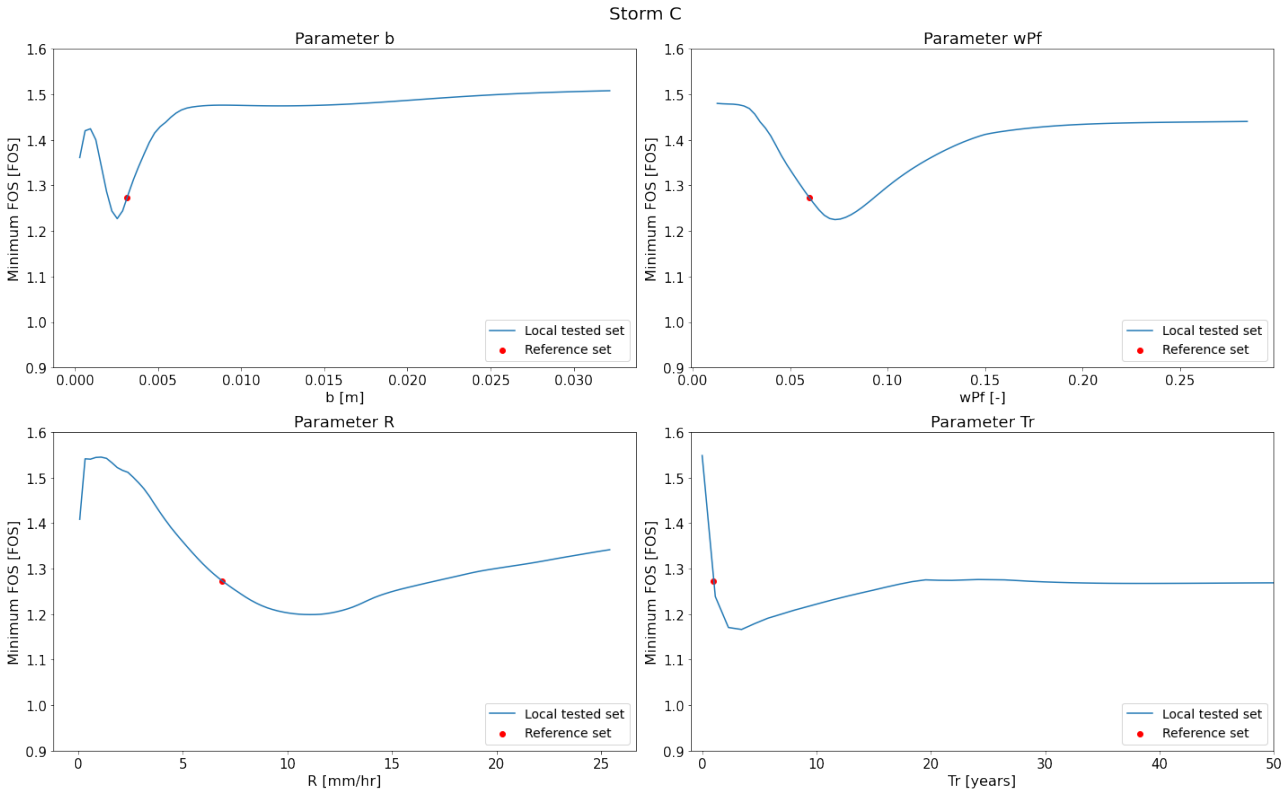

Figure 46: OAT analysis of the study parameters on the minimum FOS of storm C. The minimum FOS of the reference parameter set (b=3.15mm, wPf=6%, R=6.89mm/h, Tr=1year) was plotted in red.

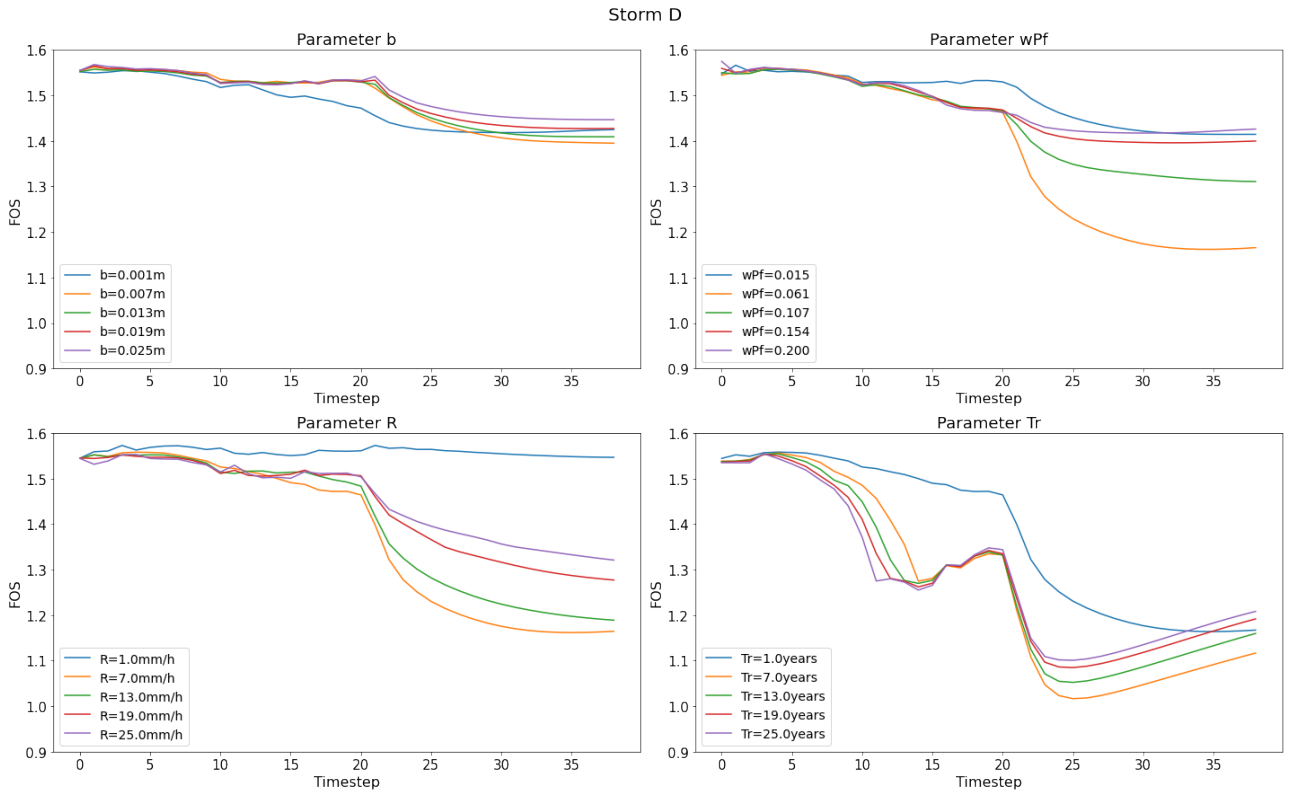

Figure 47: OAT analysis of the study parameters on the FOS timeseries of storm D.

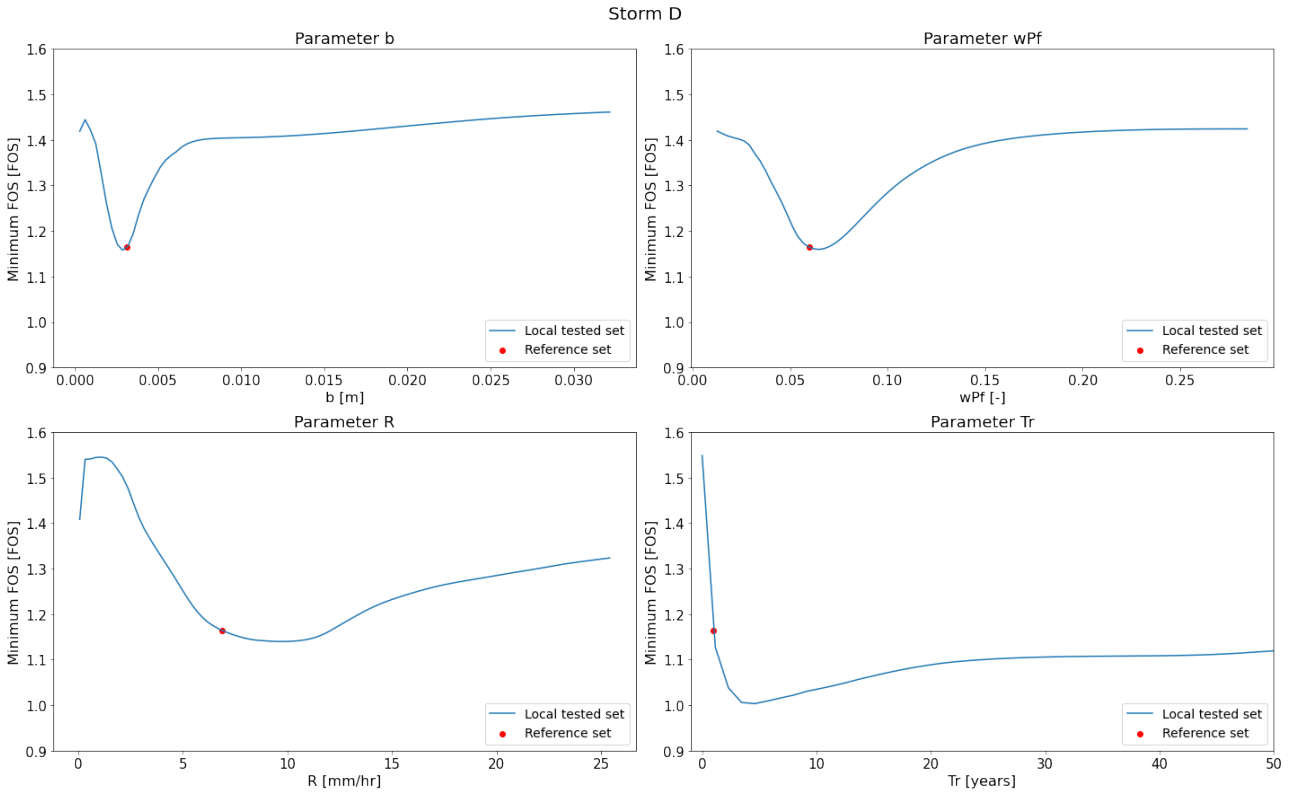

Figure 48: OAT analysis of the study parameters on the minimum FOS of storm D. The minimum FOS of the reference parameter set (b=3.15mm, wPf=6%, R=6.89mm/h, Tr=1year) was plotted in red.

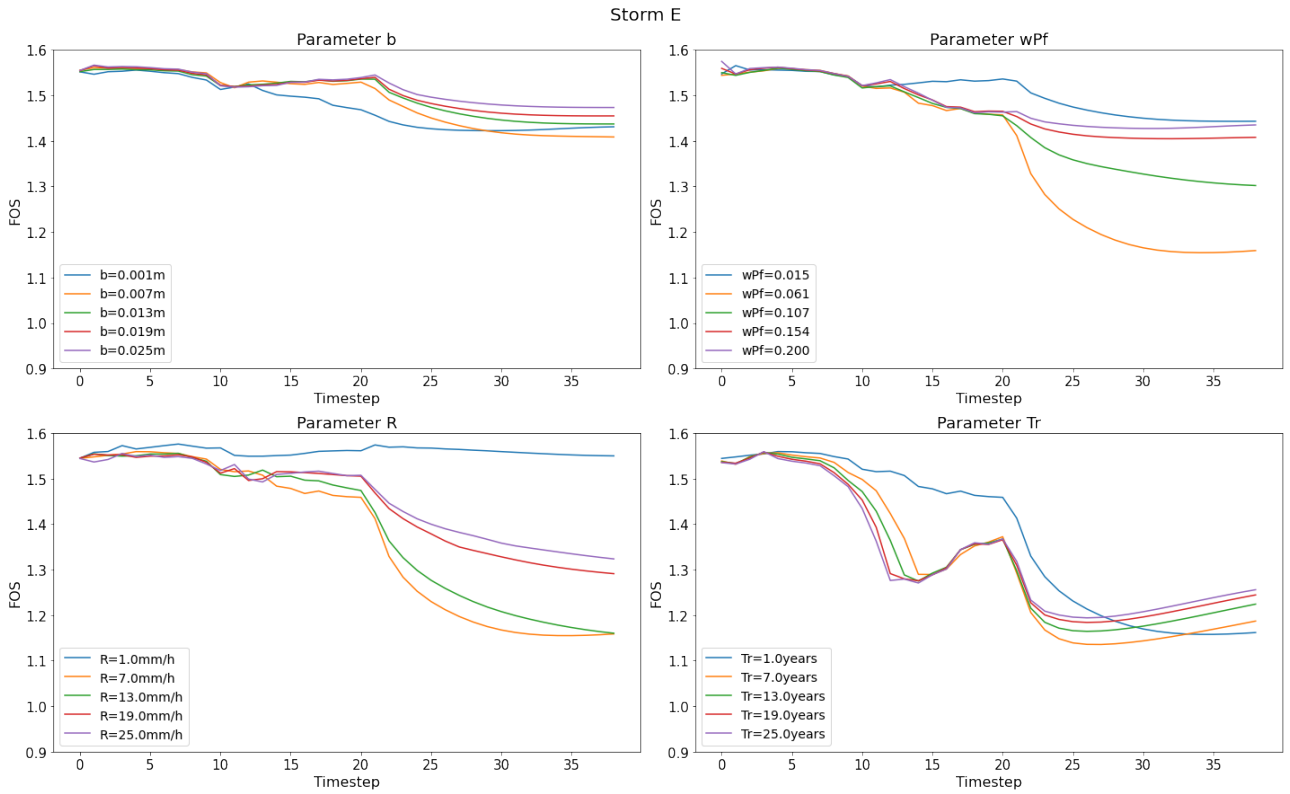

Figure 49: OAT analysis of the study parameters on the FOS timeseries of storm E.

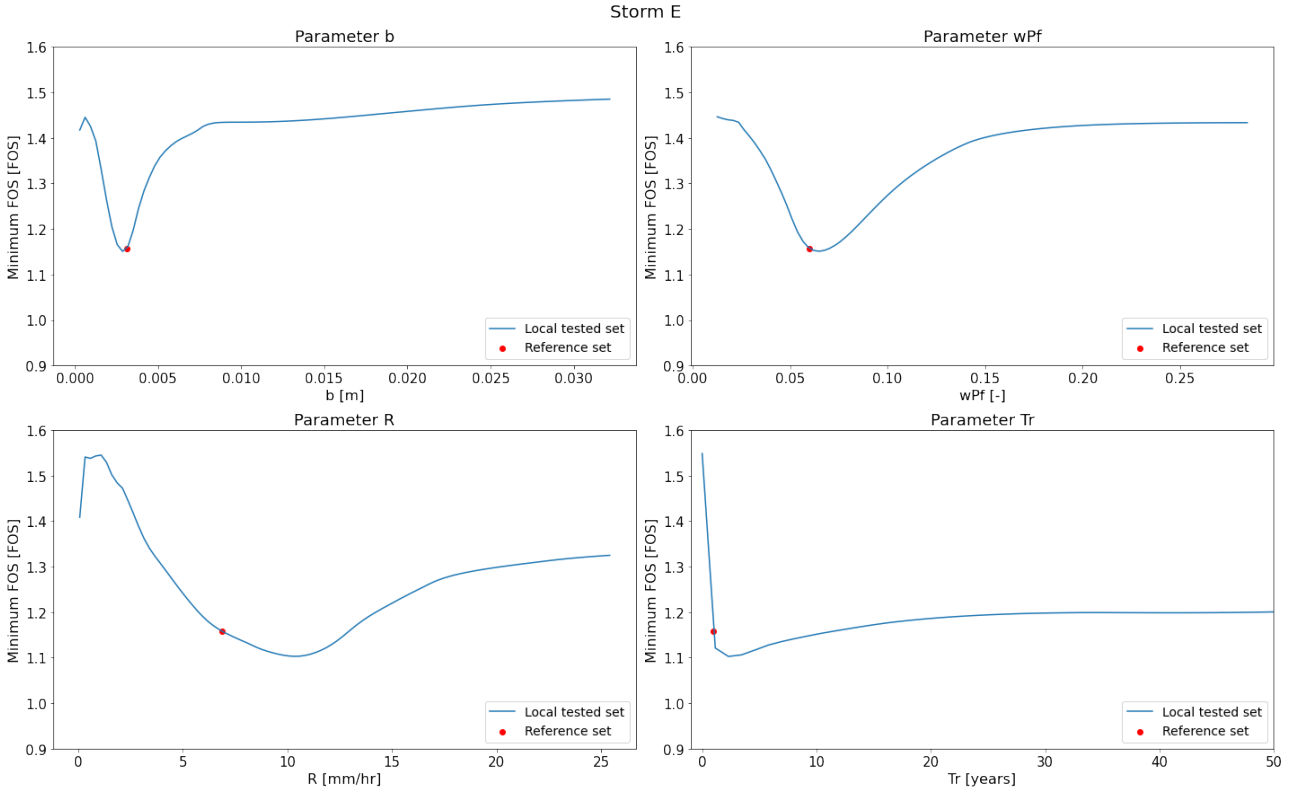

Figure 50: OAT analysis of the study parameters on the minimum FOS of storm E. The minimum FOS of the reference parameter set (b=3.15mm, wPf=6%, R=6.89mm/h, Tr=1year) was plotted in red.

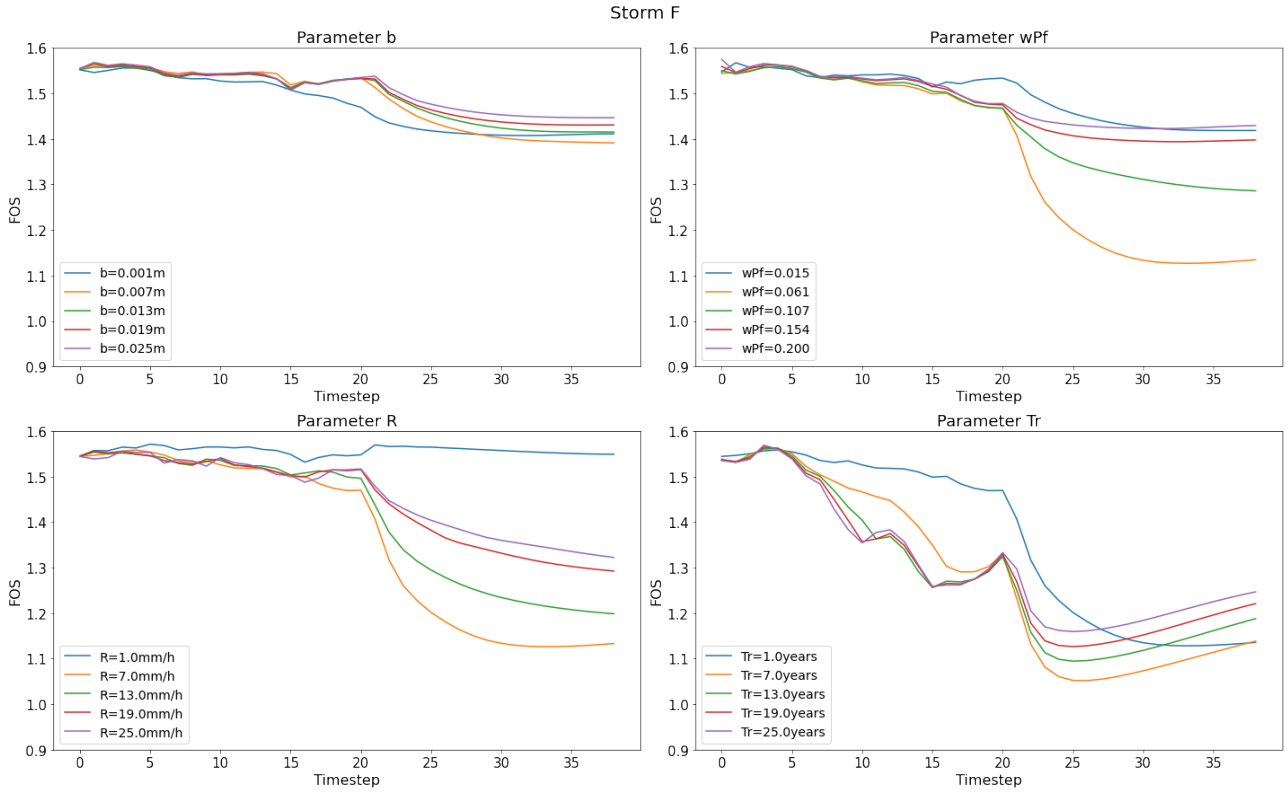

Figure 51: OAT analysis of the study parameters on the FOS timeseries of storm F.

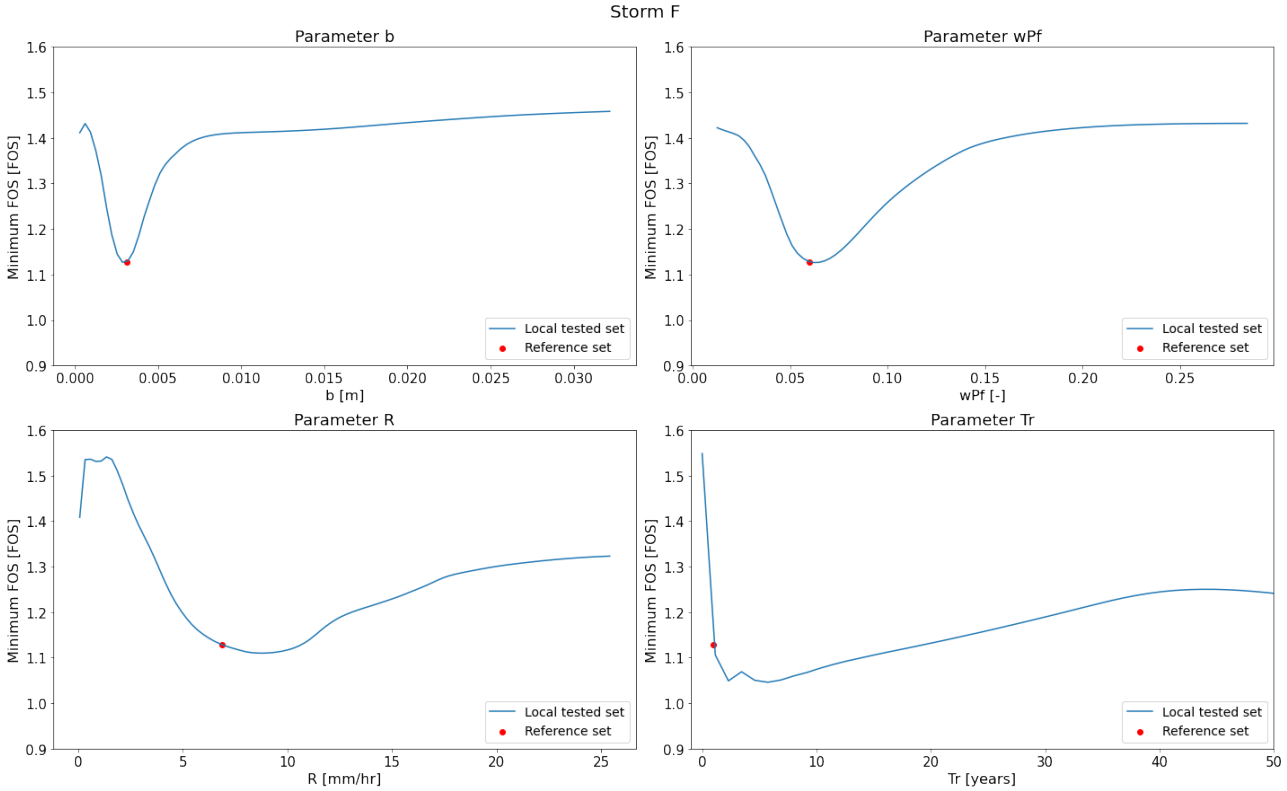

Figure 52: OAT analysis of the study parameters on the minimum FOS of storm F. The minimum FOS of the reference parameter set (b=3.15mm, wPf=6%, R=6.89mm/h, Tr=1year) was plotted in red.

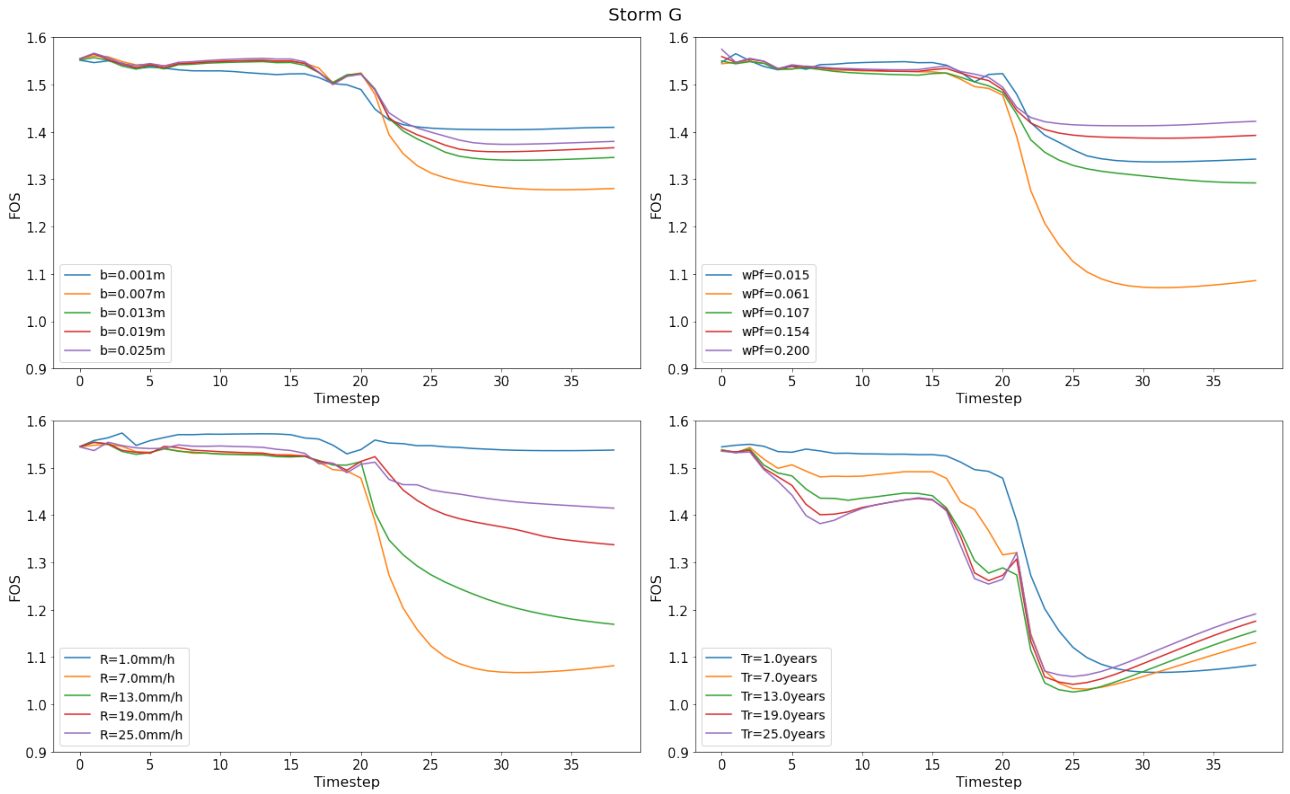

Figure 53: OAT analysis of the study parameters on the FOS timeseries of storm G.

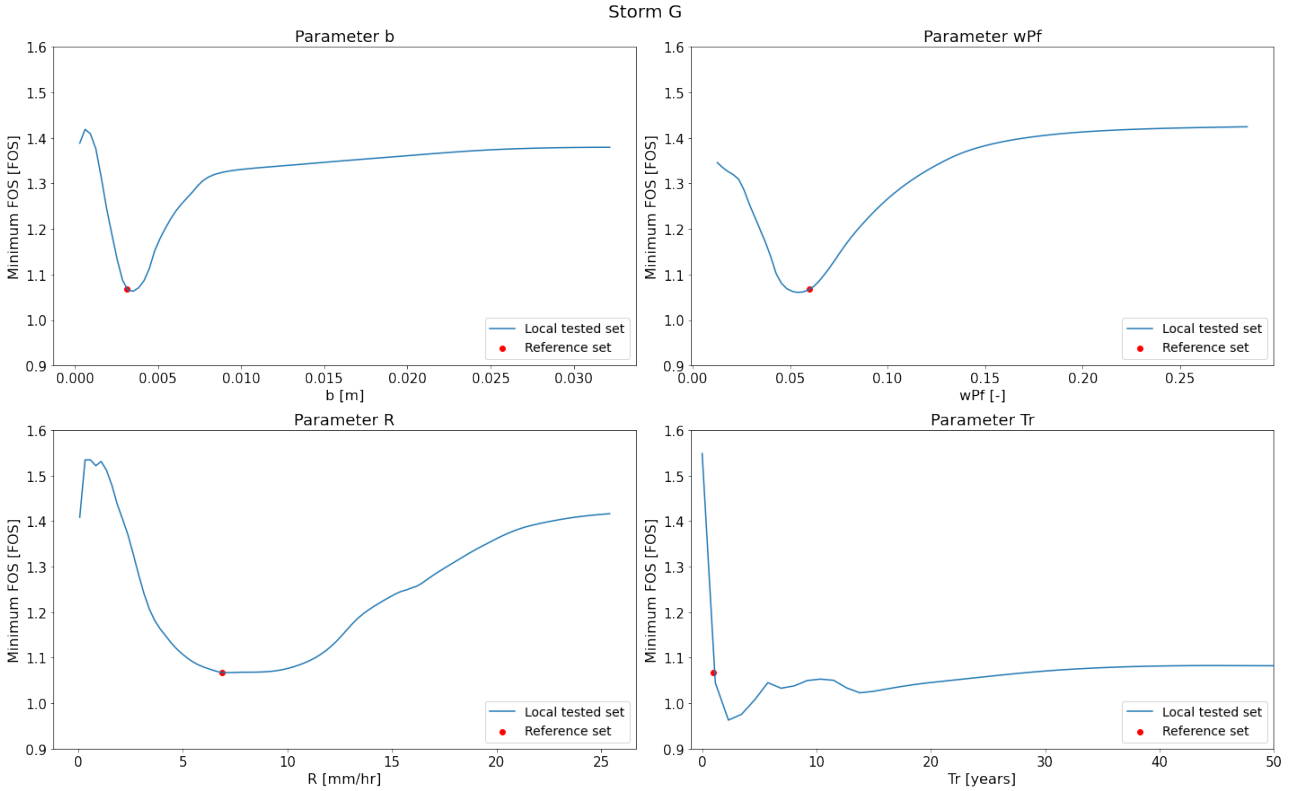

Figure 54: OAT analysis of the study parameters on the minimum FOS of storm G. The minimum FOS of the reference parameter set (b=3.15mm, wPf=6%, R=6.89mm/h, Tr=1year) was plotted in red.